The Measurement of Fuel ρR in Laser Fusion Targets Using Elastically Scattered Fuel Ions

S. T. Kacenjar

Lab Report 132
June 1982

The Measurement of Fuel ρR In Laser Fusion Targets Using Elastically Scattered Fuel Ions

by

Steve Thomas Kacenjar

Submitted in Partial Fulfillment

of the

Requirements for the Degree
Doctor of Philosophy

Supervised by Professor Leonard M. Goldman

Department of Mechanical and Aerospace Sciences
College of Engineering and Applied Science

The University of Rochester
Rochester, New York

1982

VITAE

The author was born in Cleveland, Ohio. He graduated from Parma Senior High in 1972.

In August of 1972, he joined Case Western Reserve University for undergraduate study in the Department of Physics and completed his study with honors in May, 1976.

In July, 1976 he married and in September of that same year, joined the graduate program in the Department of Mechanical and Aerospace Sciences at the University of Rochester. In 1977, he joined the Laboratory for Laser Energetics to continue his graduate research. During his graduate years, the author has been supported by a department fellowship and a Laboratory for Laser Energetics fellowship.

He has also held a parttime faculty position at Saint John Fisher College, Department of Physics, in Rochester and held the position of teaching assistant in the Department of Mechanical and Aerospace Sciences for four semesters at the University of Rochester.

ACKNOWLEDGEMENTS

The author is especially grateful for the guidance and valuable suggestions of his advisor, Professor Leonard M. Goldman. He has been an invaluable source of advice both during the research and writing stages of this dissertation.

The author is indebted to Dr. Stanley Skupsky for initially suggesting this research topic as well as for guidance in pursuing the theoretical issues of this research and to Dr. Alan Entenburg for his many useful discussions and support throughout this project, especially pertaining to nuclear diagnostics.

The author can not possibly acknowledge personally everyone who provided assistance during various stages of this research, but is grateful to all.

The author would like to give special thanks to Dr. Jacques Delettrez who performed and discussed many numerical simulation results of target compression; Professor Thomas Cormier, who helped in the calibration of the track detectors at the University of Rochester's Nuclear Structure Laboratory; Dr. Robert Fliecher and Dr. Brian Necholson, who initially acquainted me to the chemical processing of track detectors; George Korn, who was an invaluable help in various mechanical problems; and Beverly Hecht who spent long hours typing this dissertation.

Special thanks to my wife, Lori, for her patience and support during my graduate studies at the University of Rochester.

ABSTRACT

The first direct measurement of the fuel ρR in laser fusion targets has been achieved by counting the number of elastically scattered fuel ions, "knock-on particles" off 14.1 MeV DT-neutrons. Also measured for the first time was the knock-on energy spectrum which agreed well with predicted results. Both measurements required the use of thin CR-39 solid state track detectors. The presence of a proton background necessitated the development of three track criteria based on particle range and velocity to separate the knock-on deuterons and tritons from energetic protons with energies greater than 3 MeV.

Also examined here is the immediate utilization of knock-on forward-scattered deuterons to probe non-uniform fuel compressions. This requires the use of at least two track detector packages to view the target from different orientations.

A detailed discussion is also given on the future extension of the fuel ρR measurement when target ρR conditions exceed 4 mg/cm^2.

TABLE OF CONTENTS

LIST OF TABLES

List of Tables (continued)

LIST OF FIGURES

Figures (continued)

Figures (continued)

Figures (continued)

Figures (continued)

Figures (continued)

Figures (continued)

INTRODUCTION

A. Chapter Overview

During future laser fusion studies, such aspects as self-heating of the fuel by DT alpha particles and fuel ion depletion by thermonuclear burn will become of increasing importance. These aspects depend strongly upon the fuel ρR (Rho-R), a parameter which is the product of the fuel density and its confinement radius. This product is also a critical parameter for determining the proximity to thermonuclear ignition. A discussion on the significance of fuel ρR will be explored in greater detail in Chapter 2. In this chapter the author will discuss a diagnostic which has been developed and implemented to measure this parameter. The measurement relies on counting the number of elastically scattered deuterons and tritons, "knock-on particles," off the by 14.1 MeV DT neutrons. These knock-on particles are recorded on solid state track detectors.[1]

Much of the data analysis relies on a basic understanding of how solid state track detectors record charged and neutral particles. Therefore, in Appendix A a brief discussion on how track detectors work is given for those readers not familiar with this type detector.

In Chapter 3, the basic issue of how this measurement is performed is addressed. Here a discussion of various backgrounds and how they are discriminated from knock-on particles is presented.

Chapter 4 will examine more carefully the details on how the knock-on energy window is determined. Also in this chapter a discussion on optimal fuel ion concentration will be presented.

This is followed by Chapter 5 with experimental data where the method is applied and fuel ρR determined. Included here is a discussion of various measurement uncertainties entering into the estimate of ρR.

Next in Chapter 6 a discussion is given on the usefulness of this method for target ρR conditions where significant distortion in the knock-on spectrum can occur. It will be shown that the target ρR cannot exceed about .1 g/cm^2 (approximately ignition conditions) in order for the knock-on particles to have sufficient energy to escape the target.

This is followed by Chapter 8, which explores a possible application of this diagnostic to measure fuel compression nonuniformities during the time of neutron production.

The dissertation concludes with Chapter 9, which summarizes the important aspects presented in the work.

B. Fuel ρR Determination Using Knock-On Particles

This section will serve to orient the reader to the underlying physics describing how knock-on particles give information of the fuel ρR. It will then examine the experimental method developed to record and count the knock-on particles. Also a qualitative discussion will be given on the problems raised by this methodology. Lastly, this section will examine the limitations of the measurement due to particle slowdown under high target ρR conditions. No attempt is made in this section to examine quantitatively the many technical

issues associated with this method or its accompanying limitations. This discussion is reserved to later chapters in this dissertation.

Qualitatively, this method relies on the fact that the fuel ρR is directly proportional to the number of knock-ons produced. This is illustrated in Figure 1.1. In particular, the total number of knock-ons Q, is given by

$$Q = (\sigma_d \, n_d \, R + \sigma_t \, n_t \, R) \, Y_n \qquad \text{(I-1)}$$

where σ_d and σ_t are the (n,d) and (n,t) elastic cross sections, Y_n is the neutron yield and, the n_d and n_t are the deuterium and tritium ion densities. In this equation it is assumed that the neutron mean free path $(n\sigma)^{-1}$ is much larger than the fuel dimensions R. If $n_d = n_t = n_o$ and M_ρ is the mass of a proton, then the ion density can be related to the fuel density by

$$n_o = \frac{\rho}{5M_\rho} \qquad \text{(I-2)}$$

Thus, the fuel ρR can be expressed as

$$\rho R = \frac{5M_\rho}{\sigma_D + \sigma_T} \frac{Q}{Y_n} \qquad \text{(I-3)}$$

$$= 5.422 \frac{Q}{Y_n} \qquad \text{(I-4)}$$

MEASURING FUEL ρR WITH KNOCK-ONS (example)

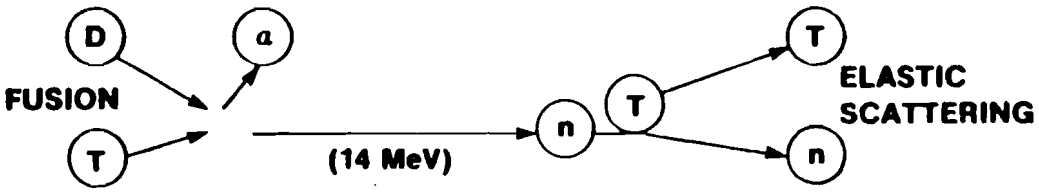

- The Number of Elastic Collisions by (n) on (T)
  $= \sigma\, n_T \langle R \rangle \approx .1\, \rho \langle R \rangle$

- Total Number of Knock-On Tritons Detected
  $Q = \sigma\, n_T \langle R \rangle \cdot Y \cdot F$

  Where

  Y = Neutron Yield

  F = Fraction of Knock-Ons in the Energy Window of The Track Detector

$$\rho \langle R \rangle \approx \frac{10Q}{Y \cdot F} \text{ g/cm}^2$$

- Determining F is The Major Theoretical Uncertainty.
  F is Sensitive to The Temperature and ρR of The Target.

TC727

Figure 1.1

where σ_D and σ_T have been taken equal to .62 and .92 barns,[2] respectively.

Unlike the fusion reaction products, the knock-on particles have a wide range of possible energies. The knock-on spectrum is shown in Figure 1.2. The maximum knock-on energies occurring at 10.6 and 12.5 MeV represent the forward-scattered tritons and deuterons. Between these peaks is a region sparsely populated and with little structure. Measurements of the particle spectrum in this region shows a distribution consistent with the knock-on spectrum.

The knock-on particles can best be counted by using thin CR-39 solid state track detectors. These detectors have nearly 100% counting efficiencies over a wide velocity interval[3] and insensitive to x-rays and electron backgrounds if doses are less than 10 Mrad.[4]

Details explaining the process by which these detectors record charged particles are given in Appendix A. Basically, they operate as follows: As a charged particle enters the detector, its electric field alters the local chemical properties of the detector by breaking chemical bonds around its trajectory. Upon chemical etching, these alterations etch more quickly than the surrounding bulk material resulting in the formation of pit structures called "tracks." For a given charge Z, measurement of the track diameter determines the particle velocity or equivalently its energy-per-nucleon (i.e., E/A where E is the particle energy divided by its nucleon number, A)[5]

Data reduction is currently complicated by the presence of a particle background and the inability of the detector to separate protons from knock-on particles over all velocities. If a stopping

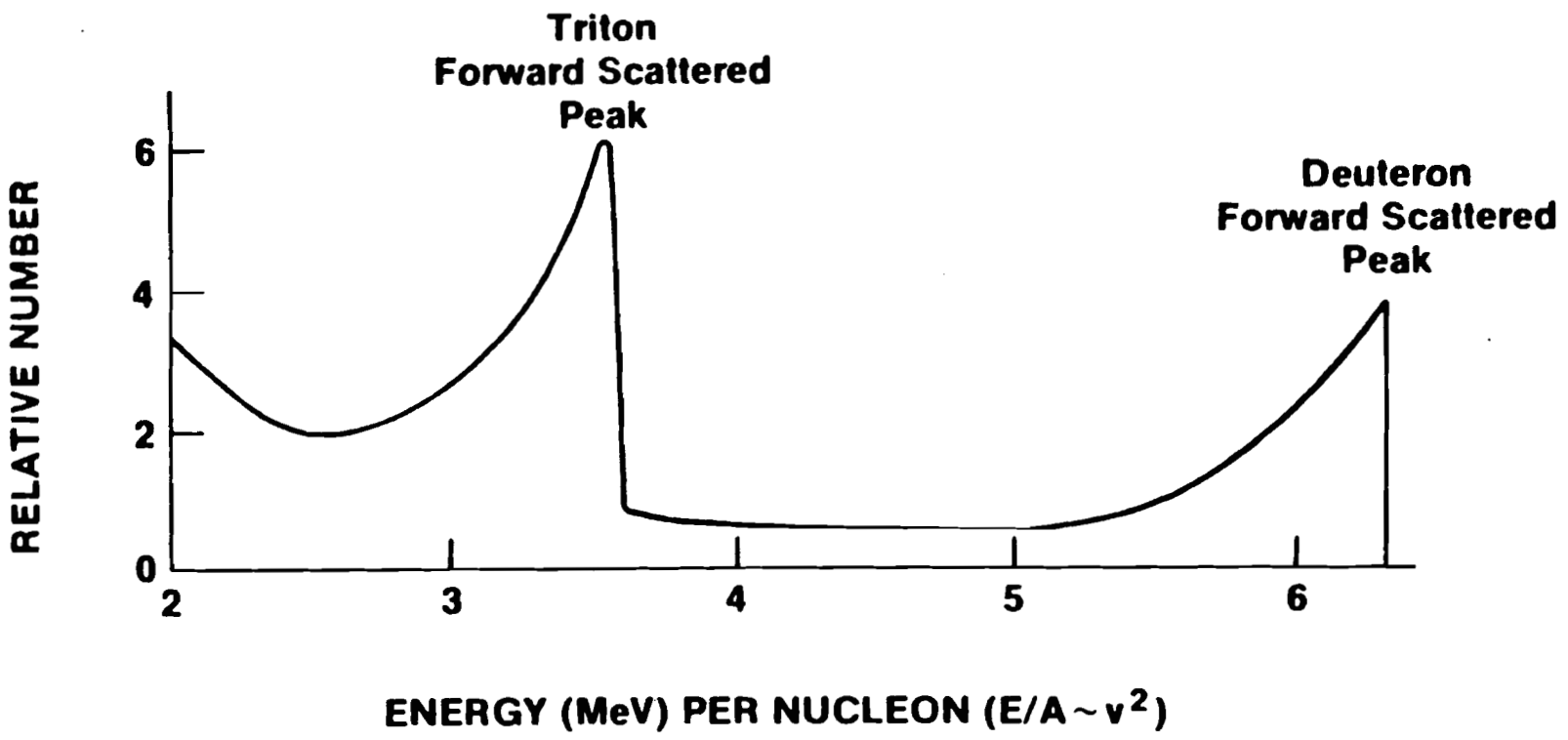

E1663

Figure 1.2

foil is not placed in front of the detector, the ion blowoff from the target will be many orders of magnitude larger than the knock-on signal thus being irretrievably lost in the myriad of overlapping background tracks. In the present experiments a 50 μm tantalum stopping foil is placed in front of the detector, as shown in Figure 1.3. This was also greater than the 40 μm of tantalum which is required to additionally stop the 3 MeV DD protons. An air gap shown in the figure is required to prevent degradation of the track detector sensitivity when placed in vacuum.

The tantalum foil does not stop energetic protons above 3 MeV or protons produced in the tantalum foil or track detector from producing tracks on the detectors. This background must be separated from the knock-on tracks by employing various track criteria. This background is most serious to deal with since knock-on tracks can have comparable track diameters with the background tracks. As track diameter gives information only of particle velocity, the particle range is additionally required to determine its nucleon number. Range information is deduced from "spatial coincident track pairs" where a track is produced on both the entrance and exit sides of the detector. The presence of such structures over a predetermined diameter interval can be used to separate protons which produce non-coincident tracks from knock-on particles which produce coincident tracks.

The finite interval of track diameters results in a limitation of the detectability over which the detector can discriminate against protons. Therefore, if Γ_d and Γ_t represent the fraction of knock-on

KNOCK-ON DIAGNOSTIC

UR
LLE

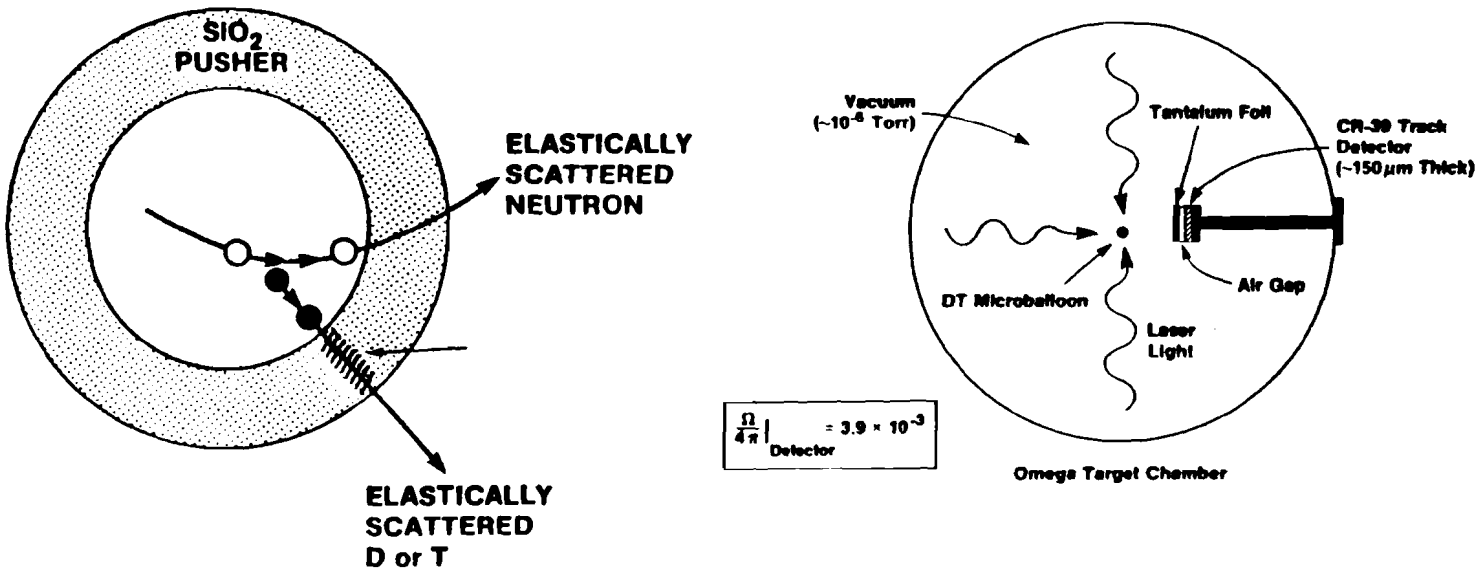

E1855

Figure 1.3

deuterons and tritons which fall into the discrimination range of the detector, then the number of spatial coincident tracks observed is given by

$$Q = (\sigma_d \Gamma_d n_d R + \sigma_t \Gamma_t n_t R) \frac{\Omega}{4\pi} Y_n \qquad \text{(I-5)}$$

where $\frac{\Omega}{4\pi}$ is the fractional solid angle subtended by the track detector.

Determination of Γ_d and Γ_t are the major theoretical uncertainties in the measurement. For target ρR conditions less than 4 mg/cm^2 these parameters can be simply determined by knowing (1) the energy interval over which the detector can separate the proton background and (2) the differential cross section for each of the two knock-on processes.[6]

In future experiments when target ρR conditions exceed 4 mg/cm^2 further uncertainties in Γ_d and Γ_t will exist. Here spectral distortion due to the slowing down of the knock-on particles through the target alters the shape of the spectrum and thus changes Γ. Two methods have been examined to correct for these distortions. One method relies on the measured energy loss of DD protons. Since these protons have velocities comparable to that of the forward-scattered tritons, they can be used to probe the localized distortion of the triton peak. This method breaks down above 10 mg/cm^2 where the protons are stopped inside the target. The second method requires the use of two detectors to view two adjacent energy intervals across the spectrum. The ratio of knock-ons from

each interval can be used to estimate the local distortion and thus correct Γ accordingly. This method can be used to about 80 mg/cm^2 where, at this point, the knock-on particles are stopped inside the target. This knock-on method therefore cannot be utilized to break-even conditions, but for the near term laser fusion program it can be cheaply and easily implemented in diagnosing compression experiments.

Unlike many other indirect methods, the targets do not have to be specially prepared in order to use the technique. The only requirement is that a DT fuel mixture be present to produce the necessary 14 MeV neutrons. Deuterium-filled microballoons are not acceptable targets for this diagnostic since the DD neutrons are not energetic enough to produce the required knock-on energies to separate them from the DD protons.

C. Alternative Methods In Measuring Fuel ρR

Various methods have been proposed to measure fuel ρR. These include (1) neutron activation of the tamper material by the DT neutrons,[7] (2) Stark broadening of seed material initially mixed in the fuel,[8] (3) DT-to-DD reaction ratio for deuterium-filled targets,[9] and (4) intensity measurements of the Kα x-ray radiation produced by the scattering of charged particle fusion products off high Z seed material in the fuel.[10] Each method has its distinct inherent difficulties, as will be discussed below.

1. Neutron Activation

Figure 1.4 shows the basis physics of this diagnostic. Here a 14 MeV neutron interacts with a ^{28}Si nuclide producing a proton and excited ^{28} Aℓ* nuclear state. This state decays first by β^- emission (whose endpoint energy is 2.86 MeV) to ^{28}Si* having a half-life of 2.24 minutes, which then γ-decays. To reduce background counts both β^- and γ rays are counted in coincidence. (The intermediate state has a half-life of only 0.5 ps.)

The number of activated nuclei N* is given by

$$N^* = \sigma Y_n n_{Si} \Delta R \qquad \text{(I-6)}$$

$$\text{where} \qquad n_{Si} = \rho \frac{A_n}{M} \qquad \text{(I-7)}$$

The parameter n_{Si}, ΔR, A_n, ρ, and M are the silicon number density, pusher-tamper thickness, Avogadro's number, glass density and the atomic mass, respectively. Therefore, the number of activated nuclei can be directly related to the tamper ρR by

$$N^* = \frac{0.6\ \sigma\ (\text{barns})}{A}\ Y_n\ (\rho \Delta R) \qquad \text{(I-8)}$$

The (n,P) cross section for ^{28}Si is 0.25 barns. It is therefore less efficient per DT neutron than with the knock-on method

Neutron Activation

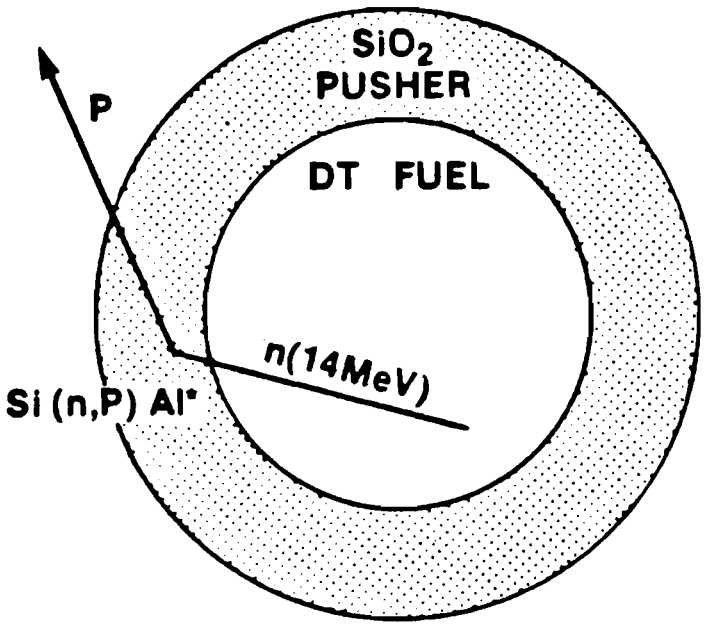

'RAD CHEM'

Figure 1.4

which uses the cross sections of 0.62 and 0.92 barns for the deuteron and triton, respectively.

It should be noted that N* is not the detected count but rather the total number of activated nuclei. Typically, a five-minute sampling time is taken to obtain adequate counting statistics. This, in turn, increases the threshold value still further.

Another limitation of this technique is that it does not measure the fuel ρR directly but must rely on numerical simulation to infer this from the tamper conditions. Only in extreme cases of spherical symmetry, uniform density in both the fuel and pusher-tamper, and thin shell can the initial parameters and measured compressed tamper ρR give exact results for the compressed fuel ρR; namely,

$$(\rho R)_{f_c} = (\rho R)_{f_o} \frac{(\rho \Delta R)_{P_c}}{(\rho \Delta R)_{P_o}} \qquad \text{(I-9)}$$

where $(\rho R)_{f_o}$, $(\rho R)_{f_c}$, $(\rho \Delta R)_{P_o}$, and $(\rho \Delta R)_{P_c}$ are respectively the initial and compressed ρR of the fuel and pusher-tamper. These assumptions are not met in laser fusion targets and therefore density modeling is necessary to extract fuel ρR conditions.

2. Stark Broadening

The width of spectral lines under certain conditions give direct information of the local density where they are produced. This in turn can be used to estimate the fuel ρR. Four basic

mechanisms can produce spectral broadening. These are listed below:

(1) Natural
(2) Doppler
(3) Collisional (Stark)
(4) Zeeman

The first broadening mechanism is inversely proportional to the lifetime of the state (result of Heisenberg uncertainty principle). No density information is obtained by this process. The second mechanism, Doppler broadening, increases the line-width due to the random thermal motion of the emitting atoms. Again no density information is obtained by this mechanism. However, for Stark broadening the local electric field of neighboring atoms can alter the states enough so that the energy levels are smeared. The degree of smearing (which is Lorentzian in shape) gives direct information of the local density. That last process of Zeeman splitting is relevant only when magnetic fields are present. This process has as yet not been identified from laser fusion targets.

Therefore, useful density information can be extracted from only Stark broadening. This has been done by placing Ne inside the target. However, the task of unfolding this broadening component from Doppler broadening is a non-trivial task. In addition, this method breaks down at fuel densities on the order of 1 to 2 mg/cm^3 where the spectral lines begin to overlap. The possibility of using argon in place of neon has been suggested, but higher temperatures are required.

Still another difficulty arising from this method is that the atoms may radiate at times significantly different from the time when the thermonuclear burn occurs. Thus measured fuel ρR values may not characterize the fuel conditions during the time of neutron production.

3. Measurement of DT-to-DD Reaction Ratio

The ratio of DT neutrons to DD neutrons gives direct measurement of the fuel ρR for tritium-free targets. In one of two possible DD reaction channels a 1 MeV triton is produced. As the triton travels through the fuel the probability of causing a DT reaction is proportional to the deuteron number density (and therefore the fuel density) and the distance traveled through the fuel. There, however, exist three limitations of this method. These are:

(1) the analysis can only be used for tritium-free targets,

(2) the detection efficiency is limited by the neutron detection efficiency and

(3) large uncertainties in the ratio result for fuel ρR conditions greater than $10^{-2} g/cm^2$ when ion fuel temperatures are less than 5 KeV.

Direct detection of the DD protons and the DT alpha particles result in high detection efficiency. Unfortunately, for target ρR conditions greater than $10^{-3} g/cm^2$ the alpha particles are stopped within the target and above $10^{-2} g/cm^2$ the DD protons are also stopped

in the target. Therefore, the detection of neutron reaction products will be necessary for target conditions in excess of .001 g/cm^2.

Limitation (3) is the result of the fact that the beam average reaction rate $\langle\sigma v\rangle_b$ is a very sensitive function of ion temperature below 5 KeV, as shown in Figure 1.5 (taken from reference 9).

The fuel ρR can be measured in a very similar manner by the ratio of DD neutrons to D^3H_e protons from deuterated targets. The chief limitation here is that the D^3H_e has a much smaller beam reaction rate compared to the DT beam reaction rate.

4. Intensity Measurement of Kα X-Ray Lines

Fusion products, in particular DT alpha particles and DD protons, can be used to produce K-shell x-rays from seeded materials initially mixed in the fuel. The number of such x-rays is proportional to the fuel ρR. Figure 1.6 shows that the cross section falls rapidly with increasing Z of the seed material. However, low Z seed material cannot be arbitrarily used because of the presence of a large x-ray background resulting primarily from bremsstrahlung from the target shell. Typical data of the x-ray background from the Zeta Laser System show that a reasonable seed material should have a Kα energy of greater than 8 KeV. This requires a Z of 30 or higher. Such high Z materials can have detrimental effects on the target performance. If the concentration is too high, excessive radiation cooling of the fuel can degrade the thermonuclear performance and overestimate realistic target compressions for strictly DT-filled targets. The opposite extreme of low seed concentration may result in insufficient

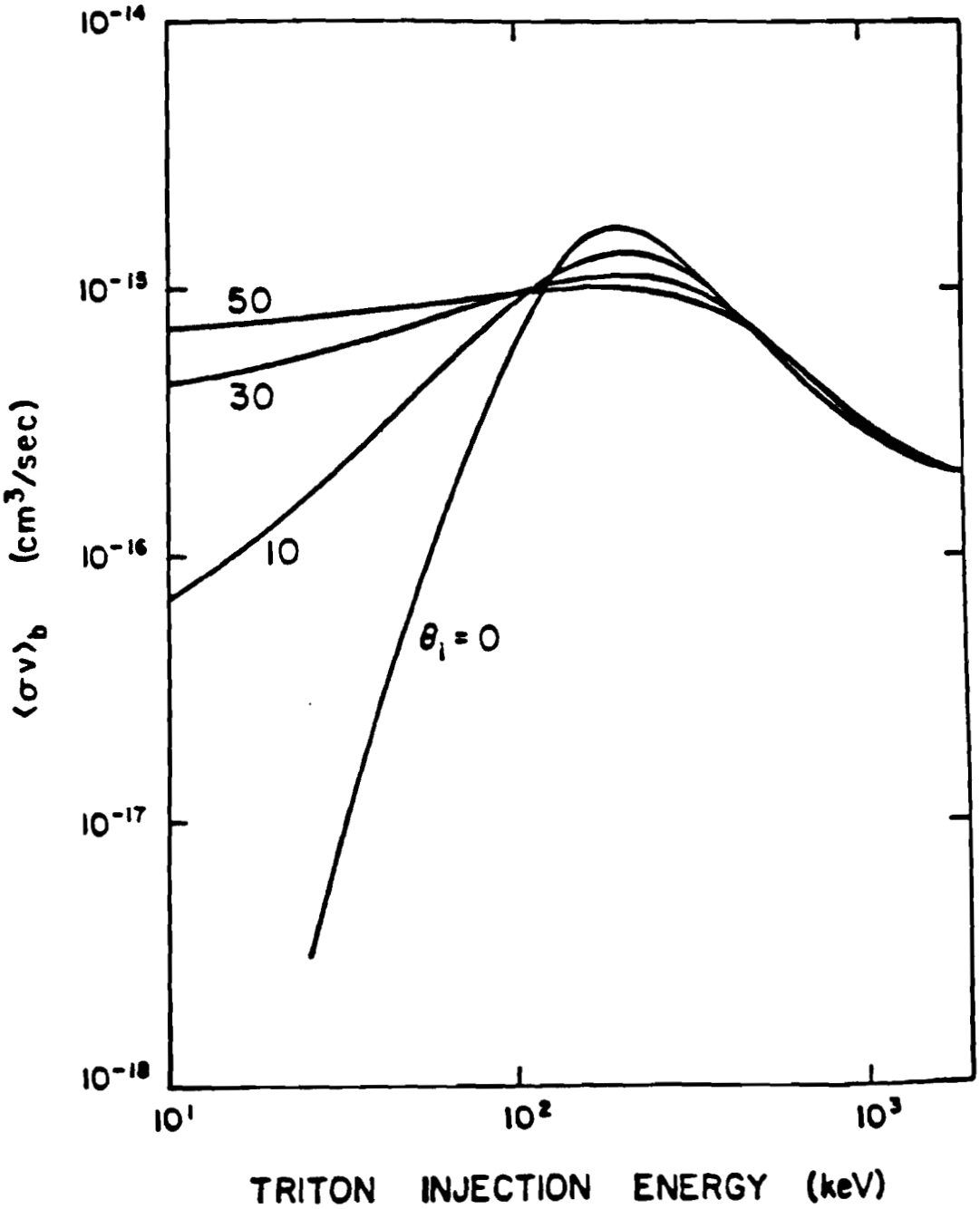
10^{-14}
10^{-15}
10^{-16}
10^{-17}
10^{-18}
50
30
10
$\theta_i = 0$
$\langle\sigma v\rangle_b$ (cm^3/sec)
10^1
10^2
10^3
TRITON INJECTION ENERGY (keV)

Figure 1.5

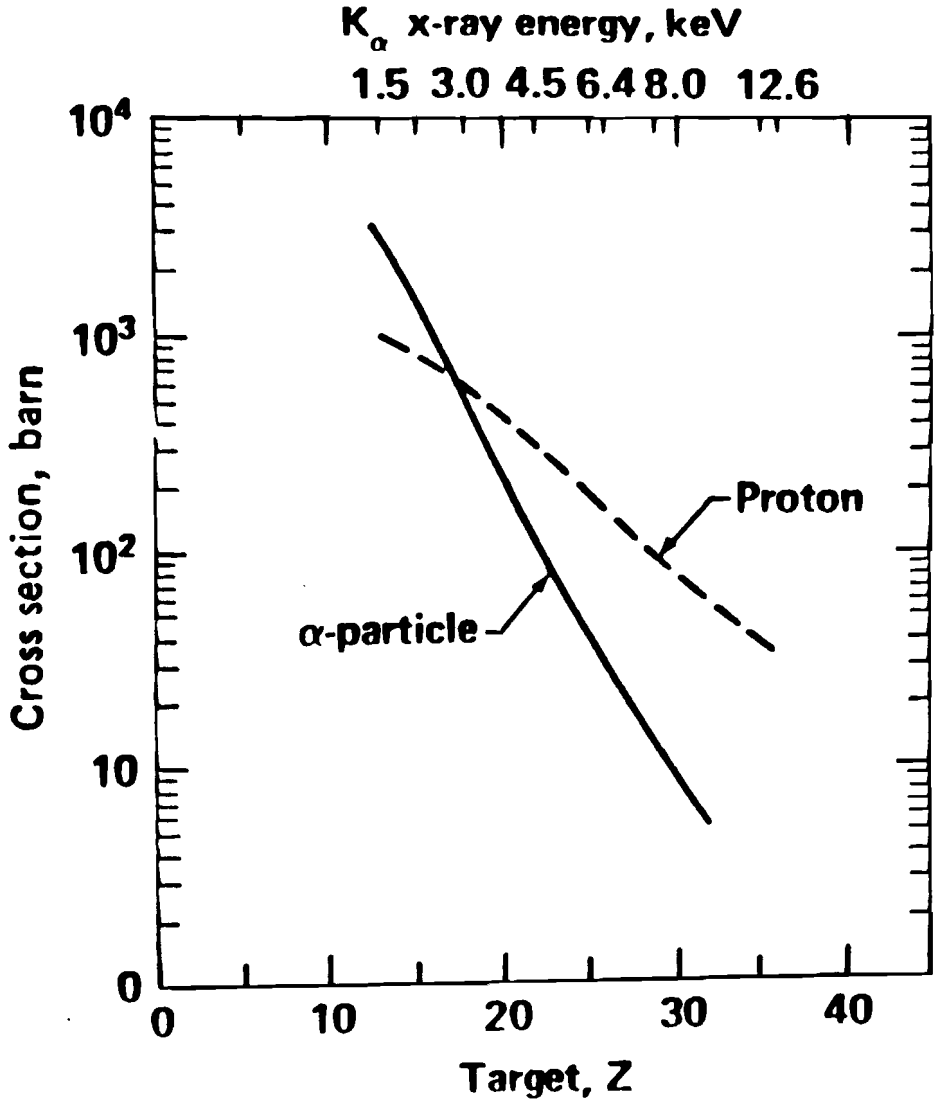
K_α x-ray energy, keV
1.5 3.0 4.5 6.4 8.0 12.6
10^4
10^3
10^2
10
0
Cross section, barn
Proton
α-particle
0
10
20
30
40
Target, Z

Figure 1.6

Kα intensity to be easily separated from the x-ray background. In either case, specially prepared targets will be required to diagnose the fuel ρR conditions.

A second method which uses Kα emission to measure compression is by measuring the dimension of the emission region using an x-ray pinhole camera. It is easily shown assuming uniform density and conservation of mass that

$$(\rho R)_f = (\rho R)_o \left(\frac{R_o}{R_f}\right)^2 \qquad \text{(I-10)}$$

where $(\rho R)_f$, $(\rho R)_o$ and $\left(\frac{R_o}{R_f}\right)$ are the final and initial fuel ρR and the initial-to-final fuel radii, respectively. Notice that measurement uncertainty in R_c will result in a two times larger uncertainty in the fuel ρR estimate. For example, if the compressed fuel has a dimension of 20 μm and the spatial resolution is 5 μm, the fuel ρR uncertainty is ±50%.

This procedure suffers from the same limitation as mentioned above when the Kα intensity lines are measured.

D. Conclusions

Because the methods described above have a number of inherent difficulties, such as tamper density modeling, utilization of specially prepared targets, and high threshold and resolution limitations, the knock-on diagnostic has been developed at the University of Rochester's Laboratory for Laser Energetics. This diagnostic has

the lowest detection threshold compared with all other alternative methods and does not rely on modeling of tamper conditions. In addition, standard DT-filled targets can be used with this method.

II THE SIGNIFICANCE OF FUEL ρR

A. Chapter Overview

Estimates for establishing breakeven requirements, fractional DT burn, and self-heating of the fuel will be shown to be strongly dependent on the fuel ρR conditions. Emphasis will be placed on the derivation of analytical models to clarify the relevant physical principles. These models have a number of simplifications which can only be treated properly with the use of complex numerical codes involving transport phenomena, ablation, hydrodynamic and nuclear burn. The goal of this chapter is to discuss the qualitative importance in which ρR enters into these estimates and in doing so stimulates additional discussion by an increased number of researchers in this field.

The chapter will be divided into three sections. In section B, a model will be presented for the fuel conditions required to achieve breakeven conditions. Here it will be shown that the required fuel ρR depends primarily on the fuel temperature and has a minimum at about 20 KeV. As will be discussed, this minimum is the result of two competing processes: the reaction rate and radiation loss due to Bremsstrahlung.

Section C will examine the dependence of fractional burn on ρR. Included here is an estimate of the disassembly time of the target based on the time required for a rarefaction wave to travel from the target surface to its center. This estimate is then used to

calculate the fractional burn. As will be shown, this dependence is a strong function of fuel temperature for $T \lesssim 20$ KeV but is almost insensitive to temperatures between 20 KeV $\lesssim T \lesssim$ 70 KeV.

This chapter will close with a discussion of self-heating of the fuel by the redeposition of energy by the DT alpha particles. Here again, the fractional energy deposition will be shown to be a function of the fuel ρR.

B. Breakeven Requirements

In laser fusion research, the fuel ρR is of fundamental importance, analagous to the parameter $n \tau_c$ found when describing magnetically confined systems. What follows is a simple model which addresses the various considerations which explain the dependence of breakdown requirements on ρR. Exact quantitative requirements are not derived in this section, for these require complex numerical modeling of the hydrodynamic, laser-plasma interaction, and the thermonuclear burn.

Consider a laser fusion pulse reactor which delivers energy to a DT plasma so that it rapidly heats the plasma to a temperature T. It is assumed here that $T = T_e \equiv T_i$ (this assumption will break down if the plasma is predominantly shock-heated and if the thermalization time is long compared with the pellet confinement time). A feasible working reactor must satisfy the condition that the output energy be greater than the input energy requirements for the reactor. Assuming that the particle number densities in the fuel is $n \equiv 2n_d = 2n_t$ and

that the fusion system has a confinement time τ_c, then the following energy sources can be identified:

$3nkT$ = total thermal energy of plasma per M^3

$\tau_c P_n = \frac{1}{4} n^2 \langle\sigma v\rangle Q_t \tau_c$ = total thermonuclear energy generated by DT reactions per M^3

As a conservative approximation assume that the plasma is optically thin to Bremsstrahlung radiation generated by the plasma. The energy balance analysis can then be simplified. The total Bremsstrahlung power generated per unit volume P_β is equal to

$$P_\beta = 1.8 \times 10^{-38} n^2 (kT)^{1/2} \quad [J/M^3] \tag{2-1}$$

where kT is in units of eV. The total available energy E_α, during the confinement time is

$$E_a = 3nkT + \tau_c P_\beta + (1-\eta) \tau_c P_n \tag{2-2}$$

where η denotes the fraction of nuclear reaction energy retained as thermal energy in the plasma. As will be shown in section D, η is a strong function of fuel ρR and electron temperature. The minimum injection energy E_i, required to heat the plasma and to provide for Bremsstrahlung energy loss is

$$E_i = 3nkT + \tau_c P_\beta - \eta \tau_c P_n \tag{2-3}$$

Assuming an efficiency ε (i.e., typically assumed to be equal to 1/3) in the conversion of the available energy into useful energy to power for example, the next pulse then

$$\varepsilon[3nKT+\tau_c P_\beta+(1-n)\tau_c Pn] > 3nkt+\tau_c P_\beta - n\tau_c P_n \qquad (2\text{-}4)$$

Defining $\hat{P}_\beta = P_\beta/n^2$ and $\hat{P}_n = P_n/n^2$ and solving for $n\tau c$ one obtains

$$n\,\tau_c > \frac{3kT}{\hat{P}_\beta} \quad \frac{1}{\frac{\hat{P}_n}{\hat{P}_\beta}\,\Gamma - 1} \qquad (2\text{-}5)$$

where

$$\Gamma \equiv \frac{\varepsilon + \eta\,(1-\varepsilon)}{1-\varepsilon} \qquad (2\text{-}6)$$

The confinement time as shown in section C of the chapter is shown to be equal to

$$\tau_c = R/4\,C_s \qquad (2\text{-}7)$$

where R is the compressed radius of the fusion target and C_s is the sound speed, which is given by

$$C_s = [(\gamma_i P_i + \gamma_e P_e)\rho]^{1/2} \qquad (2\text{-}8)$$

$$= \left(\frac{10}{3}\,\frac{T}{\langle M\rangle}\right)^{1/2} \text{ for } \gamma_i = \gamma_e = 5/3 \qquad (2\text{-}9)$$

Therefore equation (5) can be expressed in terms of fuel ρR and takes the final form

$$\rho R > 12\left(\frac{10}{3}\right)^{1/2} \left(\langle M_i \rangle\right)^{1/2} (kT)^{3/2} \frac{1}{\bar{p}_\beta} \frac{1}{\frac{\bar{p}_n}{\bar{p}_\beta} r - 1} \qquad (2\text{-}10)$$

Equation (10) expresses the fact that the required fuel ρR to achieve breakeven is dictated by the plasma temperatures, system efficiency, and the degree of alpha particle self-heating.

Figure 2.1 shows the functional dependence of the Maxwellian average reaction rate $\langle \sigma v \rangle$, as a function of ion temperature. As shown, the optimal to operate the reactor because of the higher losses due to Bremsstrahlung. For temperatures less than 10 KeV the thermonuclear reaction rate drops rapidly with decreasing temperature. Therefore, the optimal fuel temperature as shown in Figure 2.2 is about 20 KeV. If self-heating is not significant, the breakeven condition requires a fuel ρR of about .2 g/cm^2 at a temperature of 15 KeV. The role of self-heating and its dependence on ρR will be discussed in greater detail in section D of this chapter.

C. Fractional Burn

After the DT fuel is compressed and heated it commences to burn. The duration of the burn is determined by the confinement time, which is the time required for a rarefaction wave to travel a distance R from

Fusion Reaction Rates as a Function of Temperature

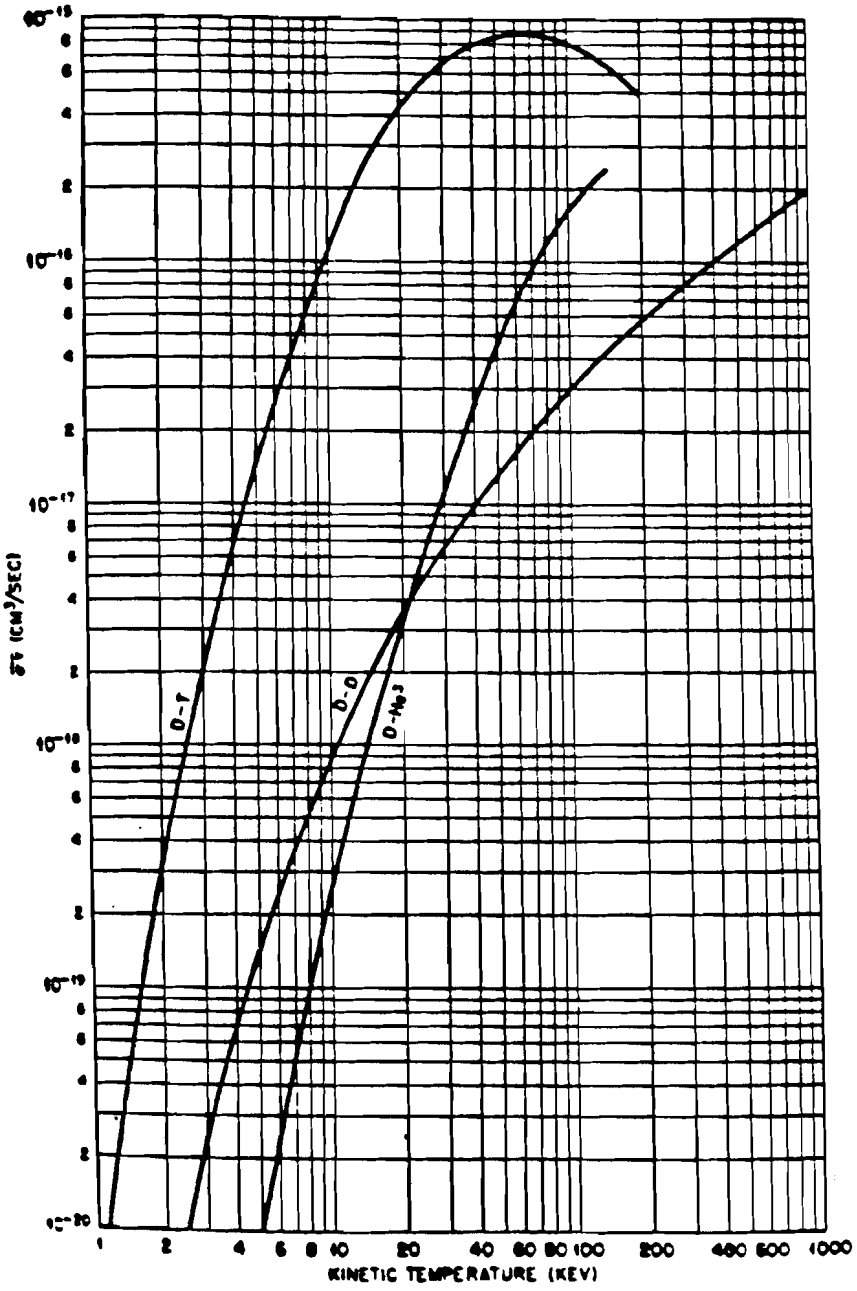

Figure 2.1

BREAKEVEN REQUIREMENTS WITH AND WITHOUT SELF-HEATING

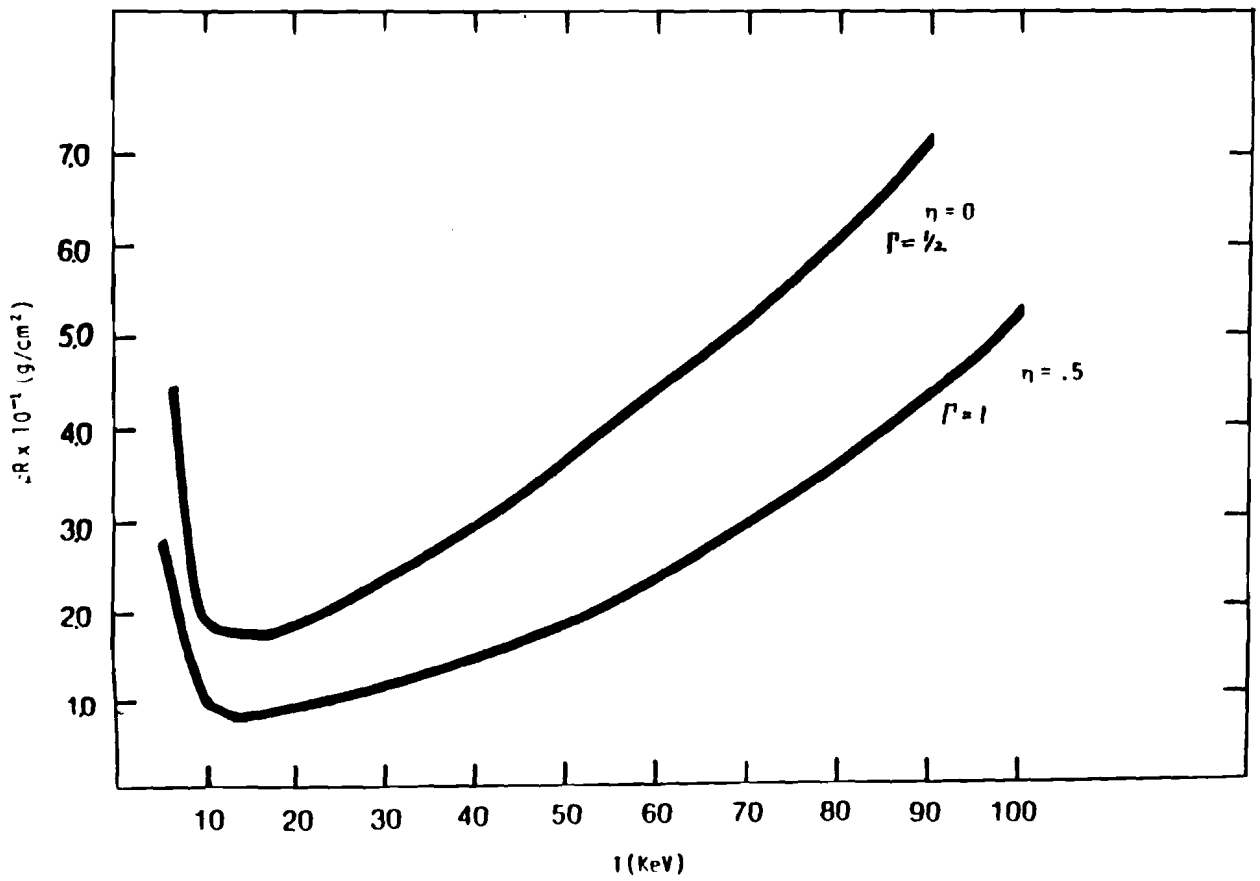

Figure 2.2

the surface of the pellet to its center. During this time a fraction of the fuel undergoes fusion. As will be shown, the fractional burn is a function of fuel ρR and temperature. In addition, it will be shown that for fuel temperatures over the range $T_e = T_i \equiv T = 20$ to 70 KeV the fractional burn has a weak temperature dependence and thus it is predominantly a function of fuel ρR.

The fractional burn (f_r) is defined as

$$f_r = \frac{n_\alpha + n_n}{n_\alpha + n_n + n_o + n_t} \equiv \frac{n_p}{n} \tag{2-11}$$

where n_α and n_n are the number densities of DT alpha particles and neutrons. Combining this with the fusion reaction rate equation it can be shown that (See Appendix B)

$$\dot{f}_r = \left(\frac{1}{2\tau_r}\right)(1 - f_r)^2 \tag{2-12}$$

where

$$\tau_r \equiv [n\langle\sigma v\rangle]^{-1} \text{ (reaction time)} \tag{2-13}$$

In deriving equation (12) it was assumed that the deuterium-tritium fuel mixture was 50/50. Small departures from this situation will not affect the fractional burn significantly because of the weak dependence of the reaction rate on the fuel ion density ratio.

Implicit in equation (12) is that the fuel is assumed to be in thermodynamic equilibrium. This is not generally valid since a large

temperature gradient is generated by the coalescing of shocks at the center of the target. Therefore, $\langle\sigma v\rangle$ is not uniquely defined across the fuel. Under current target conditions a central region of the fuel can be heated to temperatures in excess of 8 KeV while surrounding fuel is heated to about 1 KeV. As emphasis changes from short pulse - high intensity laser conditions to long pulse - low intensity laser conditions these temperature gradients may be somewhat reduced.

Keeping these limitations in mind, equation (12) can be solved for f_r giving

$$f_r = \frac{t/2\tau_r}{1 + t/2\tau_r} = \begin{cases} t/2\tau_r & t \ll \tau_r \quad (2\text{-}14a) \\ 1 - 2\tau_r/t & t \gg \tau_r \quad (2\text{-}14b) \end{cases}$$

This assumes that the reaction time is constant during the burn. Notice that if the confinement time is large compared with the reaction time, the fuel becomes depleted and f_r approaches 1. In practice, however, the other extreme is presently encountered. Setting t equal to the confinement time R/C_s where C_s is given by equation (9), equation (14) can be expressed in terms of ρR.

As the fuel burns, less and less of the fuel can participate because of disassembly. The average mass used during the confinement time is

$$M = \frac{\int_0^{t = R/C_s} \frac{4}{3}\pi\rho\ (R - C_s t)^3 dt}{R/C_s} \qquad (2\text{-}15a)$$

$$= \frac{M_o}{4} \qquad (2\text{-}15b)$$

where M_o is the total mass of the pellet. This, in turn, is reflected in the burn efficiency which is reduced by a factor of 4. Therefore setting $t = R/4C$ equation 2-14 becomes

$$f_h = \frac{\rho R}{\phi(T) + \rho R} \qquad (2\text{-}16)$$

where

$$\phi(T) = 8\, M_i \frac{C_\delta}{\langle \sigma v \rangle} \qquad (2\text{-}17)$$

and where M_i is the average fuel ion mass. Since both C_δ and $\langle \sigma v \rangle$ are still strictly functions of temperature so too is $\phi(T)$.

In present experiments, the confinement time is very much smaller than the reaction time. This leads to an expression for f_h (using equations 14b and 17) given by

$$f_h = \phi^{-1}(T)\ \rho R \qquad (2\text{-}19)$$

The function $\phi(T)$, as plotted in Figure 2.3, has a broad minimum for temperatures between 20 and 70 KeV with an average value of $11 g/cm^2$. Therefore, the fractional burn in this region is almost totally a function of fuel ρR. These high temperatures will most likely not be generated by direct conversion of laser energy into thermal energy but rather due to self-heating of the fuel by the DT alpha particles.

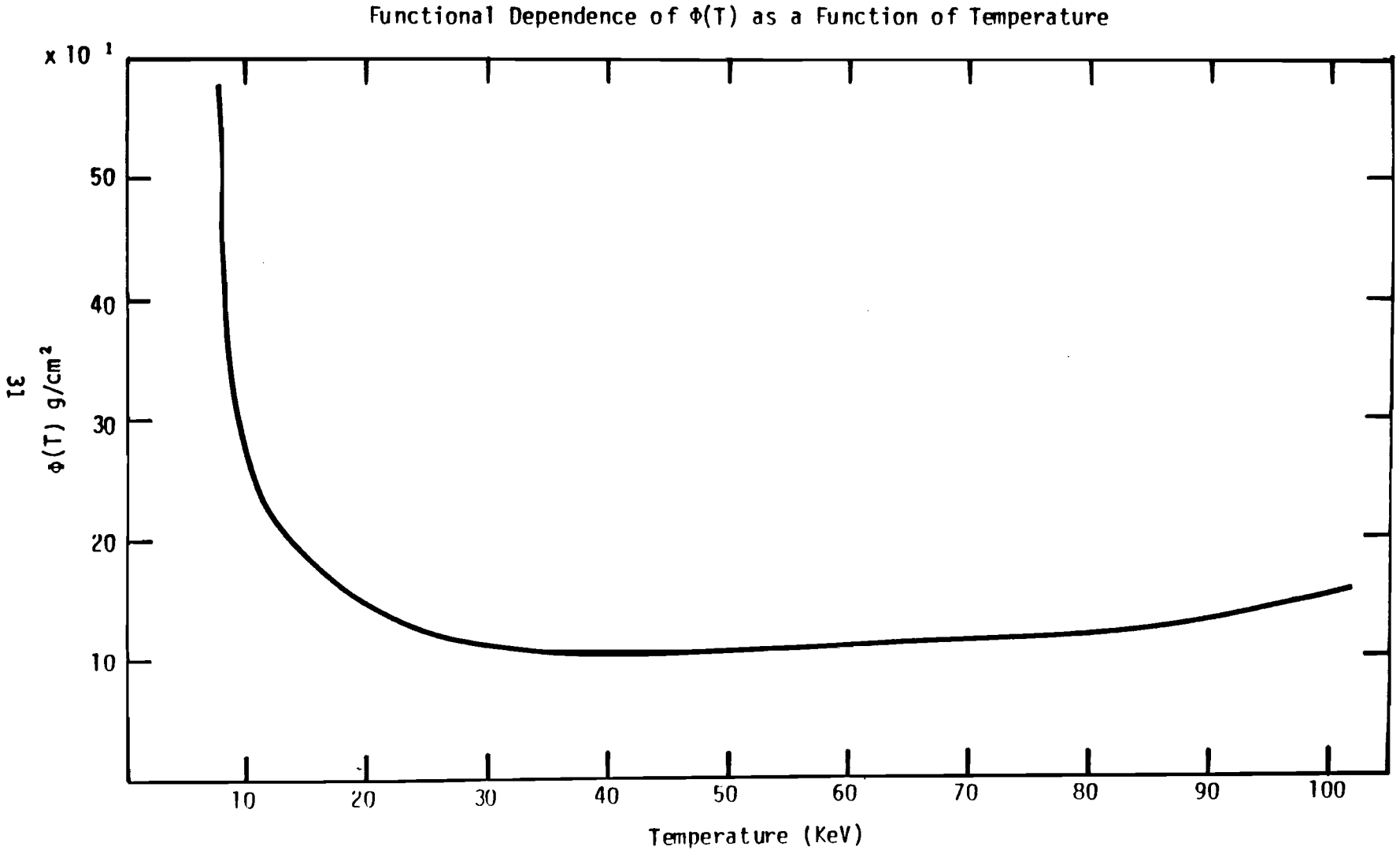
Functional Dependence of Φ(T) as a Function of Temperature
x 10 ¹
50
40
30
20
10
Φ(T) g/cm²
31
10
20
30
40
50
60
70
80
90
100
Temperature (KeV)

Figure 2.3

As will be discussed in the next section, the degree of self-heating is also a function of fuel ρR.

D. Self-Heating

Various factors, such as technological constraints on laser output energy and target gain performance, require the use of DT alpha particles to deposit their kinetic energy back into the plasma to achieve ignition. It is therefore of interest to measure the degree of self-heating so that the constraints on the above factors can be better understood. As will be shown, the degree of self-heating is a function of both fuel ρR and electron temperature.

To estimate the self-heating it is necessary to understand the mechanism in which charged particles lose energy in plasmas. The most important mechanism for low velocity particles (i.e., $\lesssim 10^9$cm/sec) is the direct exchange of energy through coulomb scattering of the test particle off the surrounding field particles. The number of field particles participating in the energy exchange process is dictated by the minimum and maximum impact parameters. These parameters are by no means trivial to deduce, and various models have been used to estimate them.[11] Fortunately, these parameters enter only as a ratio in a coulomb log term and in most cases does not alter the estimate for the energy loss significantly.

Denoting Log Λ as the coulomb logarithm, a test particle (in this particular case a DT alpha particle) of velocity V and mass $M\alpha$ travels

through a plasma whose field particles have a characteristic temperature T. The energy loss takes the forms[12]

$$\left(\frac{dE}{dr}\right)_{ion} = -\frac{4\pi \, Log\Lambda}{M_i V^2} (Z_\alpha e^2)^2 n_i \left[\phi(x) - \left(1 + \frac{M_i}{M_\alpha}\right) x \frac{d\phi}{dx}\right] \qquad (2\text{-}20a)$$

$$\left(\frac{dE}{dr}\right)_{e} = -\frac{4\pi \, Log\Lambda}{M_e V^2} (Z_\alpha e^2)^2 n_e \left[\phi(y) - \left(1 + \frac{M_e}{M_\alpha}\right) y \frac{d\phi}{dy}\right] \qquad (2\text{-}20b)$$

where

$$X \equiv \sqrt{\frac{M_i}{M_\alpha} \frac{E}{kT}} \qquad Y \equiv \sqrt{\frac{M_e}{M_\alpha} \frac{E}{kT}} \qquad (2\text{-}20c)$$

$$\phi(z) \equiv \frac{2}{\sqrt{\pi}} \int_0^z \exp(-\xi^2) d\xi \qquad (2\text{-}20d)$$

Equations (20a) and (20b) are the contributions to the total energy loss from ion and electron field particles, respectively M_i and M_e are the ion and electron field particle masses, respectively.

For the temperature range between 3 KeV <kT< 50 KeV, the parameters x and y satisfy the following conditions:

(1) $x > 1$

(2) $y < 1$

It is assumed here that the energy of the alpha particle remains above 50 KeV. Under such conditions the expressions bracketed in equations

(20a) and (20b) can be simplified; namely,

$$\phi(x) - (1 + \frac{M_i}{M_\alpha}) \times \frac{d\phi}{dx} \simeq 1 \qquad (2\text{-}21a)$$

$$\phi(y) - (1 + \frac{M_e}{M_\alpha}) \, y \, \frac{d\phi}{dy} \simeq \frac{4}{3\sqrt{\pi}} y^3 \qquad (2\text{-}21b)$$

If one forms the ratio of the energy loss of electrons to ions for the case of the 3.5 MeV alpha particle, then

$$(\frac{dE}{dr})_{electron} / (\frac{dE}{dr})_{ion} = \frac{4}{3\sqrt{\pi}} (\frac{M_e E}{M_\alpha kT})^{3/2} \frac{M_i}{M_e} \qquad (2\text{-}22)$$

Taking for example an electron fuel temperature of 10 KeV, this ratio equals

$$\frac{(\frac{dE}{dr})_{electron}}{(\frac{dE}{dr})_{ion}} = \frac{4}{3\sqrt{\pi}} (\frac{.511}{3727} \frac{3.5}{.01})^{3/2} \frac{2349}{.511}$$

$$\simeq 36$$

where all masses have been expressed in MeV. This clearly shows that the predominate energy loss is due to the electrons. Therefore, one can neglect the ion contribution for electron temperature less than about 40 KeV.

Equation (20b) can be directly integrated to yield

$$E = E_o \, (1 - \frac{\rho R}{\widetilde{\rho R}})^3 \qquad (2\text{-}23)$$

where

$$\widetilde{\rho R} \equiv \frac{15}{4\pi^{3/2}} \; M_p \left(\frac{M_p}{M_e}\right)^{1/2} \left(\frac{E_o \; (kT)^3}{Z_\alpha^2 \; n_e \; e^4 \; \mathrm{Log}\Lambda}\right) \qquad (2\text{-}24)$$

The significance of ρR is that it is the ρR required to stop the alpha particle. This term is a strong function of electron temperature and a weak function of electron density. Therefore, the energy of an alpha particle can be expressed in terms of the ρR tranversed by the alpha particle and the temperature of the electrons.

Using equation (23) and summing over the fuel volume, it can be shown that the fractional energy loss of the alpha particles η is given by[13]

$$\eta = \frac{\rho R}{\widetilde{\rho R}} \left[\frac{3}{2} - \frac{4}{5} \left(\frac{\rho R}{\widetilde{\rho R}}\right)\right] \qquad (2\text{-}25a)$$

$$\sim \frac{3}{2} \; \frac{\rho R}{\widetilde{\rho R}} \quad \text{for } \rho R << \widetilde{\rho R} \qquad (2\text{-}25b)$$

This assumes that the alpha particles are created uniformly and isotropicly throughout the fuel and that the particle range is much larger than the dimension of the fuel. It is also assumed in the calculation that the electron temperature is both spatially and temporally constant during the burn. This clearly is not the case when the fuel ρR becomes larger than $.1 g/cm^2$, for then the alpha particles heat locally the electrons, thereby reducing their stopping power. This in turn leads to larger particle ranges

causing localized ignition which grows spatially with time. These limitations on equation (25) are not, however, presently experienced since attainable ρR conditions do not exceed the low $10^{-3} g/cm^2$ regime and equation (25b) applies.

III. EXPERIMENTAL METHODOLOGY - TRACK DETECTOR ANALYSIS

A. Chapter Overview

This chapter is divided into three main sections. In the first section, a discussion on the various background track sources is presented. Here, methods are also described explaining how these background tracks can be identified and discriminated from knock-on tracks. The most difficult background components to discriminate against are protons. This is due to the fact that track diameter alone can not adequately be used to uniquely differentiate protons from knock-on tracks. Therefore, a method is discussed which eliminates this background by relying not only on diameter (which is a function of the particle energy-per-nucleon E/A) but also its range (which is a function of the particle mass). This separation of protons from knock-on particles is possible because of the smaller range protons have in CR-39 for a given velocity. By selecting an appropriately thick detector, protons are stopped within the bulk of the detector while the knock-on particles with larger ranges traverse the detector (see Figure 3.4) producing spatial coincident tracks. By accepting spatial coincident tracks over a given diameter interval separation is possible over a finite energy span.

Experimental verification of the above methods is presented in the second section where it will be shown that proton tracks can be successfully separated from knock-on tracks. This is demonstrated by measuring the knock-on particle spectrum over an extended energy interval.

The remaining supportive section discusses the detail calibration of the track detector. Its purpose is to give those readers interested, further details on how the track criteria are developed. Details on the particular energy-diameter response functions for knock-on and background particles are given. Also details on the diameter spread for a given incident particle are discussed.

B. Track Identification Methodology

1. Background Sources

In general, background tracks arise from intrinsic and extrinsic sources. The former results during the initial casting of the track detector. This background is characterized by a large number of shallow, low-contrast pits (usually less than 8 μm in diameter) with circular cross sections. Figure 3.1 shows these structures after a standard etch. These imperfections are the result of a tendency during the polymerization process to accumulate localized regions of high density cross-linking. These regions called "crosslink clusters" alter the local etch rate which produce the track-like structure. Recently, a new improved CR-39 detector has been developed based on the addition of 1% of a plasticizer, dioctyl phthalate, to the monomer. This plasticizer greatly reduces the tendency for crosslink cluster formation. It is hoped that future improvements in the sensitivity of this detector will expedite the data acquisition in later knock-on experiments.

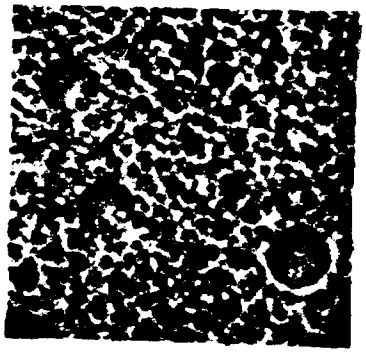

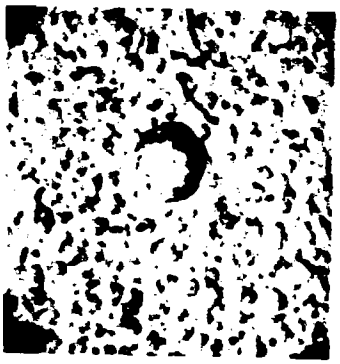

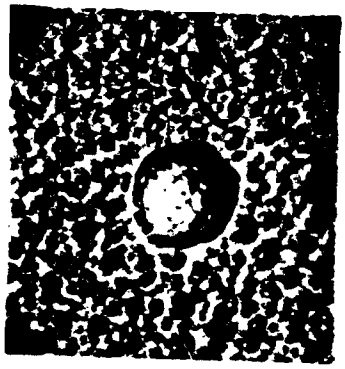

Figure 3.1

Extrinsic background sources arise from (n, p) and (n, α) reactions which occur during the knock-on measurement as well as from the decay of Rn^{222} (an alpha particle emitter found naturally in the atmosphere) during the storage of the track detector. As will be shown in the next section, alpha particle track diameters are, in general, much larger than any hydrogen isotope tracks. This results from the fact that the restricted energy loss (REL) for the alpha particles is larger than that of hydrogen isotopes because of its larger z value. Therefore, on the basis of track diameter alone, alpha particle tracks can be separated from knock-on particle tracks.

Various sources contribute to a proton background, as summarized in Figure 3.2. Table 3.1 below lists the dominant (n,p) sources with their corresponding cross section for 14 MeV neutrons[13].

Table 3.1

(n,p) Proton Background Sources

Location	Reaction	Cross Section (mb)
Fuel	D(n, 2n)p	280
Tamper	Si^{28} (n,p)$A\ell^{28}$	160 ± 16 (E_p>2.9 MeV)
	O^{16} (n,p) N^{16}	45
	Ca^{40} (n,p) K^{40}	295 ± 38
Tantalum	Ta^{181} (n,p) Hf^{181}	3.2
N_2	N^{14} (n,p) C^{14}	77
O_2	O^{16} (n,p) N^{16}	45
CR-39	H (n,p) n'	620

KNOCK-ON DETECTION AND BACKGROUND SOURCES

UR LLE

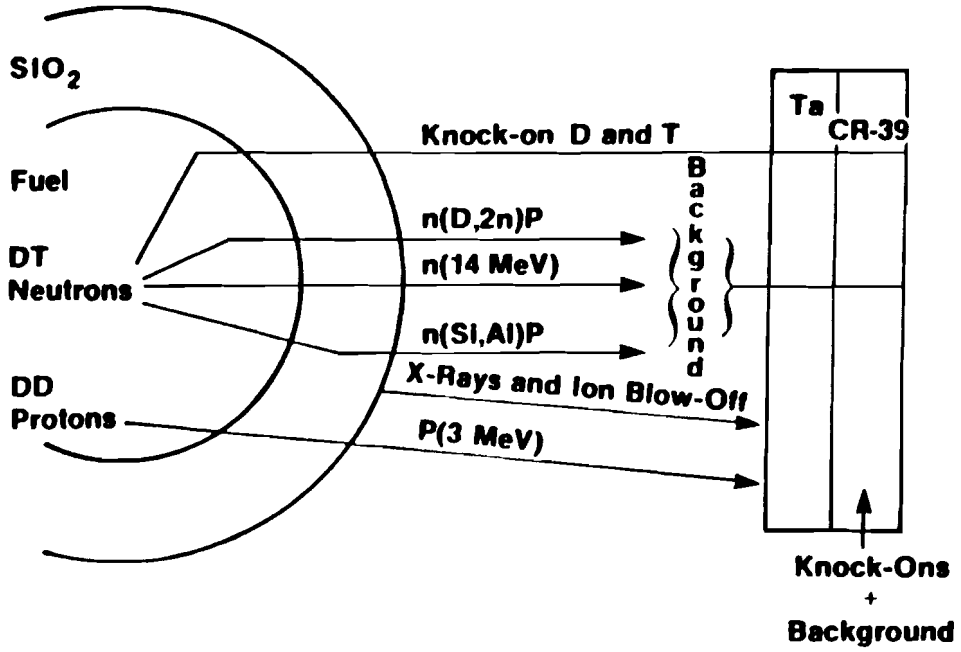

E1462

Figure 3.2

In addition to the above nuclear reactions, energetic protons produced as a result of hot electrons may achieve high enough energies to traverse the tantalum foil and produce tracks in CR-39. This background has not been observed on the University of Rochester's Zeta or Omega laser system for uniform illumination.

One final point to be made concerning the proton background is that the track contribution due to hydrogen recoils in CR-39 can be easily discriminated from the knock-on particles. Protons which are forward scattered possess energies (i.e. $\gtrsim$ 8 MeV) well above registration energy of the detector.

Estimates for the signal-to-background ratio (see Appendix C) shows a 5:1 ratio. This ratio reflects the most pessimistic situation where protons cannot be separated from the knock-on signal by any means. The signal-to-background can be greatly improved by applying three track criteria which will now be developed.

As shown in Section D of this chapter, hydrogen isotopes with equal velocity (or equivalently $^{E}/A$) greater than 6.5 x 10^{8}cm/sec (i.e., $^{E}/A$ = 2.0 MeV) all have approximately equal track diameters that is D = f (v) where D is the track diameter and f is a function of velocity. As the velocity of these isotopes decrease, their corresponding track diameter increase. This results from the fact that the track-etch rate is a function of the local energy loss of the charge particles. Over the energy interval of interest, the energy loss is inversely proportional to the square of the velocity. Therefore, the smaller the velocity, the larger the damage

produced along the latent tracks. The greater the damage produced along the track the larger the ultimate track diameters will be after etching. For an $^{E}/A$ less than 2 MeV/nucleon, the diameter is no longer strictly a function of velocity. This is due to the fact that the energy loss changes differently along the etched track for each of the isotopes. This variation in track diameter for each isotope is illustrated in Figure 3.3. Here the shaded region represents the relative amount of damage produced by the charged particle inside the detector. For $^{E}/A$ values greater than 2 MeV/nucleon the damage is essentially constant over the length of the etched track and thus the resulting diameters are equal. For $^{E}/A$ values less than about 2 MeV there is sufficient lateral variations in the damage region to produce differences in track diameter. This is the direct result of energy loss variations along the etched portion of the track. The track diameter variations are less than ± 5% for energy-per-nucleon greater than 2 MeV.

Although track diameter in itself does not help in the separation of the proton background, it does establish the particle's $^{E}/A$. Unlike alpha tracks which have track diameters well in excess of those of hydrogen isotopes, another criterion is required to establish the particle nucleon number. This information can be extracted if the particle range is known.

To within ± 4% the range of a hydrogen isotope can be simply related to the range of a proton by[15]

$$R_I\ (^{E}/A) = A\ R_p\ (E) \qquad (3\text{-}1)$$

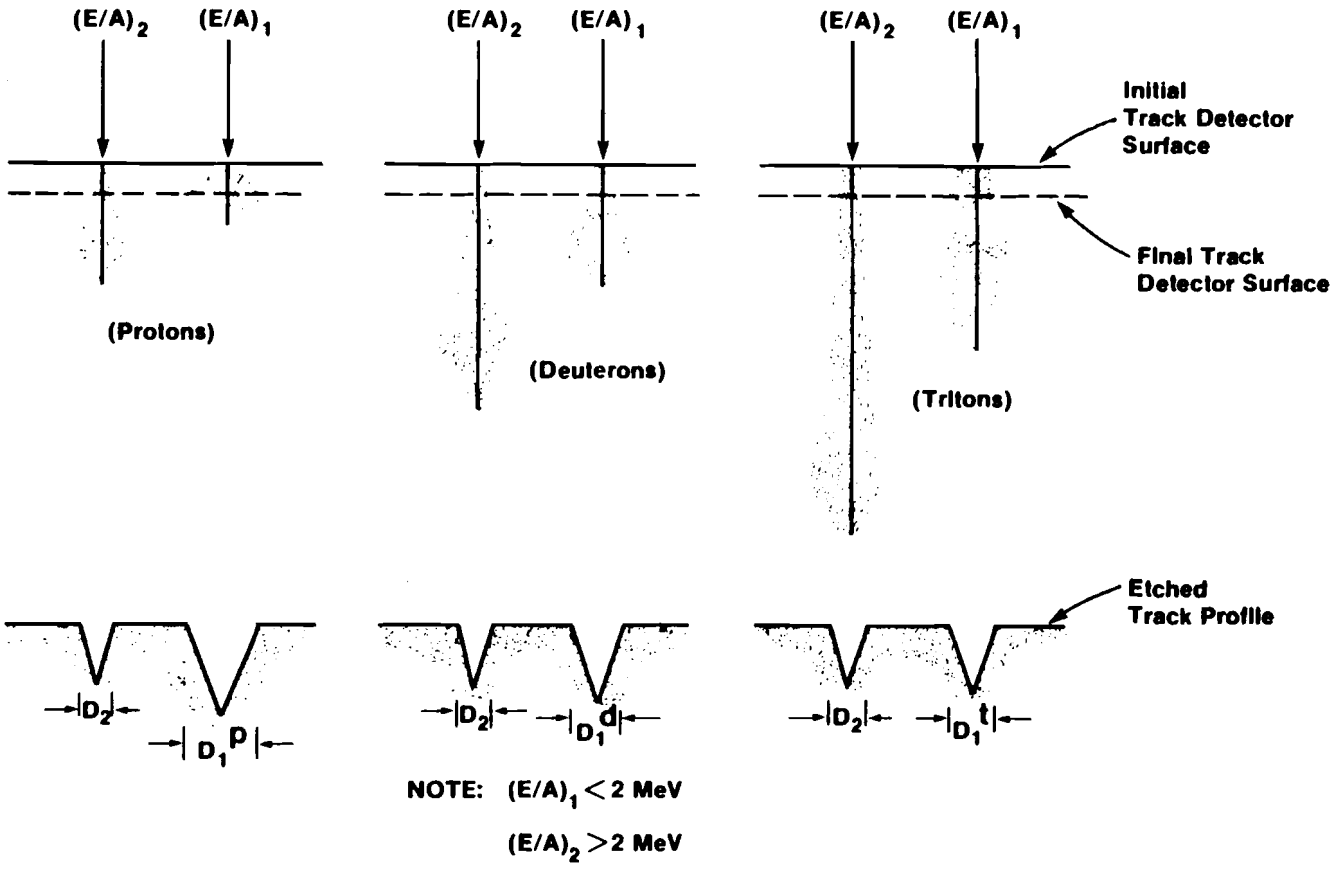

E1831

Shaded region indicates the amount of local damage produced by the charged particles

Figure 3.3

where R_I and R_p are the ranges of the isotope and proton, respectively, and A is the nucleon number for the isotope. Therefore, by measuring the track diameter one can deduce E/A; by measuring the range one can deduce A. Part 2 of this section will now discuss the experimental details of how this range measurement is performed.

2. The Spatial Coincident Criteria

One need not require the separation of deuterons and tritons per se in order to measure the fuel ρR. What is required, however, is the ability to discriminate the proton tracks from the knock-on tracks. This can be achieved by adjusting the detector thickness so that protons in a given E/A interval (or equivalently, diameter interval) do not have adequate range to traverse the thickness of the detector. Only a single track appears on the detector's front surface. On the other hand, deuterons and tritons with larger ranges can traverse the detector leading to a track both on the top surface as well as the bottom surface of the detector. These "spatial track coincidences" are the signatures required along with the knowledge of the top surface diameter to discriminate proton-produced tracks from deuteron and triton-produced tracks. Figure 3.4 summarizes the basic physics leading to the production of spatial coincident tracks. Here proton separation is possible since below a certain energy E*, or equivalently for diameters greater than D*, protons no longer have adequate range in the detector to produce spatial coincident tracks. Deuterons and tritons having larger masses, do however, produce coincident tracks with diameters greater than D* because

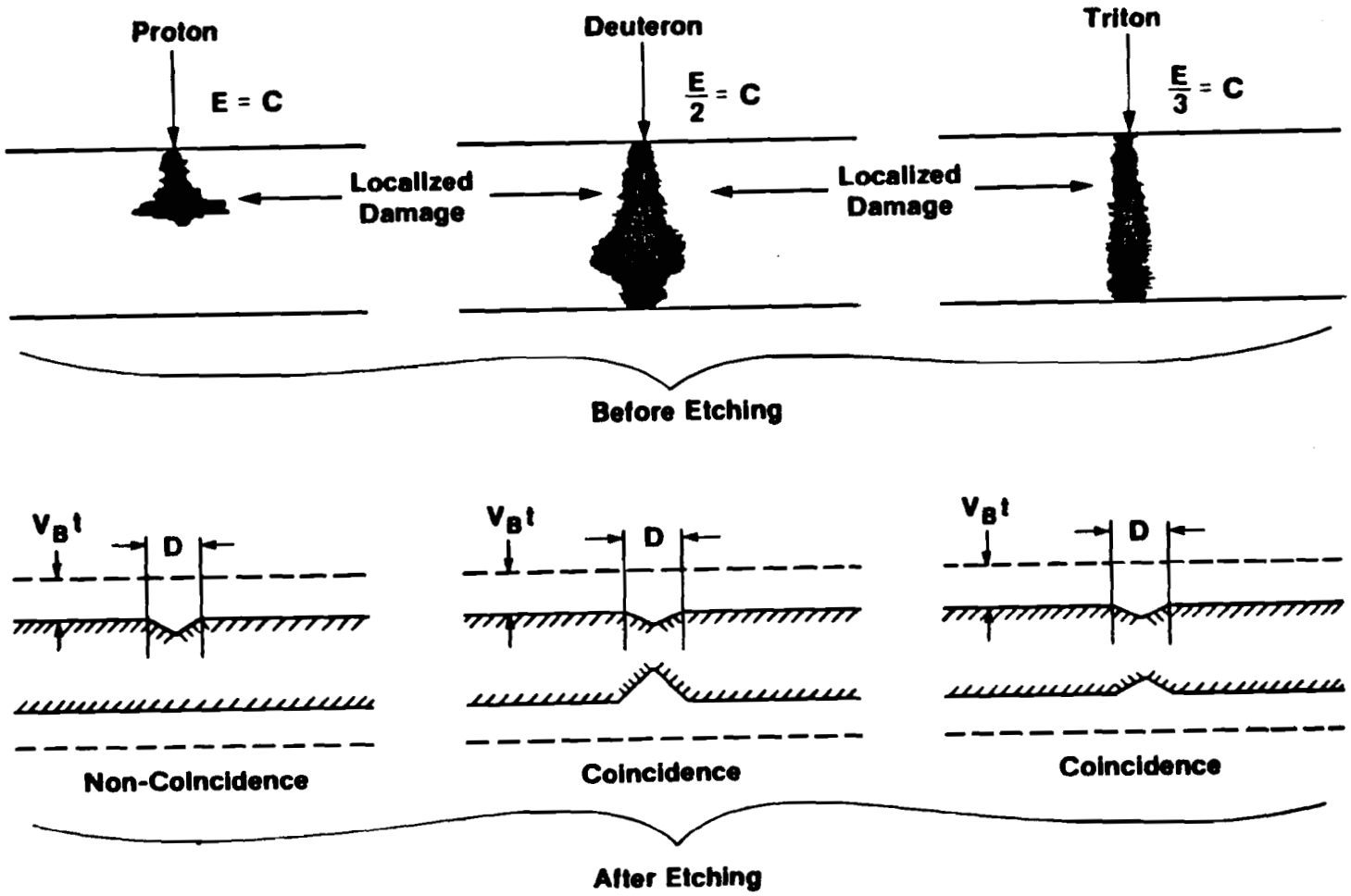
Proton
E = C
Deuteron
E/2 = C
Triton
E/3 = C
Localized Damage
Localized Damage
Before Etching
VBt
D
VBt
D
VBt
D
Non-Coincidence
Coincidence
Coincidence
After Etching
E1457
$R_A^Z(E/A) = \frac{A}{Z^2} R_{Proton}(E)$

Figure 3.4

of their larger ranges in the track detector. Figure 3.5 gives the minimum coincident track diameter (D*) as a function of detector thickness after etching.

The optimal detector thickness ranges from 110 μm to 170 μm. Detectors with thicknesses less than 110 μm suffers from two important effects. First, the registration efficiency is not constant from sample to sample. Some detectors were found not to record proton tracks at all. Second, detectors with thicknesses less than 110 μm will allow protons with energies of less than 2 MeV to produce spatial track coincidences. This complicates the analysis since track diameter is no longer strictly a function of velocity.

Detectors with thicknesses greater than 170 μm results in a diameter acceptance interval where track diameters are very small and have low contrast with respect to the surrounding field of view. Therefore, in the scanning process it becomes difficult to count all coincident tracks.

In summary, two criteria are helpful in experimentally separating background protons from knock-on tracks are (1) to look for spatial track coincidences and (2) to impose the constraint that the top surface diameter be greater than D*.

Not all proton tracks are eliminated by the above two criteria. It is still possible to confuse back-scattered proton tracks as knock-on tracks. By back-scattered tracks it is meant, those track coincidences arising from the passage of a charged particle from the back surface of the track detector to its front surface. These protons can be generated by (n,p) reactions arising in the Omega structure.

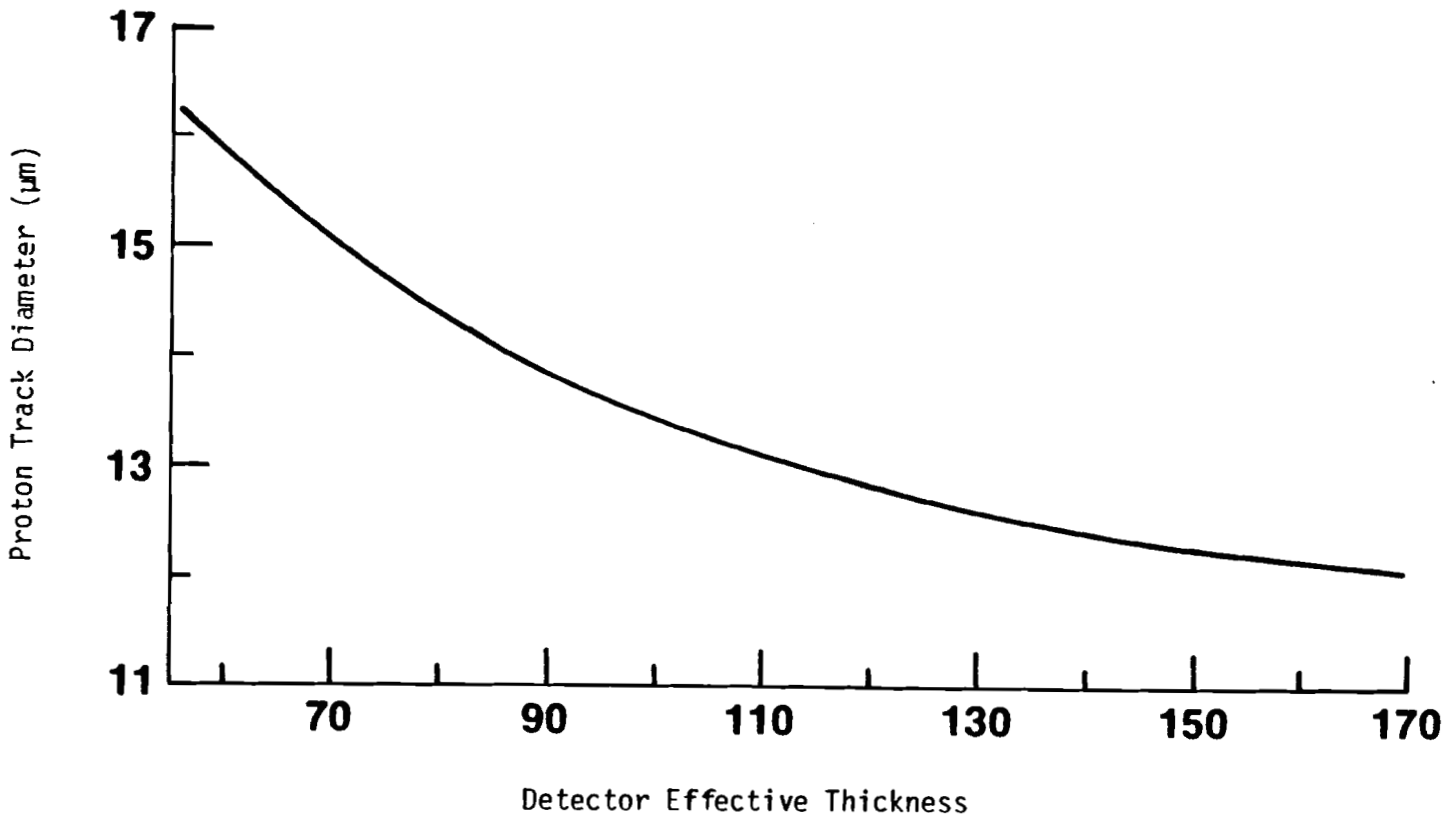

E1647

Figure 3.5

This complication can be resolved by rejecting back surface diameters which are less than D*. This criterion eliminates the energetic back-scattered protons (i.e., protons with ranges greater than the track detector effective thickness χ_{eff} equal to $\chi_o - V_g t$ where χ_o is the initial track detector thickness). Protons with less energy than required to traverse χ_{eff} will not produce coincident tracks and are automatically rejected. By adopting this criterion, the price one pays is the rejection of a small fraction of the knock-on particles.

Figure 3.6 shows the region where knock-on particles will produce bottom track diameters less than D*. The width of this region can be estimated by assuming a linear variation of track diameter, D_b, with Δr. The maximum back-surface knock-on diameter, $\hat{D}$, will occur if the knock-on particle range is equal to χ_o (i.e., $\Delta r = 0$). If the knock-on particle is of lesser energy, the bottom track diameter will be less than $\hat{D}$ (i.e., $0 < \Delta r < v_g t$). For the extreme case where the particle range approaches χ_{eff}, the back surface diameter approaches zero (i.e., $\Delta r \rightarrow v_g t$). Thus D_b can be estimated as

$$D_b \simeq \hat{D} \left(1 - \frac{\Delta r}{v_g t}\right) \qquad (3\text{-}2)$$

For separation, one requires that $D_b > D^*$. This results in

$$\Delta r < v_g t \left(1 - \frac{D^*}{\hat{D}_b}\right) \qquad (3\text{-}3)$$

TRACK FORMATION IN A SOLID STATE TRACK DETECTOR

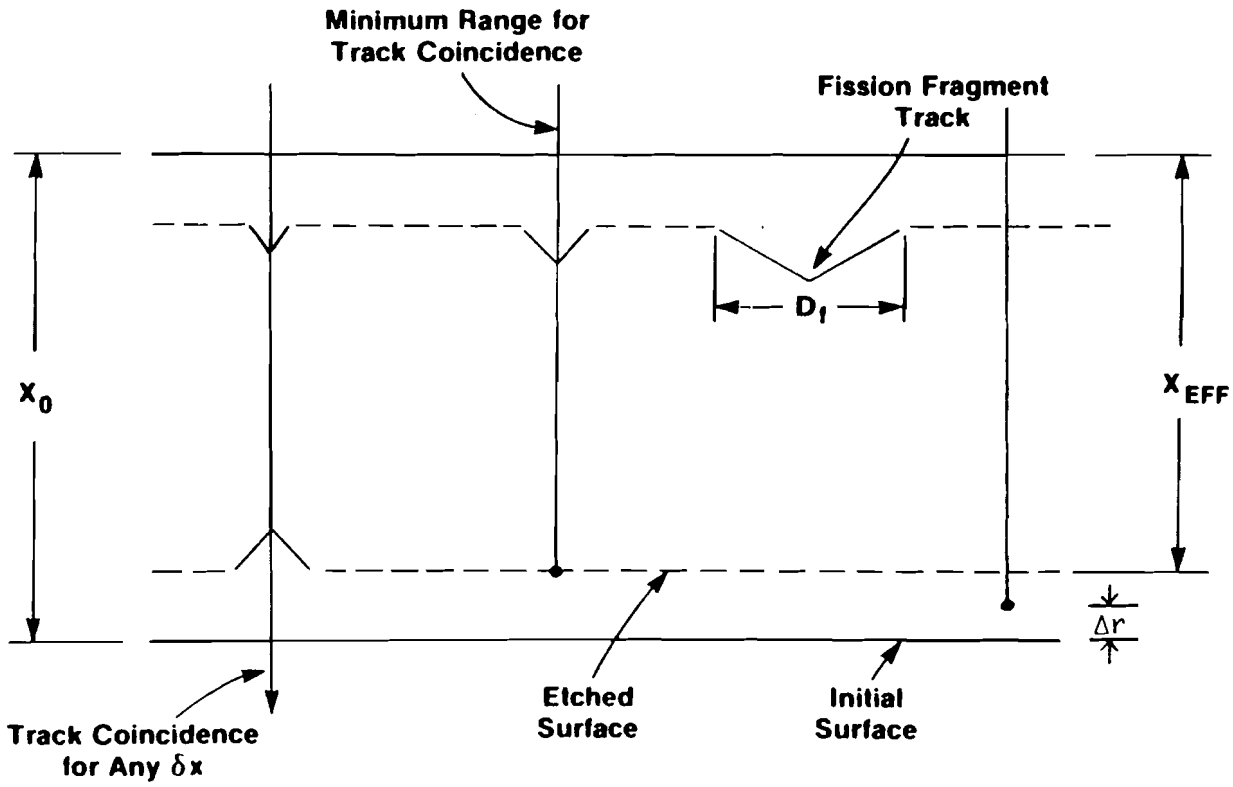

Figure 3.6

The ratio $D^*/\tilde{D}_b$ is approximately equal to 0.5 for track detectors measuring initially 150 μm in thickness. Also the term $v_g t$ can be directly obtained by irradiating a small area of the track detector to fission fragment tracks and measuring their diameters (i.e., $D_\delta \simeq 2\ v_g t$ see Appendix A). (In the present experiments, D_δ varied from 44 to 48 μm. Taking the mean value of 46 μm equation (3) requires that $\Delta r < 12.5$ μm). Therefore, knock-on particles must have ranges $R_{e\delta\delta}$, greater than

$$R_{e\delta\delta} \gtrsim T - \frac{1}{2} D_\delta \left(1 - \frac{D^*}{\tilde{D}}\right) \qquad (3\text{-}4)$$

In summary, the set of track criteria developed to separate the proton background from knock-on particles are

(1) count only spatial coincident tracks
(2) reject tracks with top surface diameters less than D*
(3) reject tracks with bottom surface diameters less than D*

C. Track Discrimination Criteria: Experimental Verification

In the last section a method was discussed, based on three track criteria, to separate proton tracks from deuteron and triton tracks.

This section will present experimental verification of this method by measuring the knock-on energy spectrum over a wide range of energies.

The measurement was performed by integrating the signal over two high yield shots. Laser intensity on target was $\sim 10^{16}$ W/cm^2 and had a full width at half maximum of $\sim$ 75 psec. Targets consisted of 200 μm diameter glass walled microballoons filled with equimolar deuterium-tritium fuel at 20 atmospheres. More details of the experimental set-up is discussed in Chapter 5.

The spectral measurement involves the placing of five different thicknesses of tantalum foil in front of 150 μm thick CR-39 track detectors. The stopping foil thicknesses are chosen to maximize the dominant features of the knock-on spectrum as shown in Figure 3.7a. The 50 μm and 115 μm tantalum foils approximately centers the triton and deuteron peaks in their respective energy acceptance window of the detector. The valley region between these peaks is sampled with the 75 and 95 μm tantalum foils. A 160 μm foil is placed over one track detector as an additional check to test one's ability to discriminate against protons. This foil stops all knock-on particles from reaching the track detector. A signal measured on it would indicate that the three track criteria are not adequate to reject all proton tracks.

As will be shown in Chapter V, the value for D* used in the discrimination process is equal to $\sim$12 μm. The relative number of spatial coincident tracks satisfying the three criteria is compared with the predicted spectrum shown in Figure 3.7b. Details related to the calculation of the predicted spectrum are examined in Chapters IV and V.

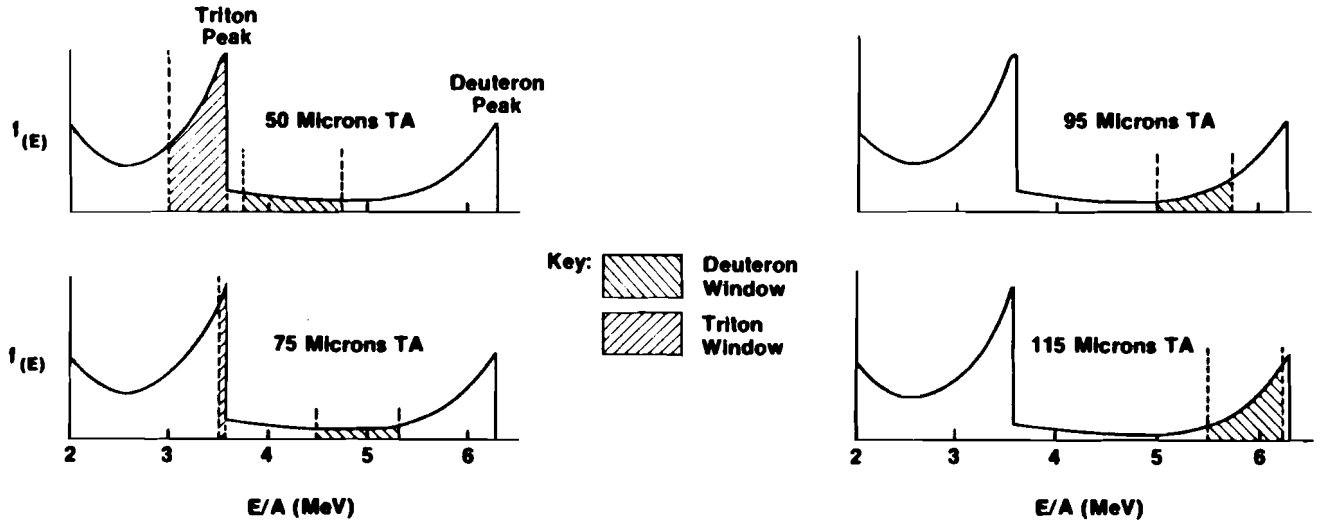
Triton Peak
Deuteron Peak
50 Microns TA
95 Microns TA
75 Microns TA
115 Microns TA
f(E)
Key:
Deuteron Window
Triton Window
2
3
4
5
6
E/A (MeV)

(a)

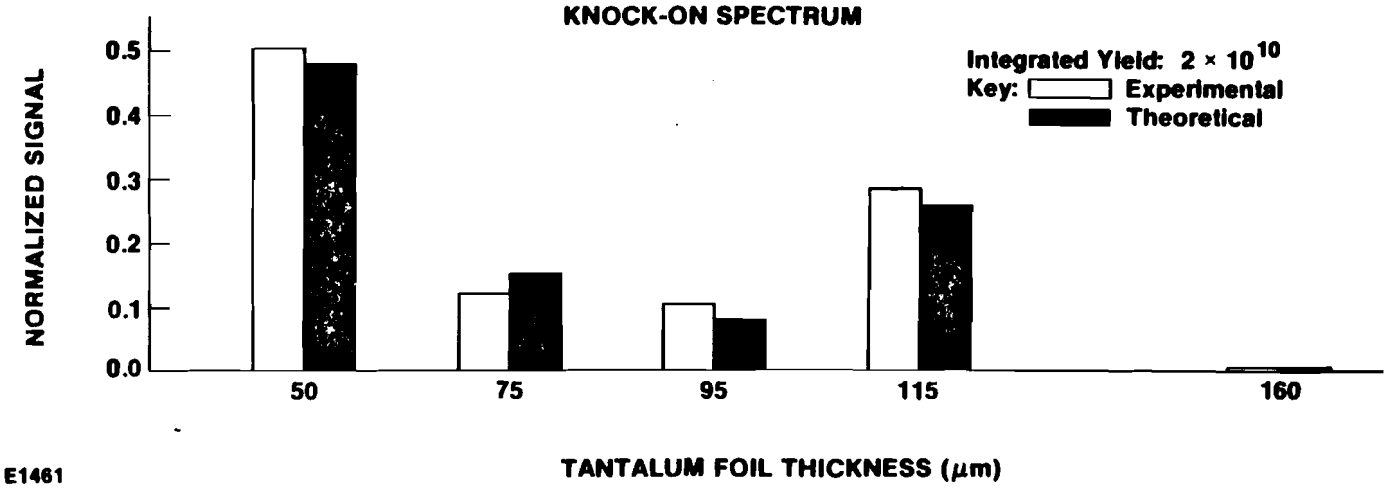
KNOCK-ON SPECTRUM
Integrated Yield: 2 × 10^10
Key: Experimental
Theoretical
NORMALIZED SIGNAL
0.0
0.1
0.2
0.3
0.4
0.5
50
75
95
115
160
TANTALUM FOIL THICKNESS (μm)
E1461

(b)

Figure 3.7

The data was obtained by integrating over two target shots (shot number 6037 and 6038) to increase the counting statistics. Even so, the uncertainty remained large. The absolute counts on each detector along with their corresponding statistical uncertainty is summarized in Table 3.2 as shown on the next page. Notice, however, that the statistical uncertainty is not large enough to wash out the observed peaks. In addition, the 160 μm tantalum foil detector package shows no knock-on coincident-like tracks. The good agreement in the measured and predicted knock-on spectrum along with the absence of any tracks meeting the three acceptance criteria on the 160 μm foil system strongly suggest that the discrimination method is adequate in separating proton from knock-on tracks. Further evidence of the validity of this method will be presented in Chapter V when details of the internal diameter distribution in a given energy window is examined.

D. Track Detector Calibration

1. Section Overview

As briefly discussed in Section B, the track criteria are based on experimental data which show that track diameter is a function of $^{E}/A$ and does not depend on particle type (at least for $^{E}/A$ values greater than 2 MeV). This section examines the details of the track diameter-energy response curves for each of the hydrogen isotopes and for alpha particles. Track diameter

Table 3.2

Knock-on Spectral Data

Tantalum Foil Thickness (μm)	Deuteron (triton) Lower Energy Window Limit (MeV)	Deuteron (triton) Upper Energy Window Limit (MeV)	Number of Tracks Counted	Statistical Count Uncertainty	Predicted (measured) Normalized Signal
50	7.7, (8.9)	9.4, (>10.6)	25	± 5	.457, (.510)
75	9.0, (10.5)	10.6, (>10.6)	6	± 2	.137, (.122)
95	10.0, (>10.6)	11.6, (>10.6)	4	± 2	.100, (.082)
115	11.0, (>10.6)	12.4, (>10.6)	15	± 4	.306, (.286)
160	>12.5, (>10.6)	>12.5, (>10.6)	0	---	.000, (.000)

smearing will also be addressed here. Lastly, it examines a calibration procedure used to correct for bulk etch differences between detectors.

2. The Calibration Experiment

A series of controlled particle exposures on CR-39 was performed to establish the diameter-energy response function for hydrogen isotopes and alpha particles. These exposures were obtained with the use of an Edge Split Pole spectrometer at the Nuclear Structure Research Laboratory at the University of Rochester. Specific energies were obtained by accelerating the particles to a final energy E_o and then scattering them off a platinum mesh. The spectrometer placed after the mesh, selected the desired particle energy which was to strike the track detector by varying the field strength of the bending magnet. Energy selection ranged from about zero to E_o, and the energy variation across each detector was estimated to be no greater than 5 KeV.

A special procedure was required to generate the triton particle source. Specifically, a deuteron beam was incident on a ^{13}C mesh placed in front of the spectrometer which through a pick-up reaction produced the triton source.

Each detector was mounted on a 45^{o} wedge to insure that the particle flux was perpendicular to the detector surface. Five samples were mounted on a six-faced rotational drum (i.e., a Geneva

Device) where the sixth face was reserved for a solid state detector to monitor the beam flux.

After the exposure each detector was first exposed to an Am^{241} alpha source over a limited area of the track detector so as to not confuse the particle tracks. Next, the detectors were etched in 6.25 N NaOH solution for 16 hours at $70^{o}C$ (henceforth referred to as a "standard etch").

Each sample was examined under a Leitz optical microscope and photographs were taken of each sample's track diameter to establish the mean and the standard deviation of this parameter. The standard deviation was measured to be about .5 μm. Figure 3.8 shows the typical high degree of uniformity of track diameter for 1 MeV protons as well as the diameter distribution.

Extensive data taken over a wide range of proton energies reveal that energy resolution can be as high as 150 KeV for protons with energies of about 1.5 MeV (See Figure 3.9). It does, however, deteriorate somewhat at higher energies and reaches ± 250 KeV at 3 MeV. (Comparisons with deuteron and triton data will be given later in this section.)

As briefly mentioned, the bulk etch rate has been noticed to vary somewhat from sheet-to-sheet. This variation will alter the measured proton track diameter from detector to detector. Therefore, it is necessary to correct for this variation by defining a standard bulk etch rate and normalizing all data to this reference. A good approximation to the variation of V_g can be determined by measuring

A1.5 MeV PROTON DIAMETER DISTRIBUTION

UR LLE

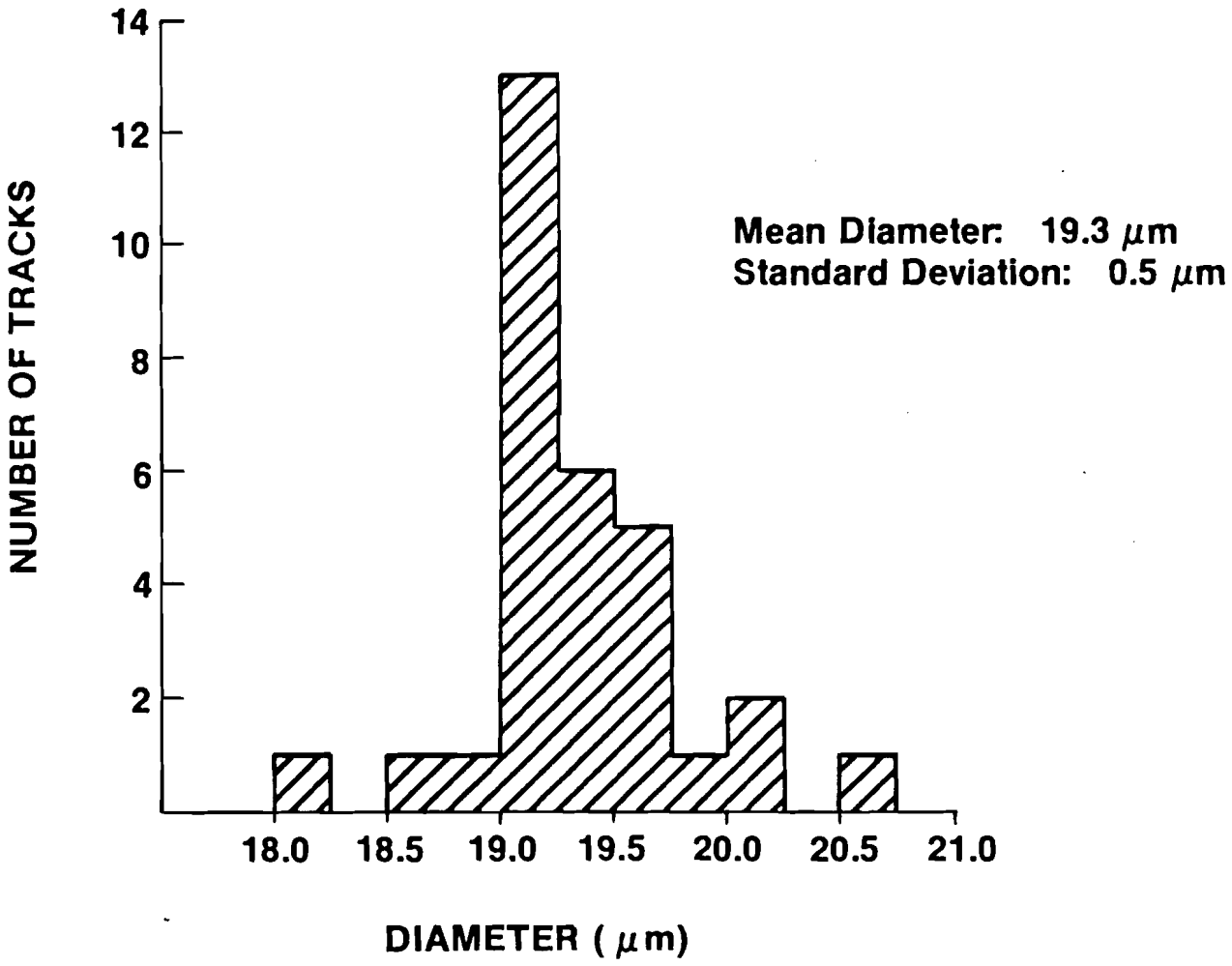

E1817

Figure 3.8

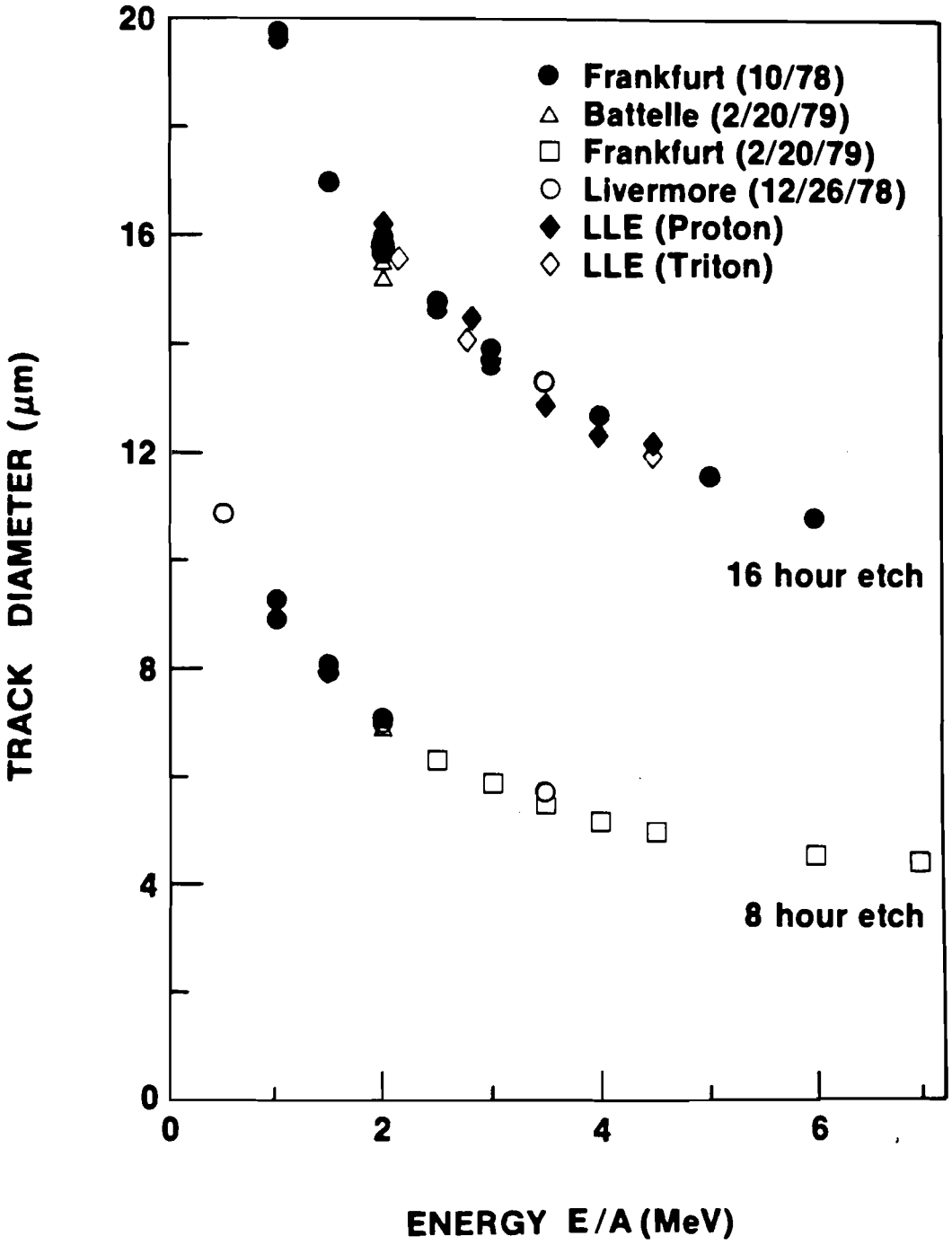

E1637

Figure 3.9

the diameter variation of alpha particle tracks (later in the investigation a Cf^{252} fission source was used). In Appendix A it is shown that the track diameter is given by

$$D(t) = 2 v_g t\left[\frac{V - 1}{V + 1}\right]^{\frac{1}{2}} \qquad (3\text{-}5)$$

where V is the track-to-bulk etch ratio, and observing from Figure 3.10 that the alpha track diameter is nearly insensitive to energy strongly suggest that the alpha particle track-to-bulk etch ratio (V_α) is large. Thus the alpha track diameter (D_α) is approximately equal to $2 v_g t$. Thus, by measuring the variation of the alpha track diameter, one can calculate the variation in the bulk etch rate. This bulk variation information can be used to correct for proton track diameter variation by use of equation (5). If the track etch rate is a function only of the number of bonds broken, then the track etch rate will not vary between sheets of CR-39. Let $D\alpha$ denote the measured alpha particle diameter on a given detector and $\hat{D}\alpha$ a reference alpha track diameter. Then the proton etch ratio V_p can be related to a reference proton etch ratio $\hat{V}_p$ by

$$V_p = \frac{\hat{V}_T}{V_g} = \frac{\hat{D}_\alpha}{D_\alpha}\hat{V}_p \quad \text{where } \hat{V}_p \equiv \frac{\hat{V}_T}{\hat{V}_g} \qquad (3\text{-}6)$$

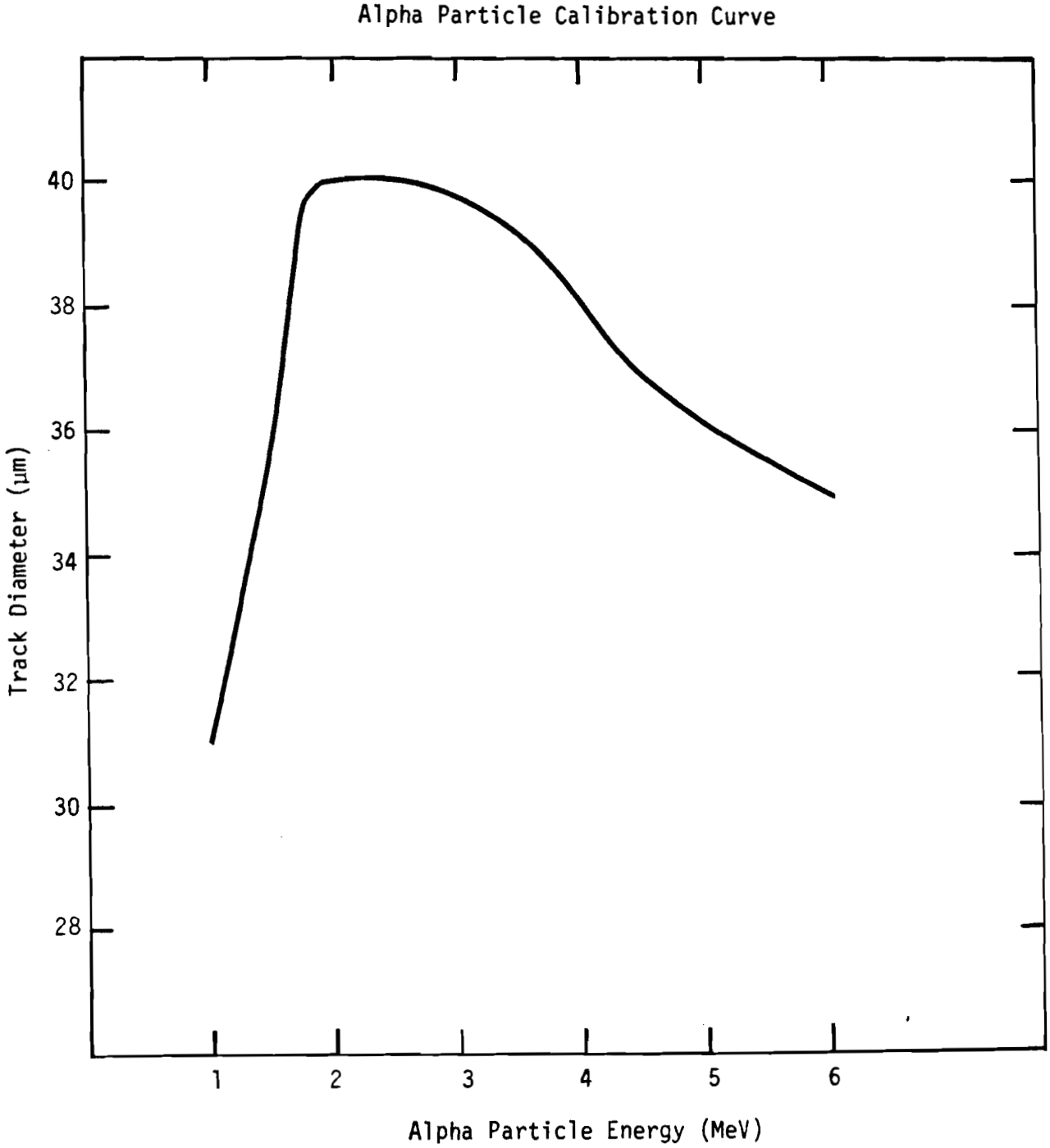
Alpha Particle Calibration Curve
Track Diameter (μm)
40
38
36
34
32
30
28
1
2
3
4
5
6
Alpha Particle Energy (MeV)

Figure 3.10

$$= \gamma \hat{V}_p \tag{3-7}$$

where γ is defined as the standard-to-measured alpha track diameter ratio. If D_p and $\hat{D}_p$ represents the measured proton diameter and reference diameter, respectively, then

$$\hat{D}_p = \left[\frac{\hat{V}_p - 1}{\hat{V}_p + 1} \Big/ \frac{\gamma\hat{V}_p - 1}{\gamma\hat{V}_p + 1} \right]^{\frac{1}{2}} D_p \frac{\hat{D}_\alpha}{D_\alpha} \tag{3-8}$$

$$\simeq D_p \gamma \left[1 + \frac{1}{2} \frac{(\gamma-1)\hat{V}_p}{\hat{V}_p - 1}\right] \tag{3-9}$$

The term γ ranges from about .9 to 1.1 while $\hat{V}_p$ can vary from 1 to about 1.5 for all proton energies. For proton energies less than 3 MeV the second term in equation (9) is small compared with 1 and can be neglected. Therefore, the measured track diameter can be related to a standard track diameter if γ is measured.

An example on how this normalization of the data is applied, consider the specific data generated from a 1.5 MeV proton exposure. Superimposed alpha tracks placed along with the proton tracks reveal an average alpha track diameter of 34 μm. A reference diameter of 36 μm was assumed for all proton, deuteron, and triton data.

γ for this particular detector is thus 1.06. Table 3.3 summarizes the measured and generated proton diameter distribution. The normalized proton diameter from column 3 gives a mean diameter and standard deviation of 19.3 and .5 μm, respectively.

Table 3.3

Proton Calibration Data

Measured Track Diameter (μm) ± .25 μm	No. of Tracks	$\hat{D}_p$ (i.e., γD_p)
17.00	1	18.02
17.25	0	18.29
17.50	1	18.55
17.75	1	18.82
18.00	13	19.08
18.25	6	19.35
18.50	5	19.61
18.75	1	19.88
19.00	2	20.14
19.25	0	20.41
19.50	1	20.67

It is instructive to ask whether such a normalization technique is, in fact, a correct method for scaling track diameter. Presumably it assumes that if a range of proton energies strike the track detector, all could be multiplied by some correction factor so as to then determine their $^{E}/A$. If this is true, then it must also be true that taking the ratio of diameter at two definite energies must be invariant for all sheets. Three series of exposures taken from different sheets of CR-39 have been taken to look at this particular situation.

Below in table 3.4 is a set of raw (unnormalized data) for 1 and 2 MeV protons track diameters and their corresponding ratios.

Table 3.4

Etching Differences of Protons from Different CR-39 Samples

Sheet	Average Diameter (1 MeV) μm	Average Diameter (2 MeV) μm	Diam. (1 MeV) / Diam. (2 MeV)
1	23.5 ± .5	16.8 ± .5	1.40 ± .07
2	18.5 ± .4	13.5 ± .4	1.37 ± .07
3	22.0 ± .5	16.0 ± .5	1.38 ± .07

The ratio from all three sheets strongly supports that the track-to-bulk etch rate ratio is an invariant of the sheet used.

The final measurement which explicitly shows that the normalization method is valid is to compare the variations in alpha particle diameters to those of protons. If the ratio of diameters is invariant

for each separate sheet then a means exists to calibrate any track detector by using a calibrated alpha source. Table 3.5 below shows just that.

Table 3.5

Proton - Alpha Particle Diameter Ratio From Different CR-Samples

CR-39 Sheet	Average Proton Diameter (1 MeV)	Average α-Particle Diameter	Ratio $(\frac{D_\alpha}{D_p})$
1	23.5 ± .5	36 ± .5	1.53 ± .05
2	18.5 ± .4	28 ± .5	1.51 ± .06
3	22.0 ± .5	33 ± .5	1.50 ± .06

Examining the ratio values demonstrate that the alpha particle track diameters serve as a convenient means for calibrating different sheets of CR-39 to a standard reference. It is both simple and direct.

Similar calibration studies have been made for deuterons and tritons. If one plots the diameter as a function of E/A one obtains essentially the same response curve (see Figure 3.8). The small differences arise from simple energy loss arguments as given in Section B. Empirically the calibration curves take the form:

$$D\ (\mu m) = 21.304\ (\frac{E}{A})^{-.4457} \qquad (3\text{-}10)$$

In summary, it has shown that the track diameter is a well-defined function of particle velocity (or $^{E}/A$). The variation in diameter for a given energy is ± .5 μm leading to a reduction in energy resolution, especially at high energies.

Also shown here is that a procedure can be followed to correct for variations in the bulk etch rate between samples. This correction is accomplished with the use of highly ionizing particles such as alpha particles or fission fragments. Their diameters are approximately proportional to the bulk etch rate. Such a procedure is necessary to normalize data from a given detector to that of a standard reference.

IV. ENERGY WINDOW DETERMINATION AND OPTIMIZATION

A. Chapter Overview

This chapter will examine in greater detail, the various considerations involved in calculating the acceptance energy window. It will show that such factors as the track criteria, detector bulk etch rate, detector and tantalum foil thicknesses all enter into the determination of this window.

In particular, this chapter will first discuss in Section B, the methodology used in such calculations. In Section C a discussion will be given on the optimization of the knock-on window as a function of both detector and foil thickness. As will be shown, two optimal operating conditions exist depending on whether one wishes to maximize the triton or deuteron component.

In the last section, this window will be optimized by altering the 50/50 DT fuel ion density ratio in the target. As will be shown, this does not result in significant increases in the knock-on signal when compared with the typical 50/50 DT fuel ion density mixture.

No corrections are made in this chapter to correct for knock-on energy loss when traveling through the fuel and glass shell. These corrections will be discussed in Chapter VI.

B. Basic Theory

In general, not all knock-on particles can be separated from protons (i.e., they violate the track criteria). Either they are too low in energy (i.e., do not produce coincident tracks) or they are too high in energy (i.e., produce coincident tracks with track diameters less than D*) to be counted. As a result, only a finite energy window (which can be related to the fractional effective cross section) is allowed which produce tracks in accordance with the three knock-on criteria. Therefore, the number of knock-ons Q is given by

$$Q = \alpha \, (n_d \, \Gamma_d \, \sigma_d + n_t \, \Gamma_t \, \sigma_t) \, R \, Y_n \tag{4-1}$$

where Γ_d and Γ_t are the probability that a deuteron and triton fall respectively in their energy window. The parameter α in equation (1) is a geometry factor discussed below. Taking $\hat{\sigma}(\varepsilon)$ as the energy differential cross section for each knock-on process then

$$\Gamma_i = \frac{1}{\sigma_i} \int_{\substack{\text{Acceptance} \\ \text{Window}}} \sigma_i(\varepsilon) \, d\varepsilon \equiv \int \hat{\sigma}_i(\varepsilon) \, d\varepsilon \tag{4-2}$$

where $\hat{\sigma}(\varepsilon)$ is the normalized energy differential cross section.

Equation 1 can be rewritten as

$$Q = \alpha \, \sigma_{total} \, (n_d \, \omega^{(d)} + n_t \, \omega^{(t)}) \, R \, Y_n \tag{4-3}$$

$$\omega^{(d)} \equiv \frac{1}{\sigma_{total}} \int_{\substack{energy\ window \\ for\ deuterons}} \sigma_d\,(E)\,dE \qquad (4\text{-}4)$$

$$\omega^{(t)} \equiv \frac{1}{\sigma_{total}} \int_{\substack{energy\ window \\ for\ tritons}} \sigma_t\,(E)\,dE \qquad (4\text{-}5)$$

Defining ν as the n_d to n_t fuel ion density ratio and m_p as the proton mass, equation (2) can be solved for ρR giving

$$\rho R = \frac{m_p}{\alpha\ \sigma_{total}} (2\nu + 3)\left[\nu\,\omega^{(d)} + \omega^{(t)}\right]^{-1} \left(\frac{\Omega}{4\pi}\right)^{-1} \frac{Q}{Y_n} \qquad (4\text{-}6)$$

where Q is now the total number of knock-on particles intercepting a detector of fraction solid angle $\frac{\Omega}{4\pi}$.

The geometry factor α, is model dependent. This parameter has been calculated in Appendix F to be equal to 1 for an isotropic neutron point source located at the center of the fuel and equal to $\frac{3}{4}$ for a uniformly distributed isotropic neutron distribution in the fuel. Lilac simulations (see Apprendix G) show that in the present experiments the majority of neutrons are located in a small region near the center of the fuel. Therefore, in the calculations for ρR in that last chapter, α was set equal to 1.

The parameters $\omega^{(d)}$ and $\omega^{(t)}$ (or equivalently Γ_d and Γ_t) can only be determined if a detailed knowledge of the knock-on energy distribution is known.[16] These distributions have been measured and tabulated. Figures 4.1 and 4.2 show both the energy distribution as well as the cumulative distribution for each of the knock-on particles. The high energy cut-off as mentioned earlier, correspond to the forward-scattered peaks located at 10.6 and 12.5 MeV for tritons and deuterons respectively.

Using the cumulative distribution along with the energy limits for the acceptance window Γ_d and Γ_t can be directly found. For example, if the energy window limits, determined by the track criteria are 2 and 5 MeV for deuterons then Γ_d is equal to 0.28 .

C. Energy Window Optimization - System Parameters

Clearly from Figures 4.1 and 4.2 there are energy intervals where signal content is high. In qualitative terms the signal content is the area under each knock-on spectrum over the energy interval where the three knock-on criteria apply. This signal content (hereafter referred to as the effective cross section) can be expressed quantitatively as

$$\sigma_{eff} = (\Gamma_o\sigma_d + \Gamma_t\sigma_t) \qquad (4\text{-}7)$$

$$= (\omega^{(d)} + \omega^{(t)})$$

TRITON KNOCK-ON SPECTRUM AND ITS INTEGRAL REFERENCED FROM THE FORWARD SCATTERED PEAK

UR LLE

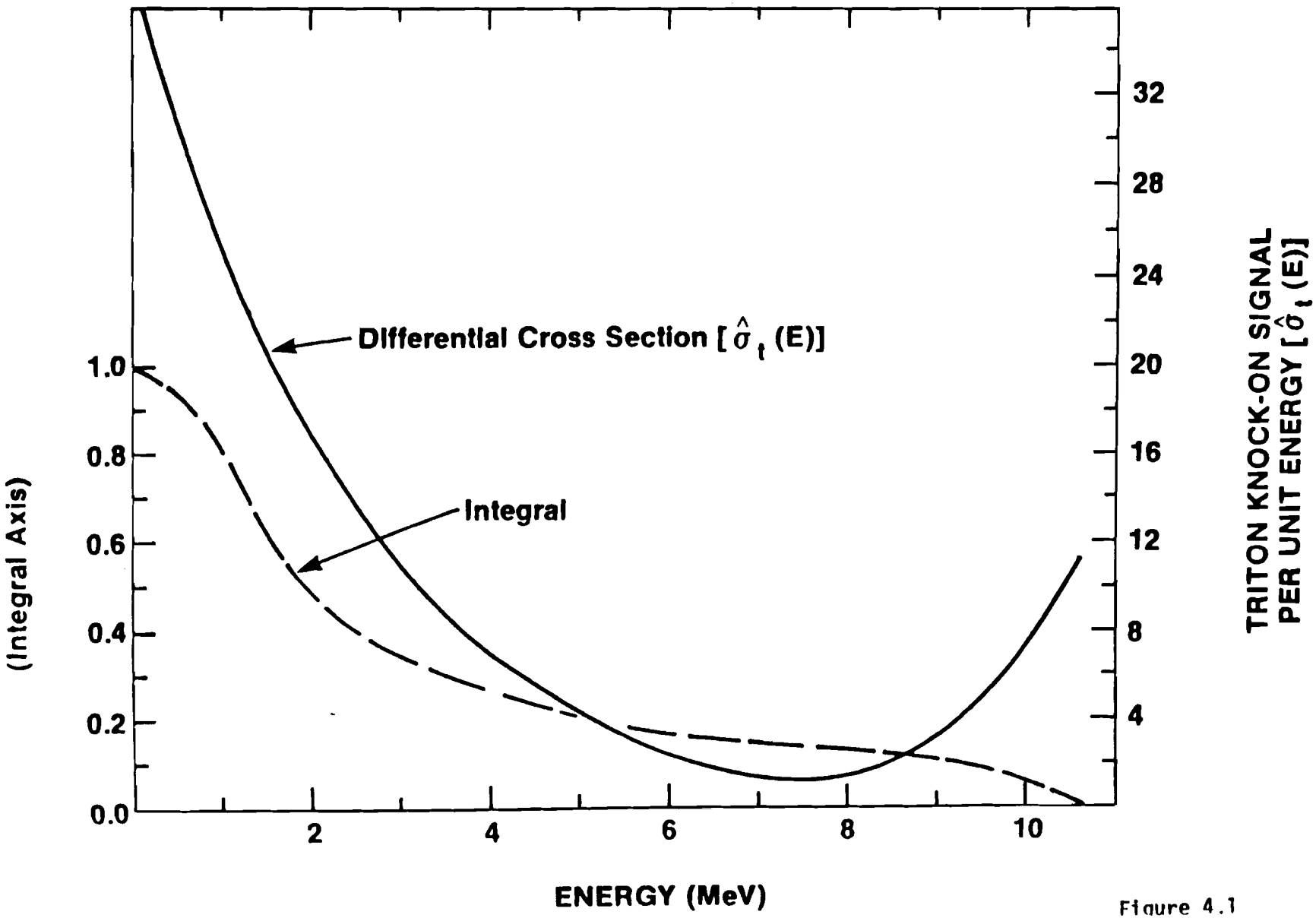

Figure 4.1

DEUTERON KNOCK-ON SPECTRUM AND ITS INTEGRAL REFERENCED FROM THE FORWARD SCATTERED PEAK

UR LLE

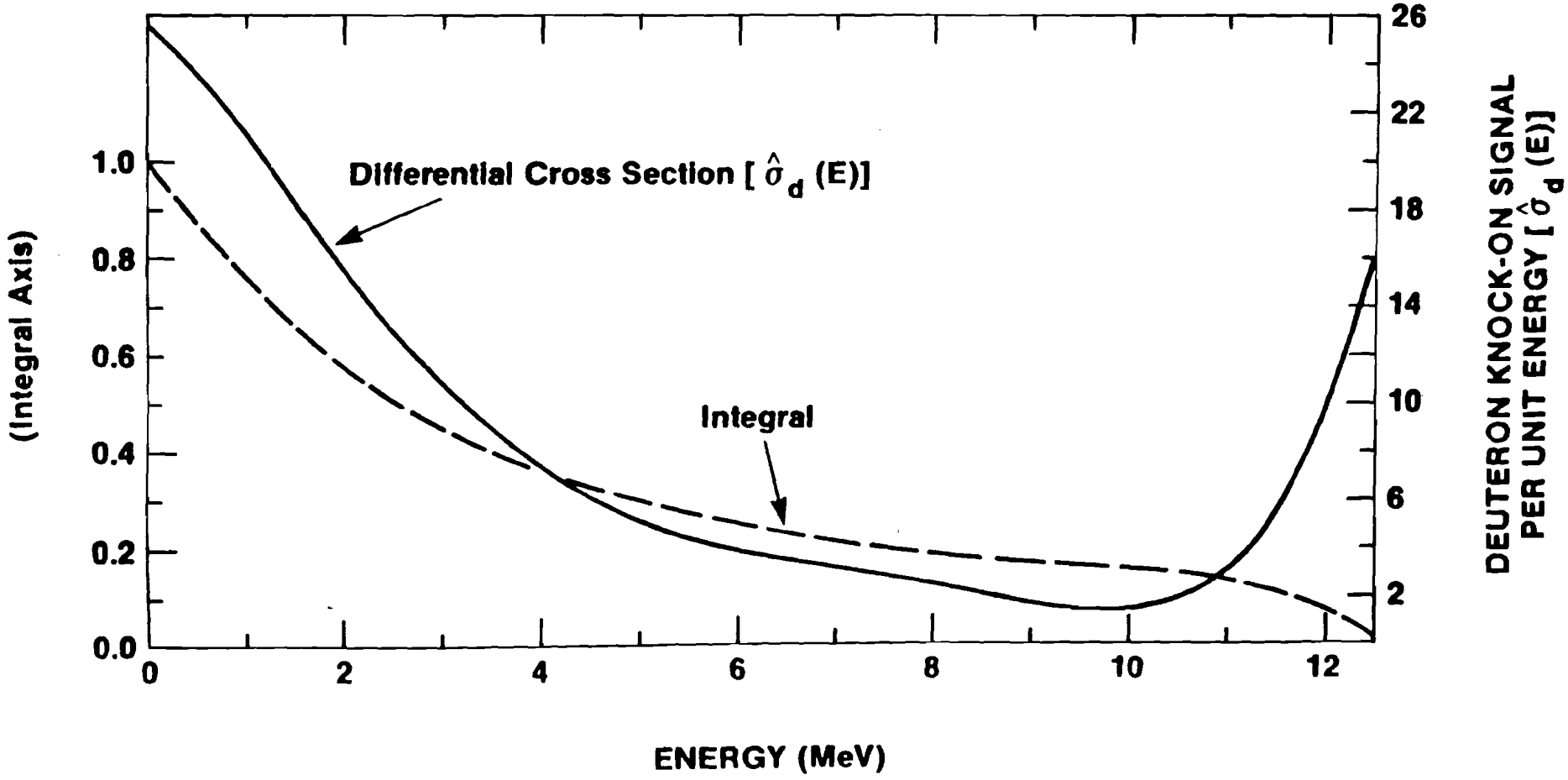

Figure 4.2

Therefore equation (6) takes the form

$$\rho R = 5.42\ \sigma_{eff}^{-1}\ \left(\frac{\Omega}{4\pi}\right)^{-1}\ \frac{Q}{Y_n} \qquad (4\text{-}8)$$

It is assumed that unless otherwise stated that the deuteron-to-triton ion density ratio is 1.

To determine Γ_d and Γ_t one requires particle energy-range data for protons, deuterons, and tritons in CR-39. Figures 4.3, 4.4 and 4.5 show the range for protons deuteron and tritons. From this data one can (1) find the energy (E*) for which a proton has a range equal to the effective detector thickness, and (2) the energies of the deuteron and triton (i.e., E_{Deut}^{Min} and E_{Trit}^{Min}) having ranges equal to the effective detector thickness. Therefore, the energy windows satisfying the track criteria are

Deuterons: $\quad E_{Deut}^{Min} < E_{Deut} < 2\ E^*$

Tritons: $\quad E_{Trit}^{Min} < E_{Trit} < 3\ E^*$

These energy intervals represent the reduced energies of deuterons and tritons after they have traversed a given tantalum foil thickness. It is therefore necessary to know the particle energy-range data in tantalum as well. Figures 4.6 and 4.7 plots this information for tritons and deuterons respectively.[17] For example, if the initial deuteron energy is 7.5 MeV and it traverses 40 μm of tantalum

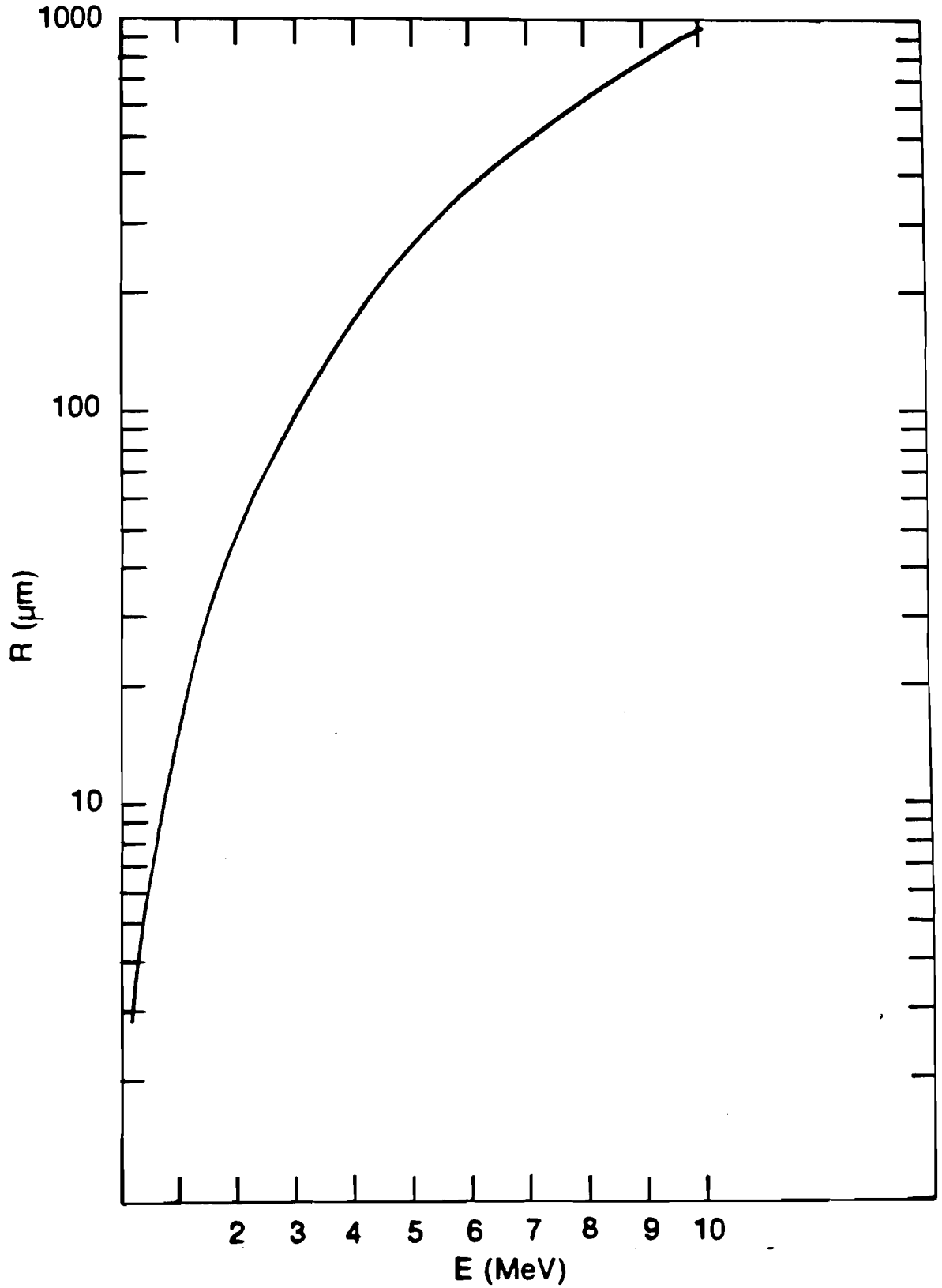

Figure 4.3

Deuteron Range in CR-39

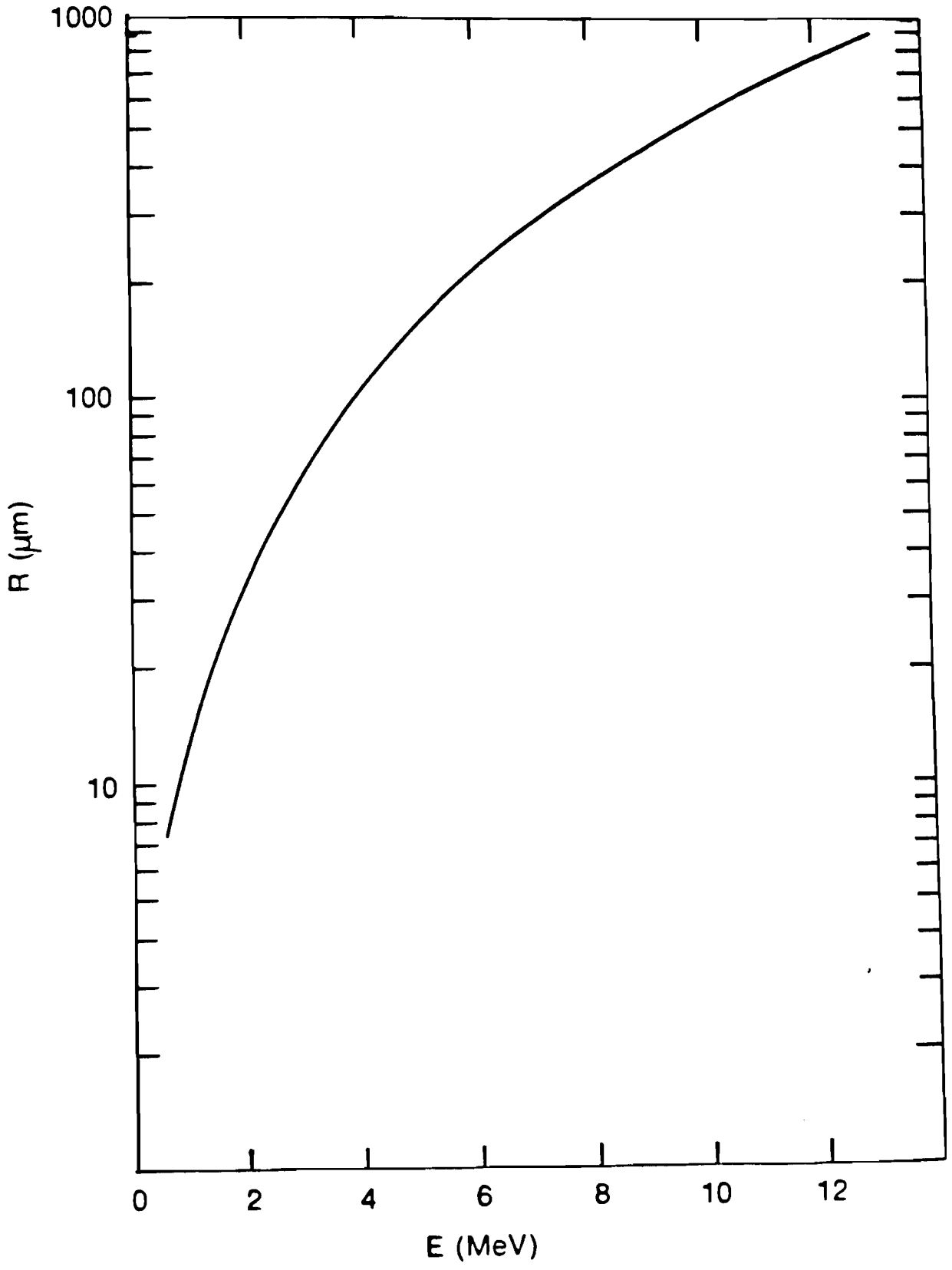

Figure 4.4

Triton Range in CR-39

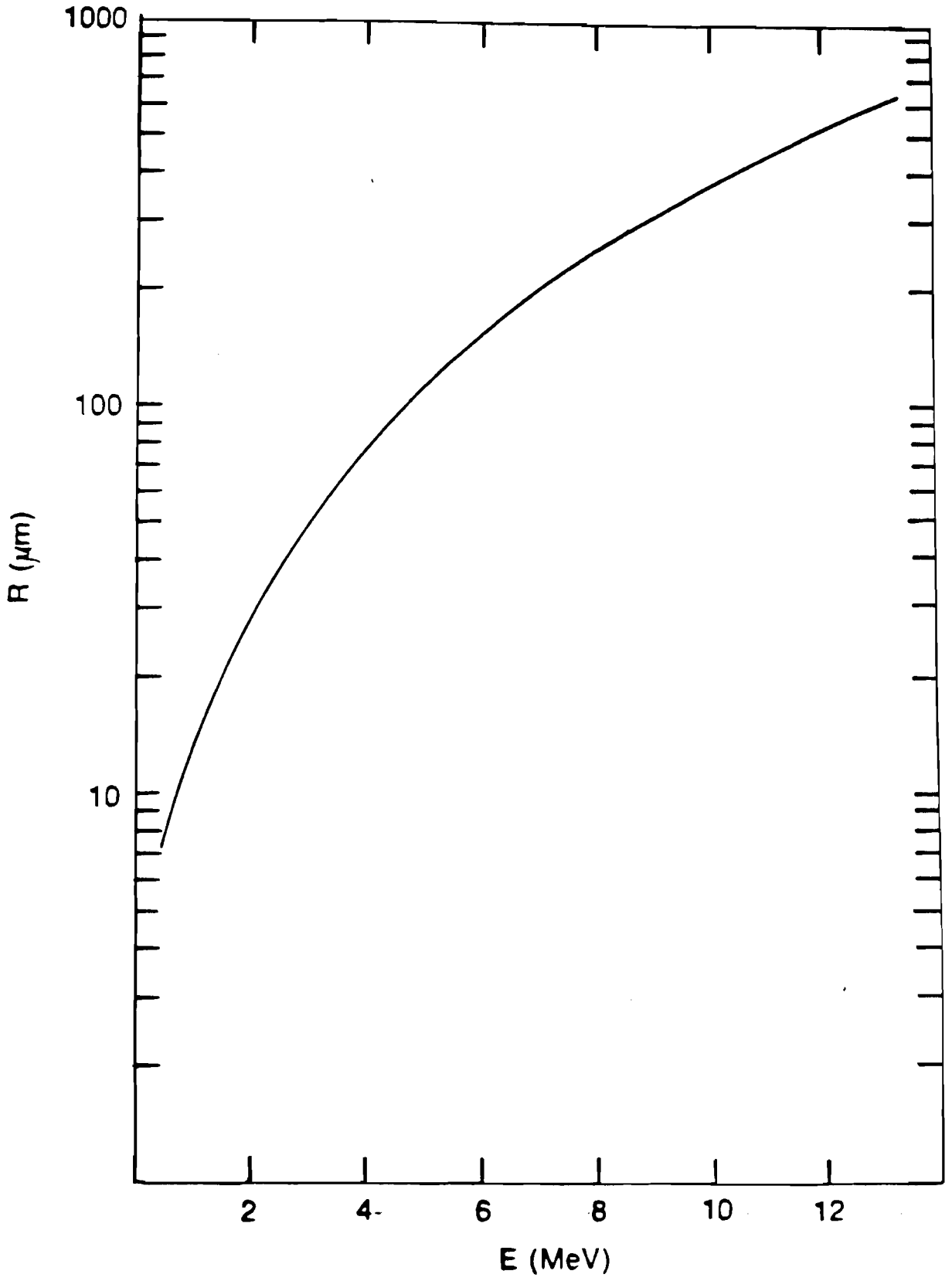

Figure 4.5

TRITON ENERGY LOSS AS A FUNCTION OF Ta FOIL THICKNESS

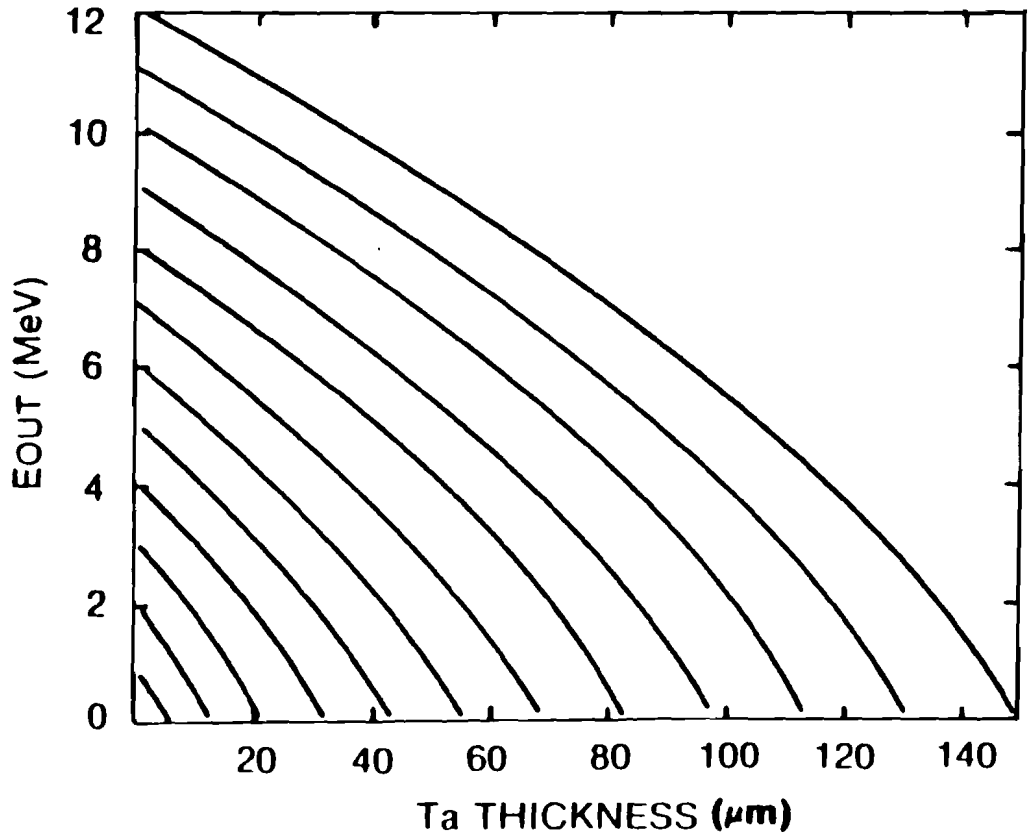

Figure 4.6

DEUTERON ENERGY LOSS AS A FUNCTION OF Ta FOIL THICKNESS

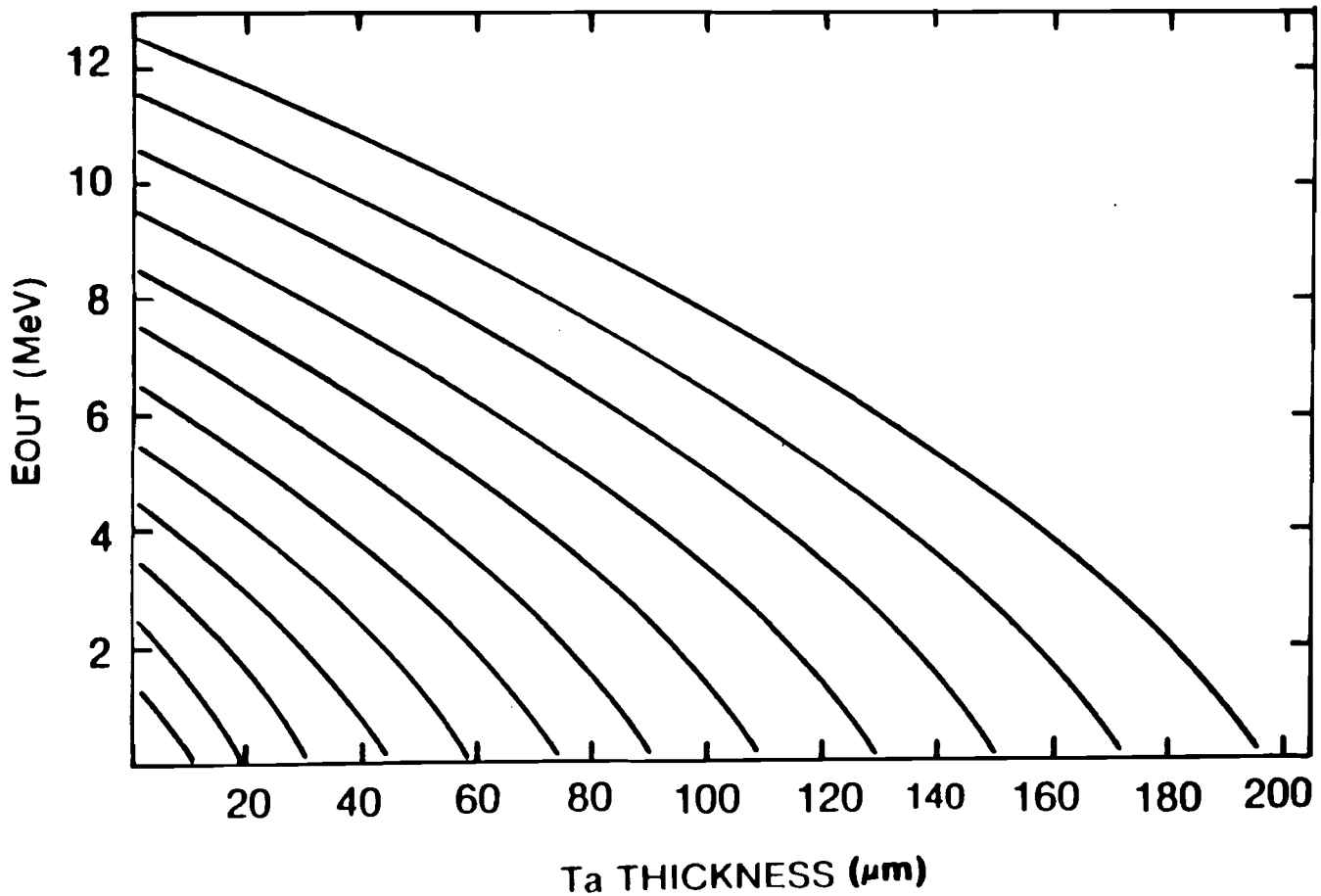

Figure 4.7

its mean exit energy is 5.0 MeV. Therefore, CR-39 and tantalum foil thickness each have a unique and important role to play in system optimization. CR-39 thickness along with the track criteria determines the extent of the energy window. The tantalum foil thickness determines which portion of the knock-on distribution is positioned within the energy window.

Defining $\hat{E}^{Min}_{Deut}$ and $\hat{E}^{Min}_{Trit}$ as the energies required for deuterons and tritons to slow down to energies E^{Min}_{Deut} and E^{Min}_{Trit} after traversing the foil thickness, one then can diagramatically summarize the methodology used to calculate the energy windows and signal as

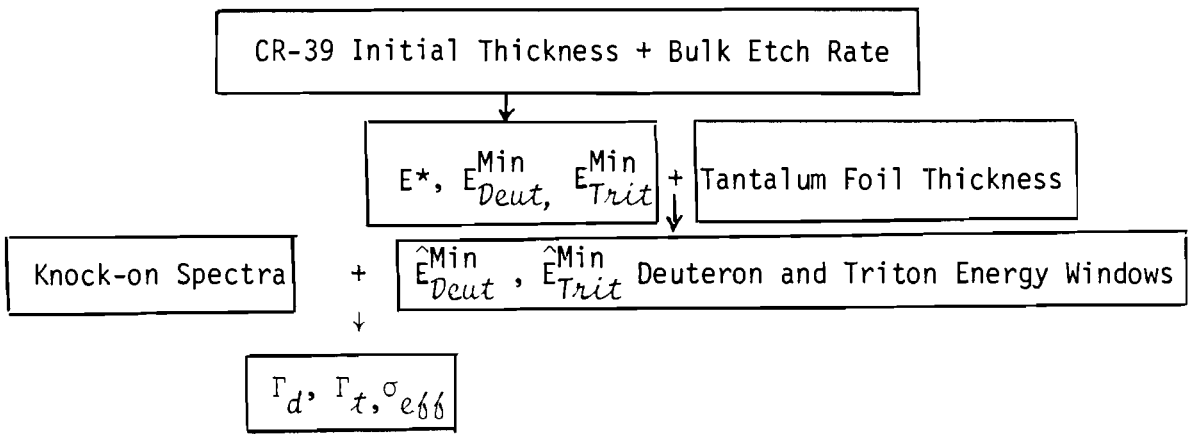

Using this methodology, Figures 8 and 9 have been generated for various CR-39 effective thicknesses and tantalum foil thicknesses. The dominant peak which is especially clear for the 20 and 40 μm foils (i.e., the left-hand peak) is due to the shifting of the triton forward scattered peak by the foil into the energy window defined by the CR-39 effective thickness. As the foil thickness increases, thinner CR-39 detectors are required to keep the triton peak

within the energy window. The second peak (i.e., the right-hand peak) is the forward-scattered deuteron peak and exhibits similar behavior to the triton peak.

To optimize system performance it is useful to replot Figures 4.8 and 4.9 so that the CR-39 effective thickness and tantalum foil thickness form the axes of a contour plot of the knock-on signal (see figure 4.10). Two operating constrains limit the choice of tantalum foil and CR-39 thickness. First, the tantalum foil can not be thinner than the 40 μm which is required to stop all DD-protons from striking the track detector. Second, the CR-39 effective thickness must not be greater than 150 μm because thicker detectors will result in D* values less than 10 μm, making identification extremely tedious especially in the presence of the intrinsic pit background. Therefore, the optimal system configurations (i.e., one for mainly a triton signal component while the other strictly a deuteron signal component) are

(1) 40 μm tantalum and 100 μm effective CR-39 thickness

(2) 110 μm tantalum and 150 μm effective CR-39 thickness

D. Energy Window Optimization - Fuel Ion Ratio

Equal mixtures of deuterium and tritium are not always the optimal means of maximizing the knock-on signals.

KNOCK-ON SIGNAL VARIATION AS A FUNCTION OF DETECTOR THICKNESS

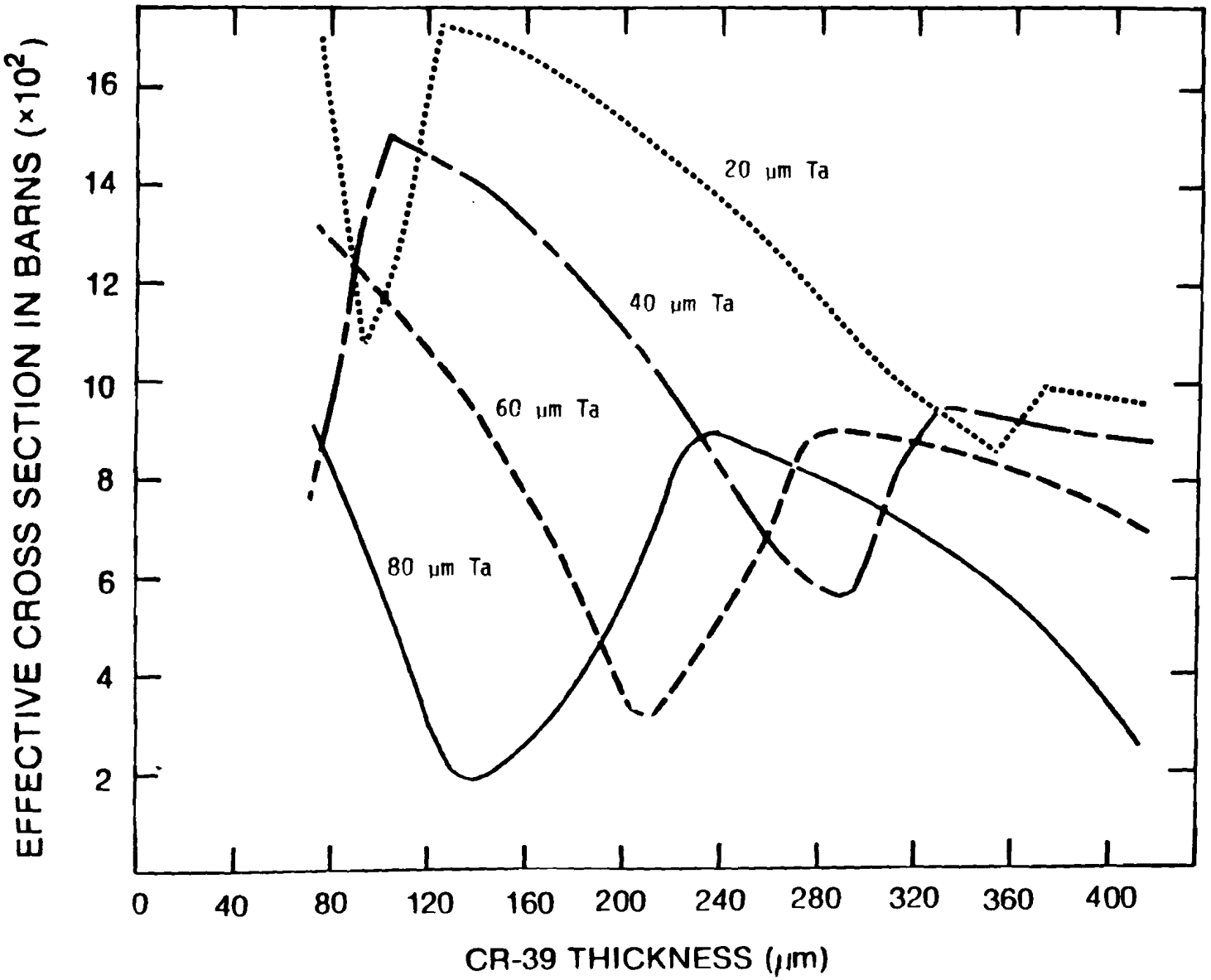

Figure 4.8

KNOCK-ON SIGNAL VARIATION AS A FUNCTION OF DETECTOR THICKNESS

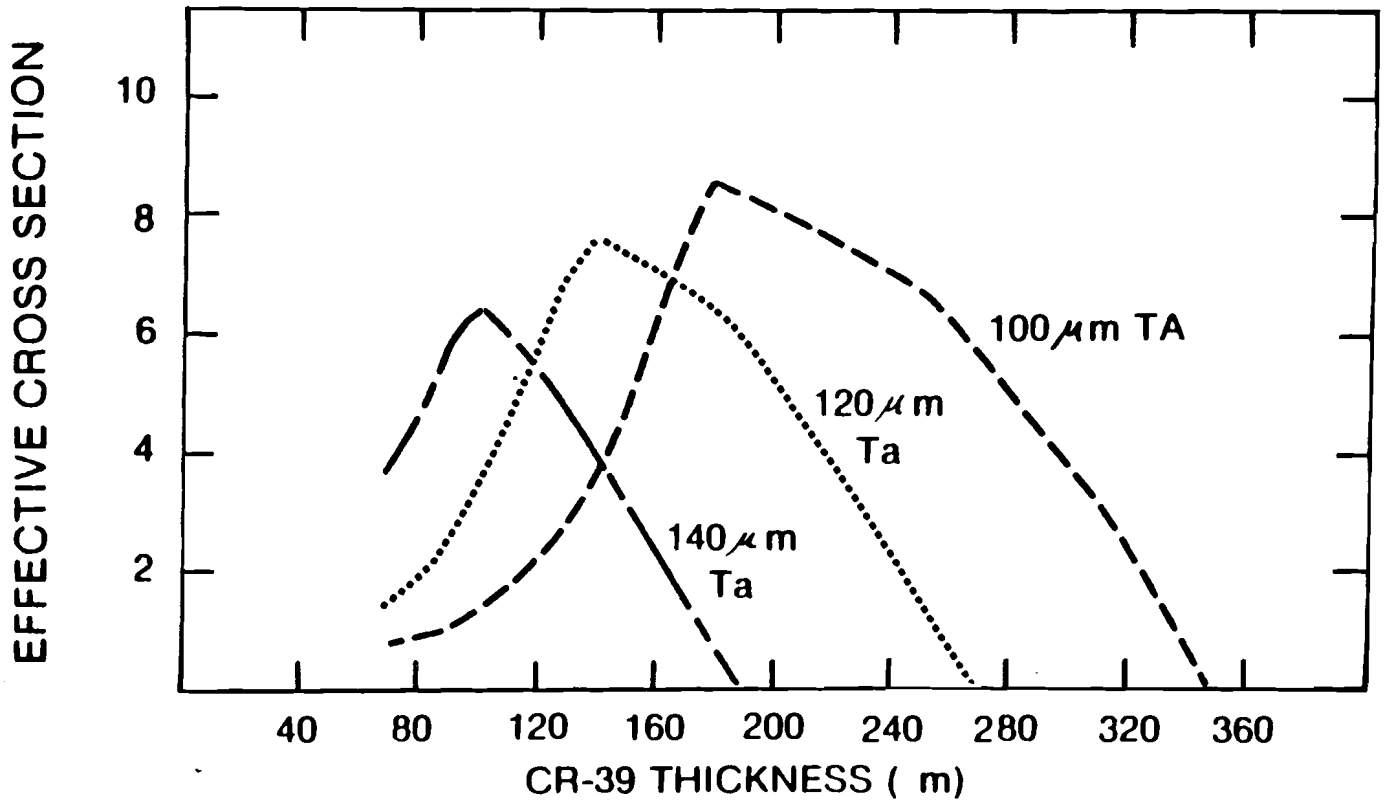

Figure 4.9

SYSTEM OPTIMIZATION STUDY

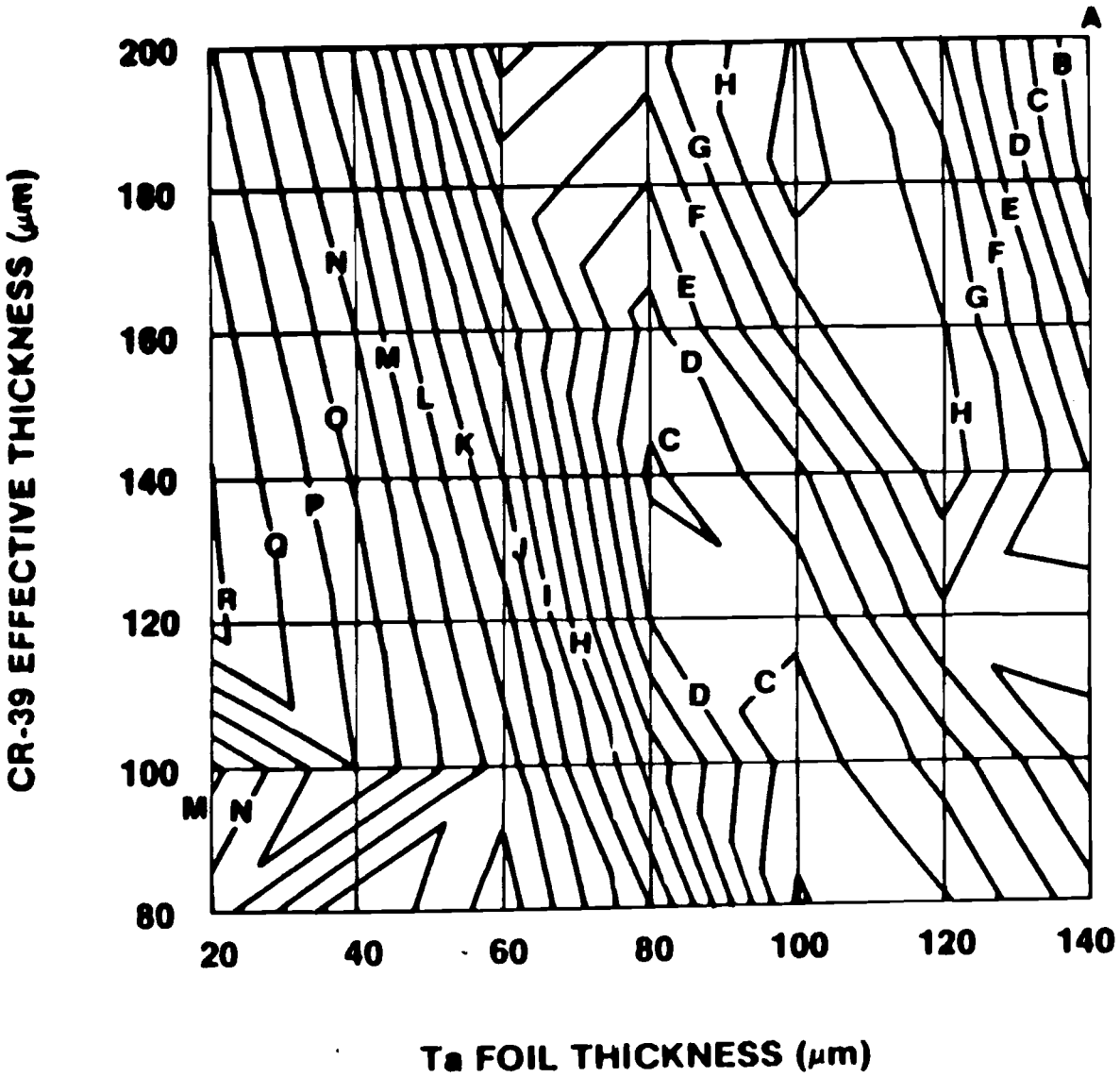

Identification	Contour Value
A	0.
B	1.
C	2.
D	3.
E	4.
F	5.
G	6.
H	7.
I	8.
J	9.
K	10.
L	11.
M	12.
N	13.
O	14.
P	15.
Q	16.
R	17.
S	18.
T	19.

Figure 4.10

E1823

Noting that the thermonuclear yield scales as $\nu\ (1+\nu)^{-2}$ (i.e., $n_d \cdot n_t$) and holding the fuel ion density constant (n_o) then

$$Q = C_1\ Y_n \left[n_d \Gamma_d \sigma_d + n_t \Gamma_t \sigma_t \right] \tag{4-9}$$

$$= C_1\ n_o^2\ \frac{\nu}{(1+\nu)^2} \left[\nu \frac{n_o}{1+\nu}\ \Gamma_d \sigma_d + \frac{n_o}{1+\nu}\ \Gamma_t \sigma_t \right] \tag{4-10}$$

$$= C \left[\frac{\nu}{(1+\nu)^2} \right] \left[\frac{\nu + \gamma}{1+\nu} \right] \equiv Q_\gamma \tag{4-11}$$

where C_1 and C are constants and γ is defined as the $\Gamma_t \sigma_t$ to $\Gamma_d \sigma_d$ ratio. The expression in the left bracket is the neutron yield (Y) scaling with ν. The expression in the right bracket is the signal contribution per neutron arising from the deuteron and triton windows. (f_γ). Figure 4.11 plots Y, f_γ and Q_γ for various γ values. As seen, the yield has a maximum for equal fuel ion concentrations. However, f_γ has no clear maximum. If $\gamma<1$ then f asymptotically approaches 1 from below as ν increases. Similarly if $\gamma>1$ then f asymptotically approaches 1 from above as ν increases. The product of Y and $f\gamma$ gives the knock-on signal and exhibits a distinct maximum. If tritons contribute predominantly to the knock-on signal (i.e., $\gamma>1$) then the optimal fuel concentration will favor a fuel ion ratio with less than 1

OPTIMIZATION CURVES FOR DEUTERIUM-TRITIUM FUEL CONCENTRATION

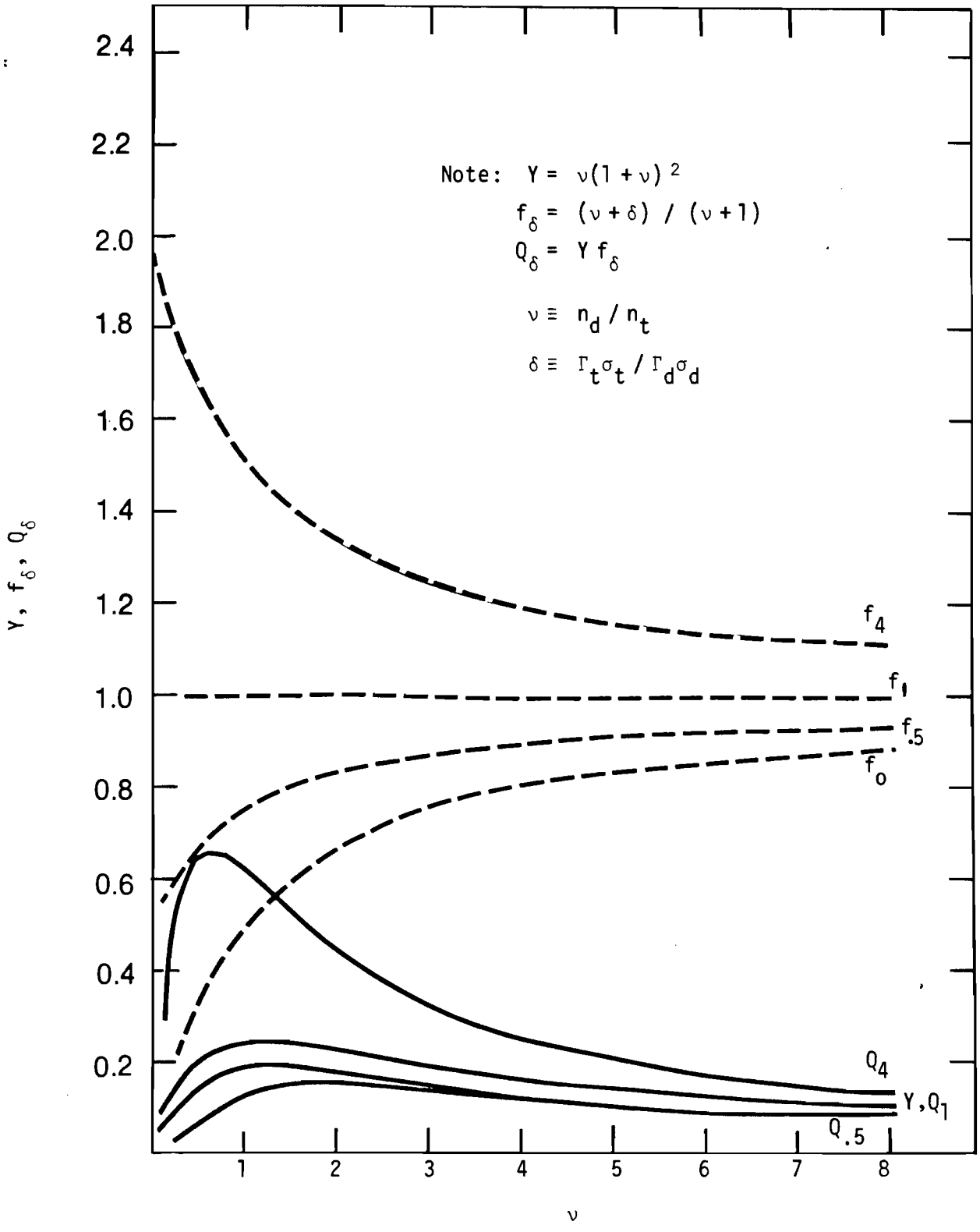

Figure 4.11

(i.e., $n_t > n_d$). Likewise, if $\gamma<1$ then the fuel ion ratio must be greater than 1. Figure 4.8 shows the optimal fuel concentrations for various γ values as indicated by the arrows.

The optimal value for ν can be determined by taking the derivative of equation (11) and setting it equal to zero. The result of this procedure leads to

$$\nu_{optimal} = (1-\gamma) + \sqrt{(1-\gamma)^2 + \gamma} \qquad (4\text{-}12)$$

This expression is plotted in Figure 4.12. As expected $\nu_{optimal}$ decreases as γ increases. Notice for large γ, ν_{opt} varies very little.

Figure 4.13 shows the optimal fuel ion ratio as a function of Ta foil thickness. The CR-39 effective thickness has been taken to be 100 μm, thereby maximizing the knock-on signal using a 40 μm Ta foil. Notice that the optimal ratio is nearly constant for foil thickness between 40 and 75 μm (i.e., referred to as "thin foils") and thicknesses greater than 90 μm (i.e., referred to as "thick foils"). This is due to the fact that for thin foils, the predominant signal contribution is from tritons (i.e., γ large), resulting in only a small variation in ν_{opt}. For thick foils only deuterons contribute to the knock-on signal (i.e., $\gamma = 0$) resulting in γ_{opt} being exactly equal to 2. From Figure 4.13 it is seen that if standard targets are used (i.e., $\nu = 1$) then the system performance is only reduced by 5% for thin foils and 15% for thick foils.

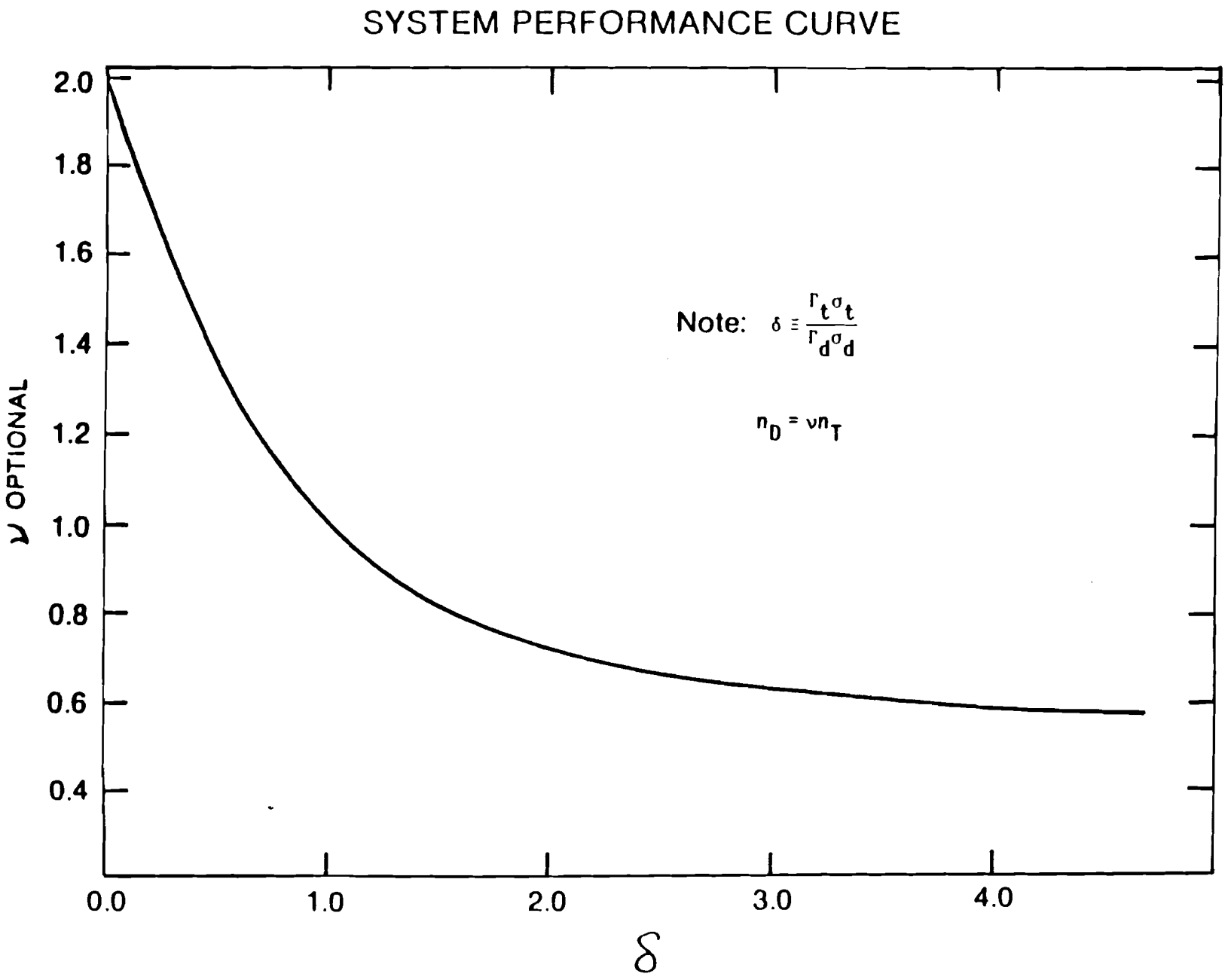
SYSTEM PERFORMANCE CURVE
2.0
1.8
1.6
1.4
1.2
1.0
0.8
0.6
0.4
ν OPTIMAL
Note: $\delta \equiv \frac{\Gamma_t \sigma_t}{\Gamma_d \sigma_d}$
$n_D = \nu n_T$
0.0
1.0
2.0
3.0
4.0
δ

Figure 4.12

OPTIMAL FUEL ION RATIO TO MAXIMIZE KNOCK-ON SIGNAL

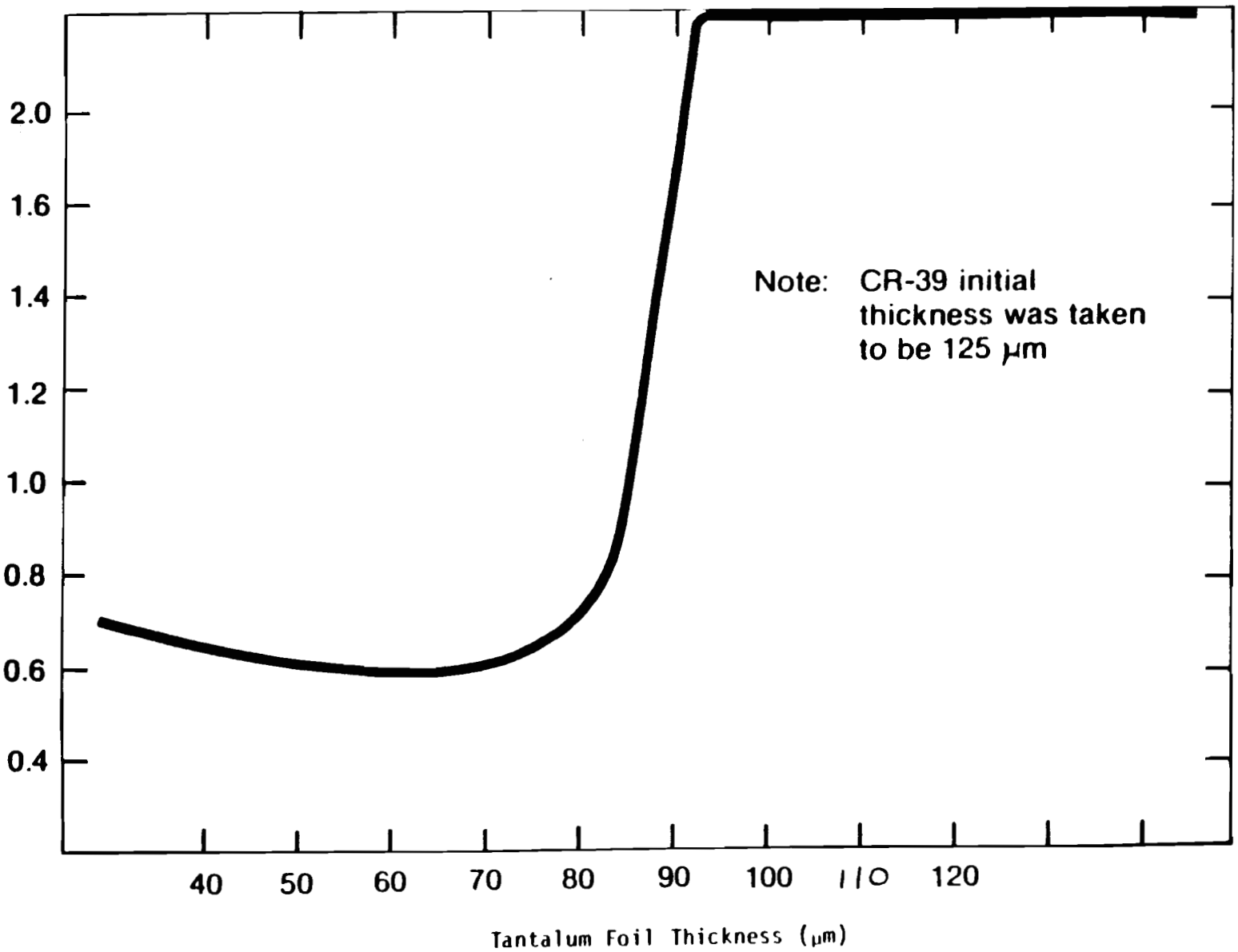

Figure 4.13

V. FUEL ρR MEASUREMENTS - EXPERIMENTAL DATA

A. Chapter Overview

This chapter will examine data obtained from the OMEGA 24-beam laser facility at the University of Rochester's Laboratory for Laser Energetics. It will be divided into four sections.

The first section will describe the experimental conditions associated with the measurements. Specifically, details of laser and detector conditions will be discussed.

The second section will demonstrate the use of the methodology developed in the last chapter. Here, a specific shot will be examined in detail, showing the reader all the essential elements needed to deduce the parameter D*. This will be done by both examining the raw data as well as from range calculations in CR-39.

In section D the above example case is continued and the fuel ρR calculation is presented. Issues such as the calculation of the effective cross section and the propagation of errors will be addressed.

This chapter will conclude with a general discussion of results obtained under short and long pulse laser conditions. It will show that enhanced compression can be achieved in the long pulse experiments with characteristic fuel ρR values in the low 10^{-3} g/cm^2 regime.

B. Experimental Conditions

The knock-on ρR experiments were performed using the 24-beam Nd: glass laser (OMEGA) at the University of Rochester. Two examples of experiments diagnosed by the knock-on method are summarized in Table 5.1. Particular attention will be given to shot number 7036 in sections C and D illustrating the application of the methodology developed in previous chapters.

In both the high and low compression experiments, targets had a 1 μm glass wall thicknesses encapsulating a 20 atmosphere equimolar DT fuel mixture. The low compression experiments had characteristic laser pulse widths of 90 psec producing peak intensities of $\sim 2 \times 10^{16}$ W/cm^2 on target. The high compression experiments had characteristic pulse widths of nearly 1 nsec and peak intensities of $\sim 4 \times 10^{14}$ W/cm^2.

The knock-on particles were recorded with 150 ± 5 μm thick detectors. Each measurement consisted of two detectors which were mounted 90^o apart from each other. The two detectors were implemented to increase the available collecting solid angle. Each detector was cut to a 3/4 inch diameter disc and placed inside an air-encapsulated chamber. One of the walls of this chamber consisted of a 50 μm tantalum foil as shown in Figure 5.1.

An extraction system was developed to retract the track detector assembly after a single shot in later high-compression experiments. This system was not available for the earlier low compression experiments where fuel ρR measurements were averaged over

Table 5.1

Experimental Conditions and Results

	High Compression	Low Compression
SHOT NUMBER	7038	6037/6038
LASER:		
Energy (J)	1982	693/778
Pulse Width (ps)	921	89/92
Intensity	4×10^{14}	$2\times10^{16}/2\times10^{16}$
TARGET (SiO_2 shell):		
Thickness (μm)	0.91	1.01/1.11
Radius (μm)	209	103/99
Fill Pressure (atm)	20	16/20
YIELDS:		
Neutrons (Y)	5.5×10^{8}	$1\times10^{10}/1\times10^{10}$
Knock-on Tracks (Q*)	91	49
Total Number of Knock-ons (Q)	9.4×10^{4} †	5.0×10^{5}
INFERRED ρR (g/cm^2)	1.2×10^{-3}	$\langle 1.3\times10^{-4} \rangle$ ††

† Using a solid angle of 0.92% of 4π and a detection efficiency of 8.2% of the total knock-on spectrum.

†† This is the average fuel ρR for the two low compression shots.

The Knock-on Diagnostic

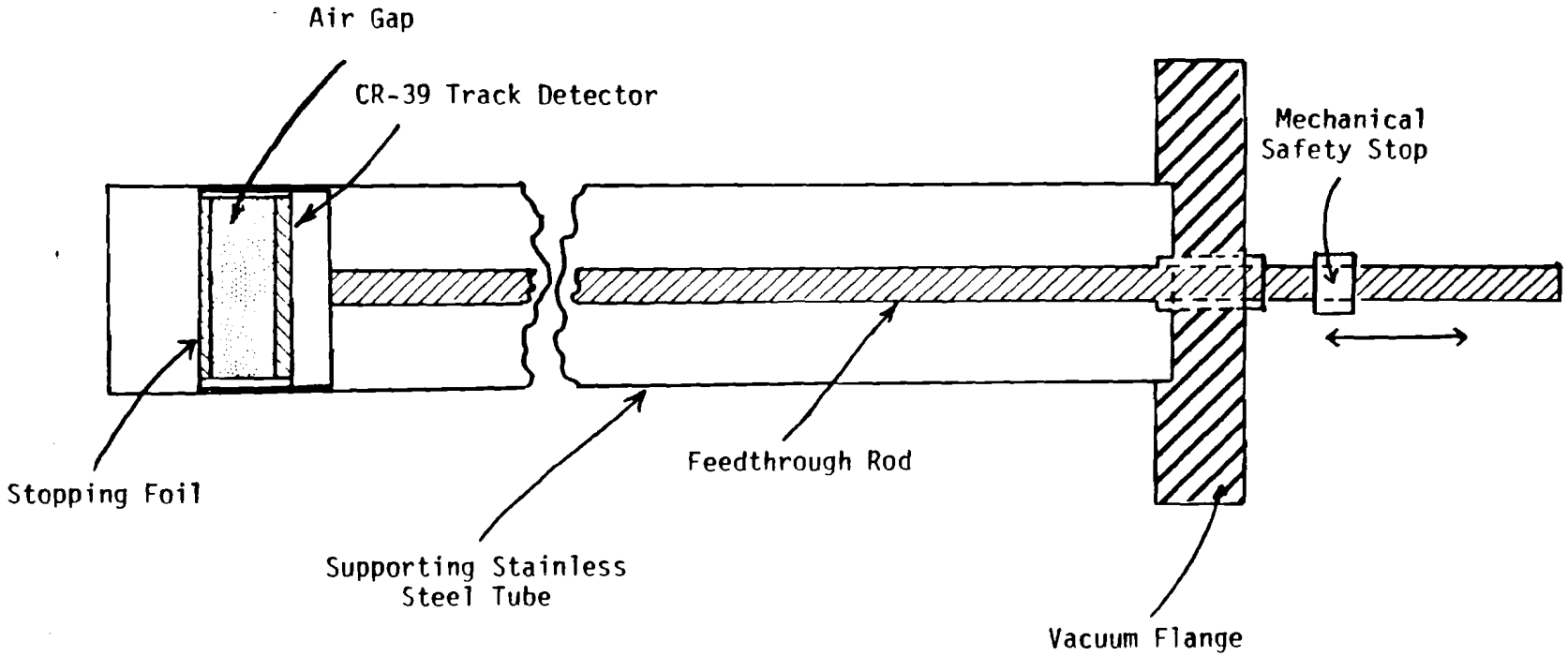

Figure 5.1

multiple shots. This extraction system consisted of a vacuum feedthrough assembly manually controlling the positioning of the track detector assembly in the OMEGA vacuum system as shown in Figure 5.1. The detector assembly rode inside a supporting stainless steel tube to insure that (1) the feedthrough rod did not strain the feedthrough o-ring assembly and (2) the feedthrough rod did not bend and obstruct any of the laser beams from reaching the target. A mechanical stop was positioned on the feedthrough rod to restrict the detector assembly from moving closer than 7 cm from the target. At this distance, the fractional collecting solid angle ($\Omega/4\pi$) was 5×10^{-3}.

In both the high and low compression experiments, each detector was post-exposed before etching to a Cf^{252} fission source for later thickness corrections.

Accompanying each shot was a measurement of the neutron yield. The primary diagnostic used was a copper activation system which was calibrated using solid state track detectors.[13] A silver activation system was implemented when neutron yields fell below the copper activation threshold of 10^8.

C. The Determination of D* Based on Experimental Data - Sample Calculations

The following analysis is based on the data obtained from shot number 7038 as already characterized in Table I. The calculations presented here are intended to illustrate to the reader how the

methodology described previously is actually implemented. This analysis is carried into the next section where the fuel ρR is determined. The goal of this section is to demonstrate how D* can be estimated from both the raw data of the track diameter histogram as well as from range calculations in CR-39.

Measurement of D* from the track diameter histogram requires first the systematic scanning and recording of all coincident and non-coincident tracks. Each track is photographed under 1000x and if required a double exposure is taken for all coincident tracks. Figure 5.2a and b shows typical examples of non-coincident tracks. The slight ellipticity of the track diameters are the result of the charged particles entering the detector at a slight angle from normal incidence.

Figures 5.2c, d, e, and f are examples of spatial coincident tracks. These pictures are double exposure of the track detector. One picture was taken of the top surface while the other exposure was taken of the bottom surface (note that CR-39 is clear). It should be noticed that in Figures 5.2c and d the bottom track diameters are smaller than the top diameter. These tracks as described in Chapter 3 may result from either knock-on particles or backscattered protons.

Each track diameter is measured and plotted in histogram form as illustrated in Figure 5.3. The shaded region represents the coincident tracks while the region above the shaded region represents the non-coincident tracks. Therefore, the total height of each bin count represents the total number of tracks whose top surface diameter falls within the given diameter interval.

(a)

(b)

(c)

(d)

(e)

(f)

Figure 5.2

The key to the direct estimation of D* is found in the non-coincident portion of the histogram. This portion is replotted in Figure 5.4. Notice that an abrupt transition occurs in the number of tracks between 12 and 13 μm and between 13 and 14 μm. This supports range calculation in CR-39 that protons with diameters less than 12.4 μm are too energetic to produce non-coincident tracks. Therefore based on non-coincident tracks from this histogram the value of D* must be less than 13 μm.

As suggested range calculations are consistent with this value extracted from the histogram. This can be shown by first determining the effective thickness of the track detector and then applying Figure 3.5 and shown again for convenience in Figure 5.5.

The effective thickness can be determined by measuring the fission track diameters which are introduced after the post-exposure to the knock-on particles. In the present situation the fission track diameters are measured to be 48 ± 1 μm. Therefore, the effective thickness using equations 3-4 is given by

$$R_{eff} = X_o - \frac{1}{4} D_f$$

$$= (150 \pm 5) - \frac{1}{4} (48 \pm 1)$$

$$\simeq 138 \pm 5 \text{ μm}$$

Using this value as the range of the proton required to produce a coincident track along with Figure 5.5 one finds that D* is equal to

KNOCK-ON DIAMETER SPECTRUM

UR LLE

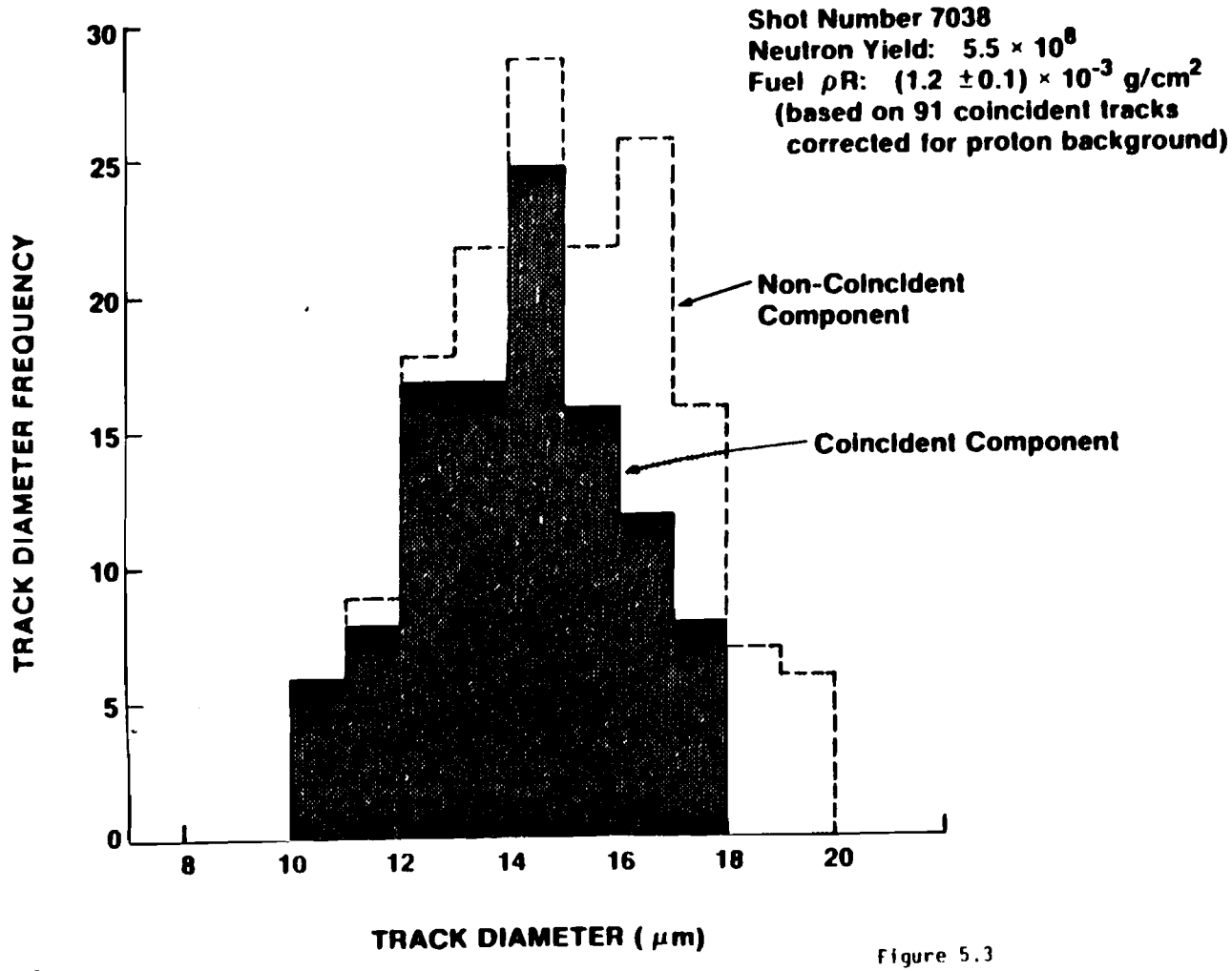

Figure 5.3

E1820

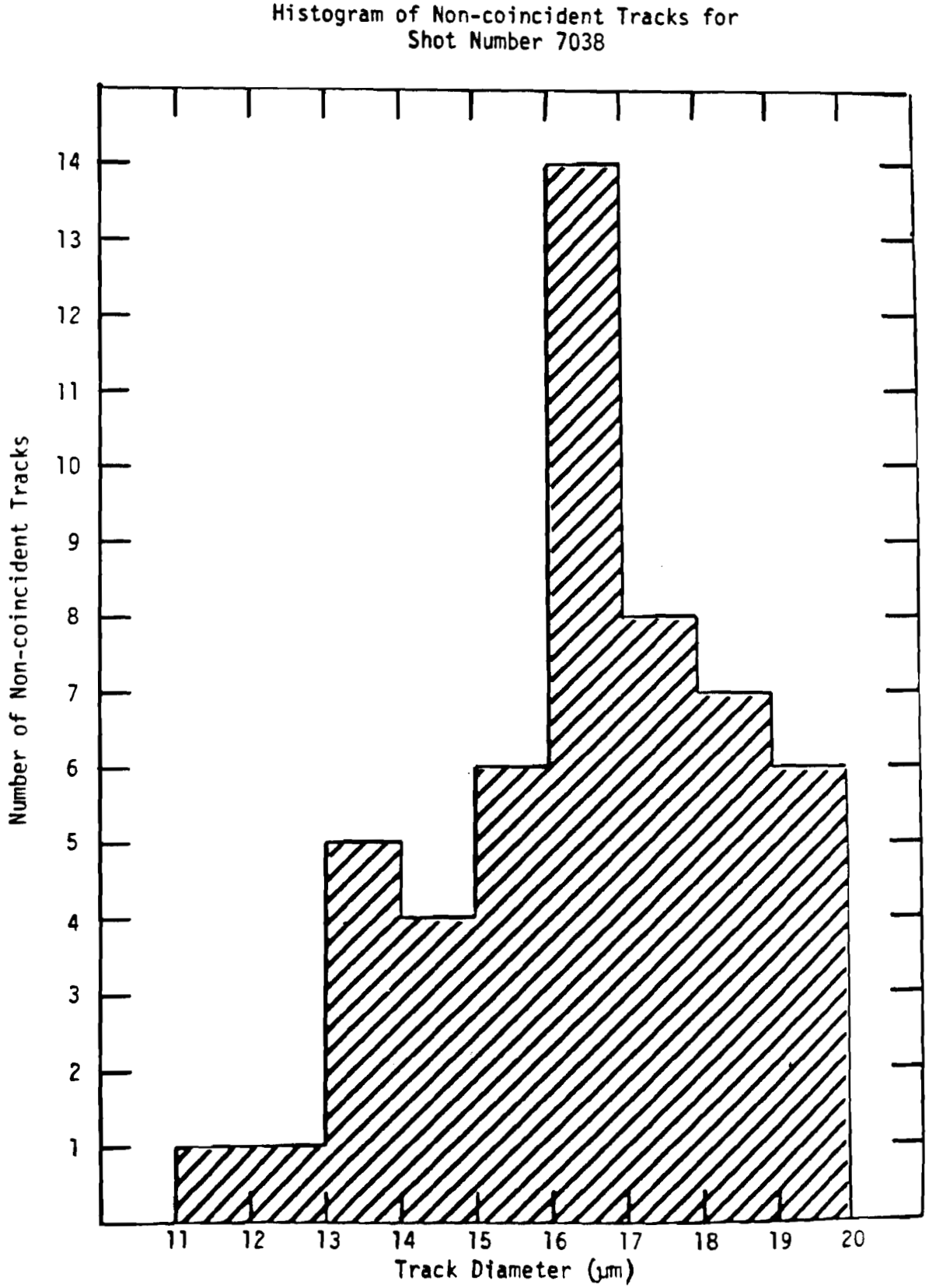
Histogram of Non-coincident Tracks for
Shot Number 7038
Number of Non-coincident Tracks
1
2
3
4
5
6
7
8
9
10
11
12
13
14
11
12
13
14
15
16
17
18
19
20
Track Diameter (μm)

Figure 5.4

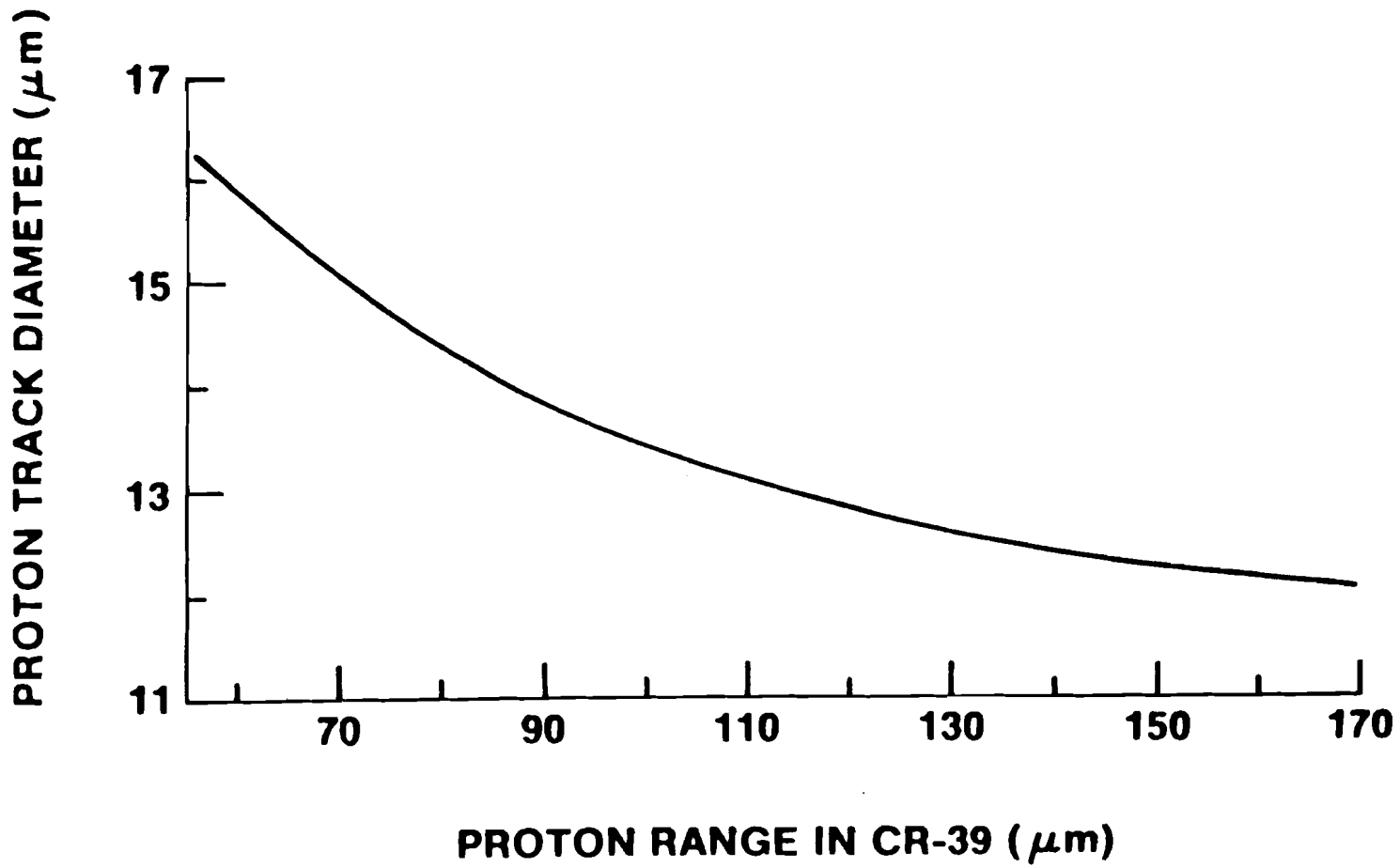
PROTON TRACK DIAMETER (μm)
17
15
13
11
70
90
110
130
150
170
PROTON RANGE IN CR-39 (μm)
E1647

Figure 5.5

12.4 ± .2 μm. This is in good agreement with the non-coincident transition esitmate for D* from Figure 5.4.

Knowing D* one can formulate the acceptance criteria necessary to separate the proton tracks from the knock-on tracks. Specifically, these criteria are

(1) The acceptance of all spatial coincident tracks with top surface diameters greater than 12.4 μm.

(2) The rejection of all spatial coincident tracks with bottom surface diameters less than 12.4 μm.

The criteria will enable one to obtain a measurement of the total number of knock-ons which is necessary in the determination of ρR.

D. The Calculation of Fuel ρR - Sample Calculations

Before the fuel ρR can be calculated, the effective cross section must be determined. As explained in Chapter IV, this is performed in two steps namely by (1) determining the energy interval of which deuterons and tritons can be separated from protons when incident on the detector and by (2) propagating each interval back through the stopping foil and establishing the portion of the knock-on spectra where particle separation is possible.

In calculating the energy interval in step (1), range information for each isotope in CR-39 along with the knowledge of the detector's effective thickness is required. The lower limit is determined by the least energetic proton required to traverse this thickness. By knowing this proton energy, the upper energy limit

determined by multiplying the proton energy by the knock-on specie nucleon number (i.e., the upper limit is established by D* which is a function only of charge and velocity). Figure 5.6 shows that deuterons and tritons can be separated from protons over the energies intervals of (4.6, 6.9) and (5.4, 10.3) MeV respectively. The arrows indicate the minimum energy required to traverse the detector and produce coincident tracks.

An uncertainty in the energy limits is introduced primarily from the uncertainty in the detector's effective thickness. Specifically, the lower energy limits are directly influenced by the uncertainty in the effective thickness. This is shown in the shaded region around each arrow in Figure 5.6. The upper limit is indirectly influenced by the uncertainty in determining the minimum proton energy required to produce a coincident track. Table 5.2 summarizes the energy intervals and corresponding limit uncertainties for each knock-on specie in columns two and three.

Table 5.2

Knock-On Energy Window Limits

	After Passage Through Ta Foil		Before Passage Through Ta Foil	
Specie	Lower Energy Limit (MeV)	Upper Energy Limit (MeV)	Lower Energy Limit (MeV)	Upper Energy Limit (MeV)
Deuteron	4.6 ± .1	6.9 ± .2	7.7 ± .1	9.6 ± .1
Triton	5.4 ± .1	10.3 ± .2	8.8 ± .1	12.1 ± .1

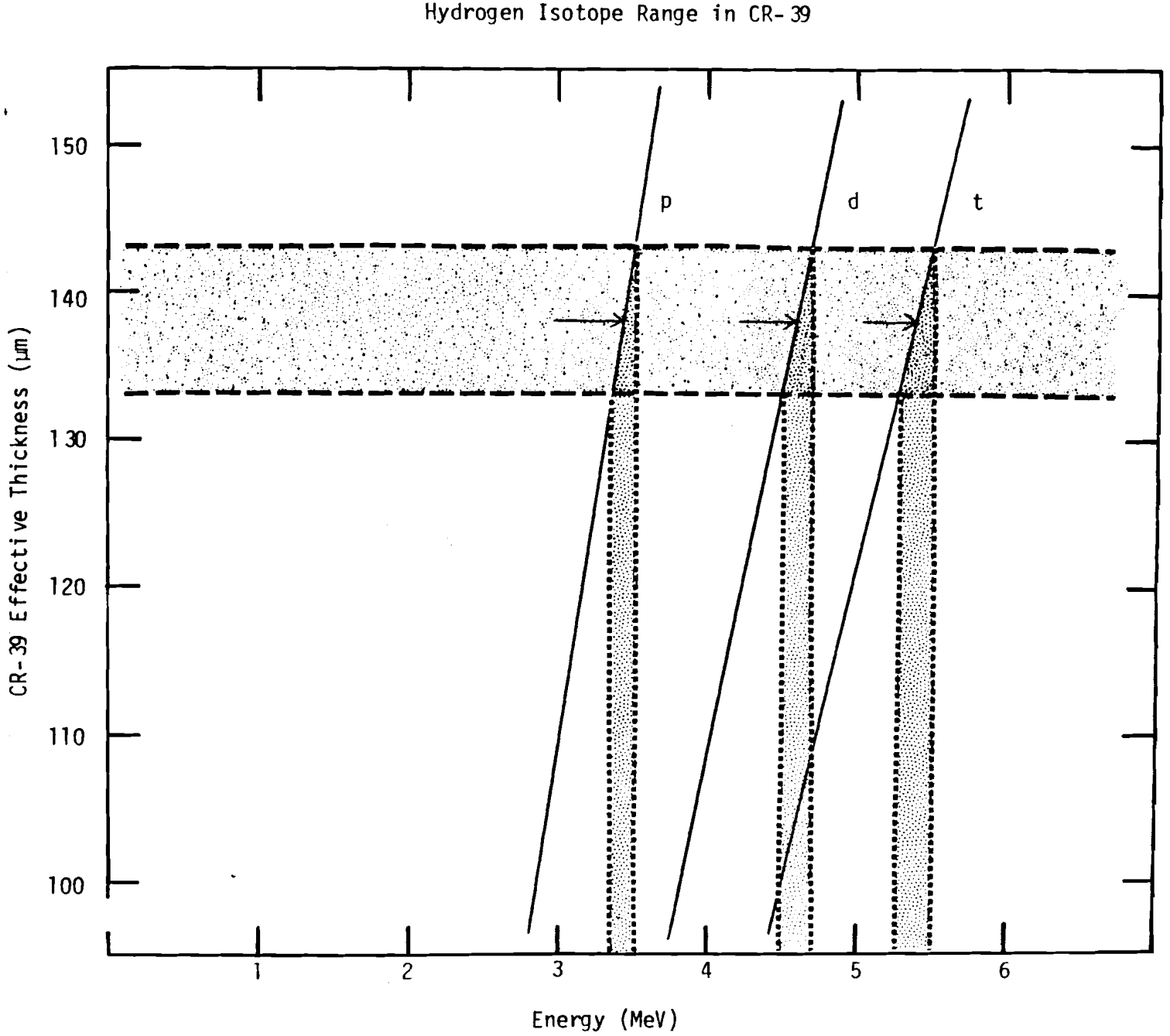
Hydrogen Isotope Range in CR-39
CR-39 Effective Thickness (μm)
150
140
130
120
110
100
p
d
t
1
2
3
4
5
6
Energy (MeV)

Figure 5.6

Each energy interval must next be translated back through the stopping foil to calculate the portion of the knock-on spectrum being measured. This requires the use of range information in tantalum which is supplied in Figure 5.7. For example, a deuteron with a mean energy of 4.6 MeV after traversing a 50 μm of tantalum (i.e., 83.3 mg/cm^2) requires an incident energy of 7.7 MeV. Columns four and five in Table II summarizes the incident knock-on energies defining the portion of each spectrum measured.

Knowing the portion of each spectrum measured it is now possible to calculate the effective cross section. Figures 4.1 and 4.2 show the cumulative distribution curves necessary to estimate Γ_d and Γ_t. These values are $(3.37 \pm .02) \times 10^{-2}$ and $(1.16 \pm .02) \times 10^{-1}$, respectively. Therefore, the effective cross section equals

$$\sigma_{eff} = \sigma_d \Gamma_t + \sigma_t \Gamma_t$$

$$= .62[(3.37 \pm .02)\times10^{-2}] + .92\,[(1.16 \pm .02)\times10^{-1}]$$

$$= (1.28 \pm .02)\times10^{-1}\ \text{b}$$

or $$\omega = \frac{\sigma_{eff}}{\sigma_d + \sigma_t}$$

$$= (8.3 \pm .1) \times 10^{-2}$$

where ω is the fraction of the total number of knock-on particles produced which fall into the acceptance energy interval.
It should be noted that the uncertainty in ω is actually larger than the value indicated above due to such effects as multiple scattering

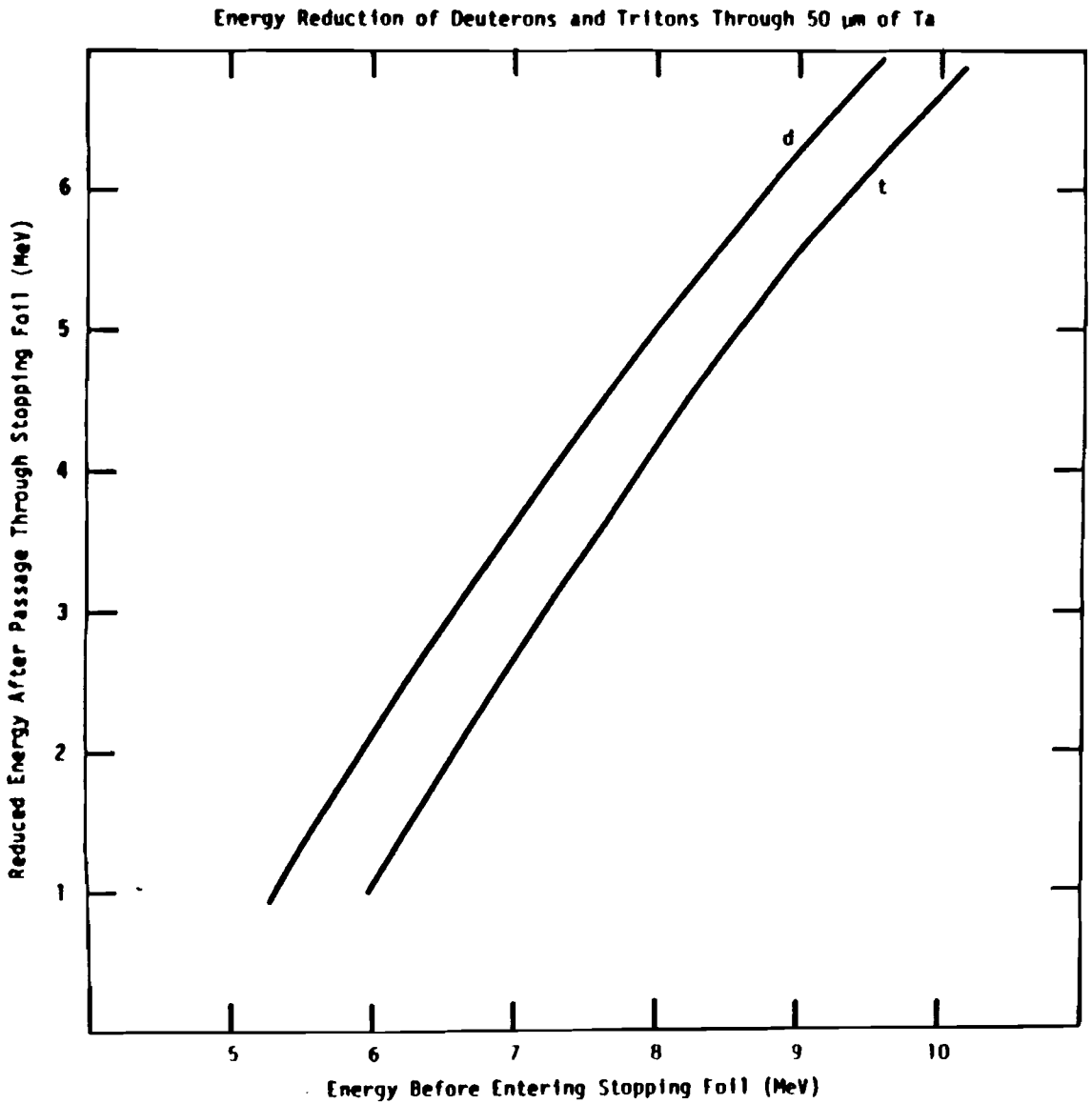
Energy Reduction of Deuterons and Tritons Through 50 μm of Ta
Reduced Energy After Passage Through Stopping Foil (MeV)
Energy Before Entering Stopping Foil (MeV)
d
t
1
2
3
4
5
6
5
6
7
8
9
10

Figure 5.7

in the tantalum foil, diameter smearing and uncertainties in the differential cross section. These contributions to the uncertainty in ω will be discussed further in the next section.

Calculation of the fuel ρR requires two final pieces of information namely the number of knock-ons counted in the collecting solid angle and the DT neutron yield. Returning to Figure 5.3 the total number of tracks above 12 μm is 95. However, this number is slightly inflated by a small portion of coincident protons falling between 12 and 13 μm. Using the number of non-coincidents found between 13 and 14 μm as an estimate for the number of protons existing between 12 and 13 μm, the total number of knock-on coincident tracks is reduced to 91.

The neutron yield is 5.5×10^8 for this particular shot. It had a measurement uncertainty of ± 10% [18]. Therefore the fuel ρR using equations 4-6 and setting $\nu = 1$ the ρR is found to be

$$\rho R = 5.4 \frac{Q}{Y_n} \left(\omega \frac{\Omega}{4\pi}\right)^{-1}$$

$$= 5.4 \frac{91}{5.5 \times 10^8} \left(0.083 \cdot 0.0092\right)^{-1}$$

$$= 1.2 \times 10^{-3} \text{ g/cm}^2$$

Measurement uncertainties in ω, Y_n, and Ω combine to produce an overall uncertainty of ± 22% in the ρR measurement. In addition, statistical fluctuations in the knock-on adds a ± 10% uncertainty in the measurement. Table 5.3 breaks down in further detail the contribution of each source.

Table 5.3

Parameter Values and Uncertainties Used in the Calculation of Fuel ρR

Type Uncertainty	Value of Parameter	± % Uncertainty in Value
ω	$(8.3 \pm .1)\times10^{-1}$	1
$\Omega/4\pi$	$(9.2 \pm 1.0)\times10^{-3}$	11
Y_n	$(5.5 \pm .5)\times10^{8}$	10
Q	91 ± 9	10

Only the contribution due to CR-39 thickness uncertainty has been included in the estimation of the uncertainty in ω.

Four additional effects have not been considered when calculating ω. These are

(1) energy straggling in the stopping foil,

(2) multiple scattering in the stopping foil,

(3) diameter smearing in the track detector and

(4) uncertainty in the measured differential cross section.

To understand the importance of these effects, a detailed analysis is presented in the following section and Appendix E.

E. System Distortion in the Knock-On Spectrum

This section will calculate the modified knock-on spectrum when diameter smearing, energy straggling, and range straggling are included. These results are compared with spectral data which show good agreement. Lastly, it will be shown that a 1% reduction in the value of ω results when these effects are included.

Data was obtained by integrating over 8 high-yield shots with an integrated yield of 2×10^{10}. The detector package consisted of a 150 μm CR-39 track detector covered with 50 μm of tantalum.

Figure 5.8 shows the diameter histogram of the data collected during these shots. The effective thickness was measured to be 138 μm implying a D* value equal to $\sim$ 12.4 μm. This is consistent with the cut-off value seen on the histogram.

Another feature on the histogram which shows excellent agreement with predicted results is the position of the triton forward-scattered peak. These tritons are reduced from 10.6 to 7.3 MeV after traversing the 50 μm of tantalum. Recalling from Chapter 3 that the mean track diameter is given by

$$D\ (\mu m) = 21.304\ (\frac{E}{A})^{-.4457} \qquad (5\text{-}1)$$

the corresponding predicted triton diameter peak should occur at $\sim$ 14.5 μm. This is additional proof that the track criteria can reject proton background tracks.

These simple calculations, however, fall short in explaining the quantitative structure of the spectrum. Indeed, Figure 5.9 shows the

MEASURED KNOCK-ON SPECTRUM

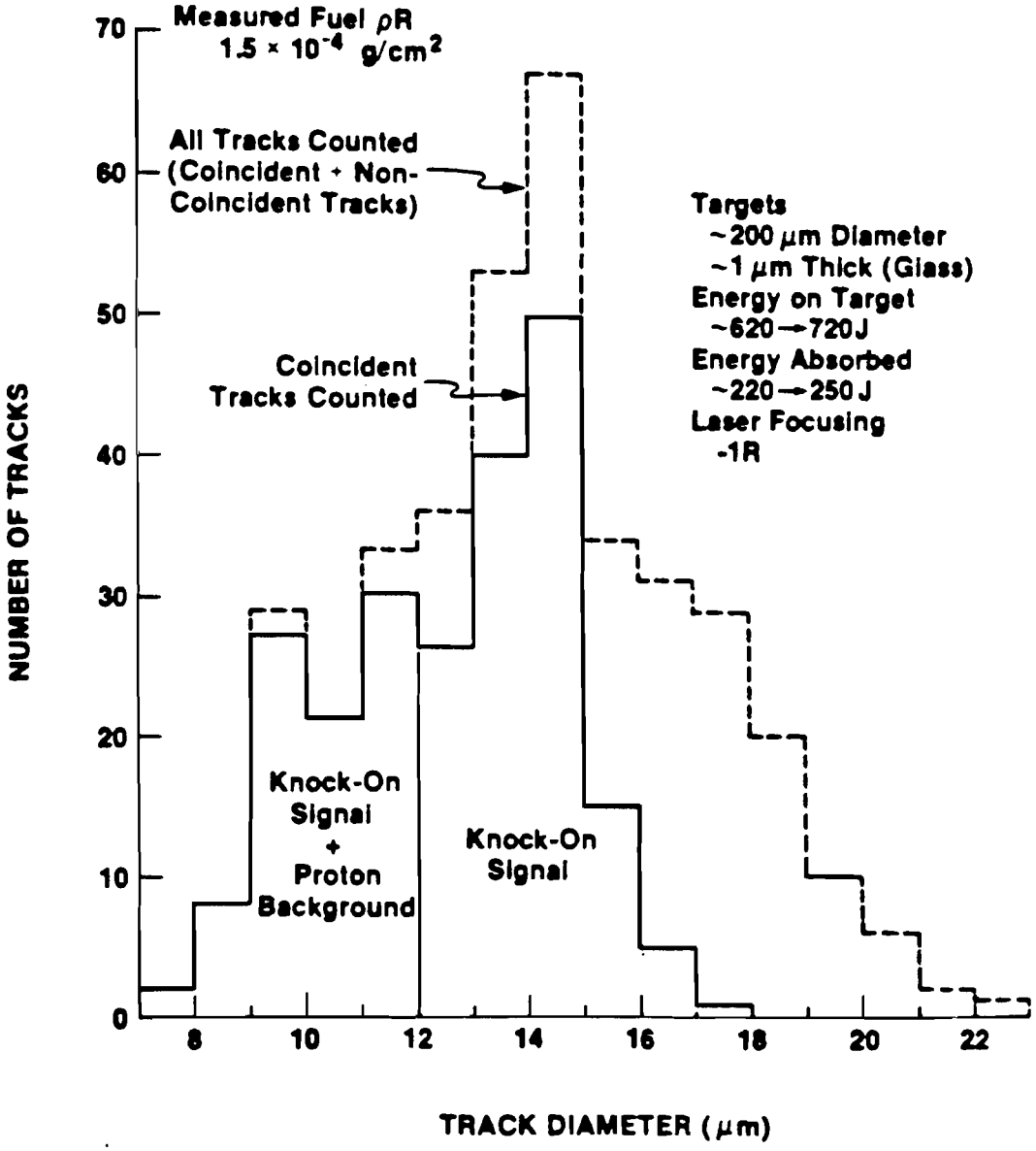

E1458

Figure 5.8

DIAMETER SPECTRUM WITHOUT DIAMETER SMEARING OR ENERGY STRAGGLING

UR LLE

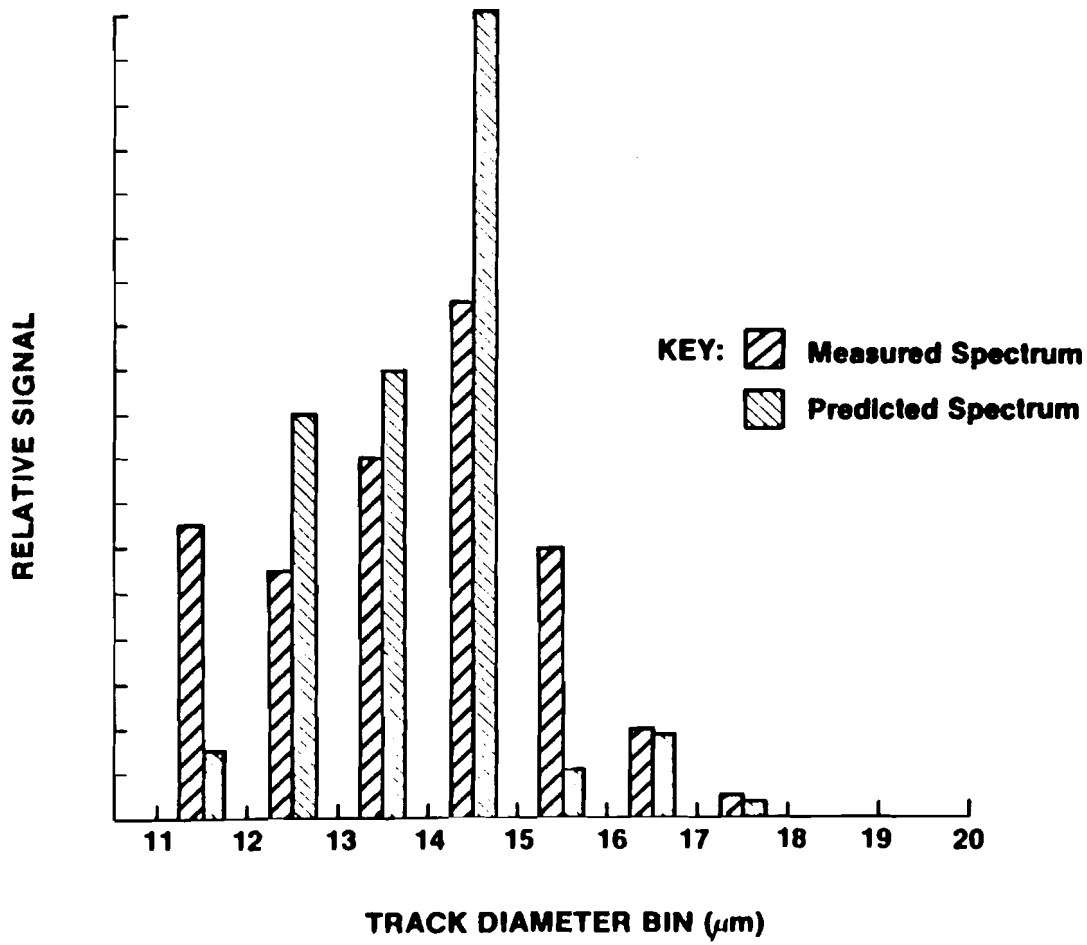

Figure 5.9

E1819

peak being much larger than is actually measured. The fit can be substantially improved upon by including energy straggling in the tantalum foil and diameter smearing in CR-39.

Recall that diameter smearing is the spread in track diameter about a mean value, which is energy dependent, resulting from localized variation in the bulk etch rate across the detector surface. As was discussed in Chapter III this smearing has a measured standard deviation of 0.5 μm and is approximately energy independent. Energy straggling was estimated using thin foil approximations to be between 100 and 200 KeV, however, larger straggling up to 500 KeV does not significantly alter the distribution.

To simulate these effects, a Monte Carlo procedure is used to generate the knock-on particles weighted by each of their appropriate energy differential cross sections and passed through a tantalum foil. The mean energy loss is calculated using standard stopping power tables for tantalum. Energy straggling is artificially introduced by assuming a gaussian distribution and randomly distributing particles into energy bins.

By using equation (1) along with knowledge of the probability smearing function (i.e., approximately gaussian) and the knock-on energy distribution after passing through the tantalum foil, the expected diameter distribution is generated. Particles with ranges greater than the effective detector thickness are counted as spatial coincident tracks. It should be noted that multiple scattering in the tantalum foil is not important as shown in Appendix E.

By knowing the initial number of particles generated and the final number of coincident tracks directly yields the effective cross section.

Figure 5.10 is the generated spectrum compared with the measured spectrum when energy straggling and diameter smearing are included. The enhancement of the predicted signal in bin 11 is due to diameter smearing of high energy deuterons contributing to the lower energy bins. Notice also that the predicted peak in bin 14 is reduced relative to the uncorrected spectrum. This is attributed to energy straggling in the tantalum.

Comparison of the initial-to-final numbers of particles producing coincidences indicate that ω has a value of $\sim .082$. This small reduction in the value of ω is attributed to the fact that (1) the upper energy limit of the acceptance window is well above the triton cut-off energy and (2) the lower energy limit lies near the spectrum minimum. Therefore, no significant changes in the ρR measurement discussed in the last section will occur due to either energy straggling or diameter smearing.

Uncertainty in the differential cross section has not been included in this analysis. Tabular information of these cross sections are given in reference (2) but no estimates or references were given for the measured uncertainty in these cross sections.

F. Target Compression Performances

Returning to Table I, two experimental conditions were explored. Short pulse experiments ($\sim$ 90 psec) delivered about 700 J on target

DIAMETER SPECTRUM WITH DIAMETER SMEARING AND ENERGY STRAGGLING

UR LLE

Proton Background Corrections Made in Bins 11 and 12

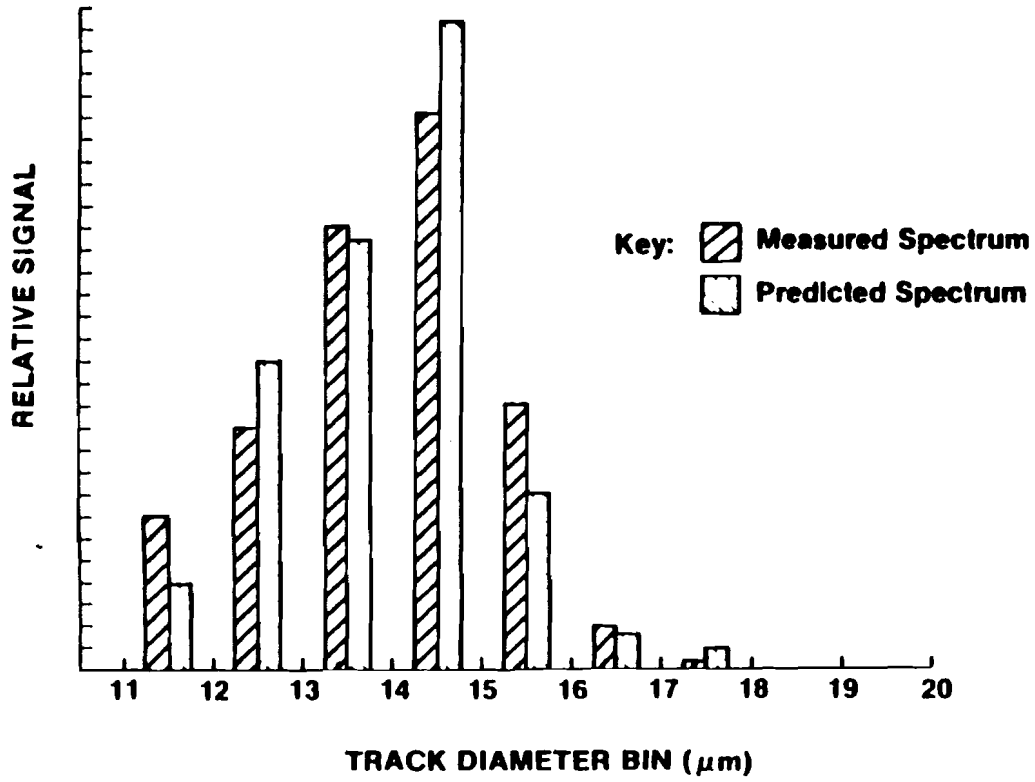

Figure 5.10

with peak intensities of 2×10^{16} w/cm^2. Unlike the long pulse experiments, these short pulse experiments integrated data over multiple shots. This shortcoming was the result of initial debugging of the diagnostic and the inability during these early experiments to retract the track detector package.

Computer simulations indicate that the high intensities encountered in the short pulse studies produced strong shocks and energetic electrons with an effective temperature of 35 KeV, which heated the fuel. The resulting high fuel pressure precluded a high density compression.

In contrast, the long pulse experiments had a peak intensity of $\sim 4 \times 10^{14}$ w/cm^2 with 2 KJ delivered on target in $\sim$ 1 nsec. The generated shocks were weaker and the amount of suprathermal electrons smaller than compared with the short pulse studies. The smaller fuel pressure resulted in larger density compressions.

The fuel ρR measurement support this general description. For the short pulse studies, the fuel ρR fell in the low 10^{-4} g/cm^2 regime. This value was increased 10-fold when laser conditions were changed to long pulse.

The measured values are also in good quantitative agreement with numerical simulation results. Figure 5.11a shows that after 1.5 nsec into the shot, the neutron production rate is maximum. The predicted fuel ρR variation shown in Figure 5.11b gives a localized ρR. The time average fuel ρR based on Lilac simulations (see Appendix G) and weight with the neutron production rate was calculated to be 1.6×10^{-3} g/cm^2.

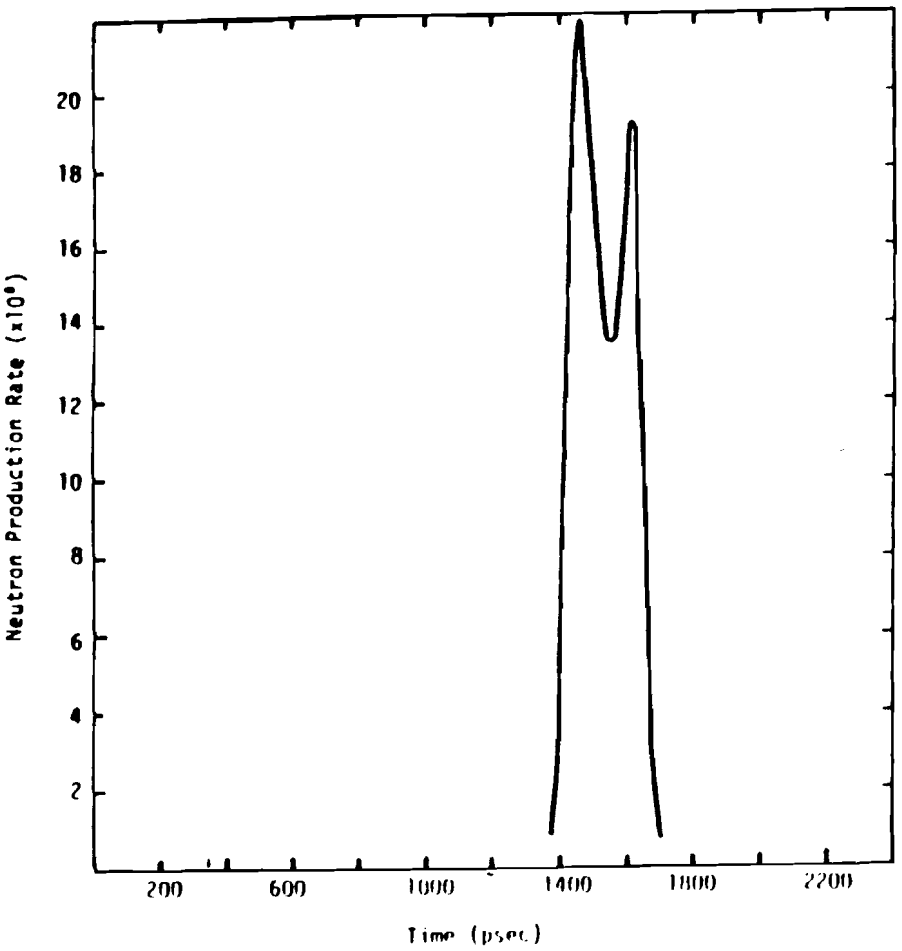

Figure 5.11a

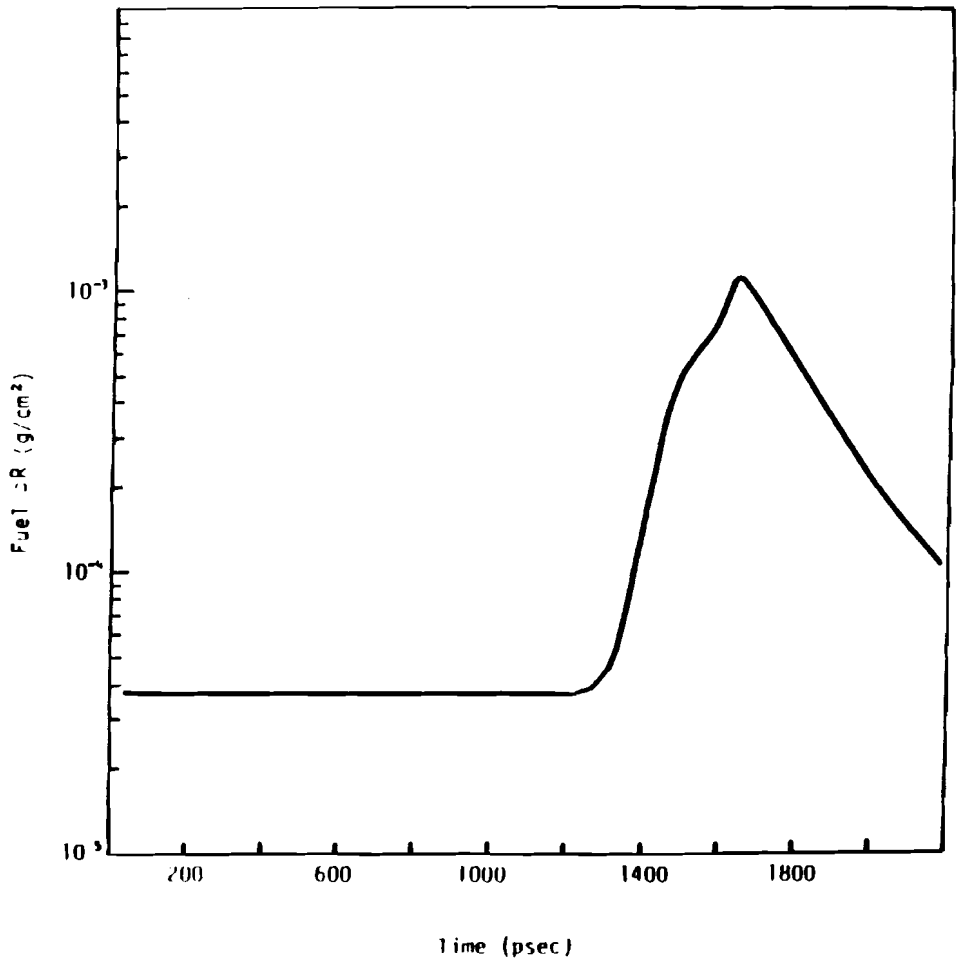

Figure 5.11b

VI. THE EXTENSION OF THE ρR KNOCK-ON MEASUREMENT TO MODERATE ρR CONDITIONS

A. Chapter Overview

In the previous chapters the target ρR has been assumed to be small enough not to produce distortions in the knock-on spectrum. This assumption breaks down when target ρR conditions exceed about 3 mg/cm^2 and corrections in the effective cross section are necessary. Compounding the problem, uncertainties in the tamper (i.e., glass shell) ρR and temperature translate into uncertainty in σ_{eff} if correlation techniques are not used.

Another factor which introduces uncertainty in σ_{eff} is the degree in which the track detector thickness is known. This uncertainty is looked at as a function of target ρR.

Other factors leading to uncertainty in σ_{eff} such as tantalum foil thickness and bulk etch rate are small and have been discussed earlier in this work. Therefore, the emphasis of this chapter is on the extension of the knock-on measurement to the moderate ρR conditions and to examine how the σ_{eff} changes with target conditions and track detector thickness. Methods will also be discussed as how to minimize the uncertainty in σ_{eff}.

Section B will examine the effects that target conditions influence the uncertainty in σ_{eff}. This section will develop two potentially useful approaches to minimize σ_{eff}. One approach will

correlate the DD-proton energy loss to the effective cross section. Another approach presented will correlate the ratio of knock-on counts from two closely spaced energy intervals to the effective cross section.

In Section C the consequence of the uncertainty in measuring the track detector on σ_{eff} will be explored. The two approaches discussed above will be examined in context to this type of uncertainty.

In Section D the ratio approach will be used to extend the knock-on measurement to about 70 mg/cm^2. An overview of threshold requirements over the entire ρR regime will also be addressed in this section.

B. The Examination of Two Schemes to Minimize the Effects of Uncertainty in σ_{eff} Due to Target Conditions

In the simulation calculations below, neutrons were generated uniformly and isotropically throuhout the fuel. The knock-on particles were all assumed to be forward-scattered. If measurements are centered about the deuteron or triton peak, such an approximation give excellent agreement with more correct Monte Carlo transport calculations.[19] As the knock-on particles traversed the fuel and tamper, their energy was reduced predominantly as a result of energy exchange with electrons. The energy loss was calculated using an expression similar to that of Longmire but was corrected for (in the logarithm term) degenerate effects.[20] This loss is predominantly a function of target ρR and electron temperature.

Since one has no prior knowledge of the target conditions during a particular shot, one is faced with the prospect of examining various foil thickness systems to find an optimal system whose effective cross section changes least with expected ρR and temperature extremes. Examining Figure 6.1, once again it is seen that the 120 μm tantalum foil system has the lowest fractional uncertainty over a wide range of tamper ρR. Assuming an effective cross section of .0675 barns the maximum uncertainty over this range is ± 10%.

The slow variation of the cross section can be attributed to two factors. First, this foil system translates the high energy deuteron peak into the acceptance window of the track detector. As shown in Figure 6.2, as the ρR increases, the particles leaving and the window is small over the entire ρR range. Below about 4×10^{-3} g/cm^2 the deuteron peak has not yet entered the acceptance window. Above 4×10^{-3} g/cm^2 the fractional window decreases because of the lower energy deuterons leaving the acceptance window. Since these particles leaving the window comprise a very small portion of the knock-on signal, they do not greatly affect the effective cross section. The second factor which tends to reduce the variation in the fractional window is the weak dependence on tamper temperature. This is due to the high energy deuterons having velocities very much higher than the electron thermal velocity.

The 40 μm tantalum foil system is another potential candidate which must be considered. Figure 6.1 shows that this system will

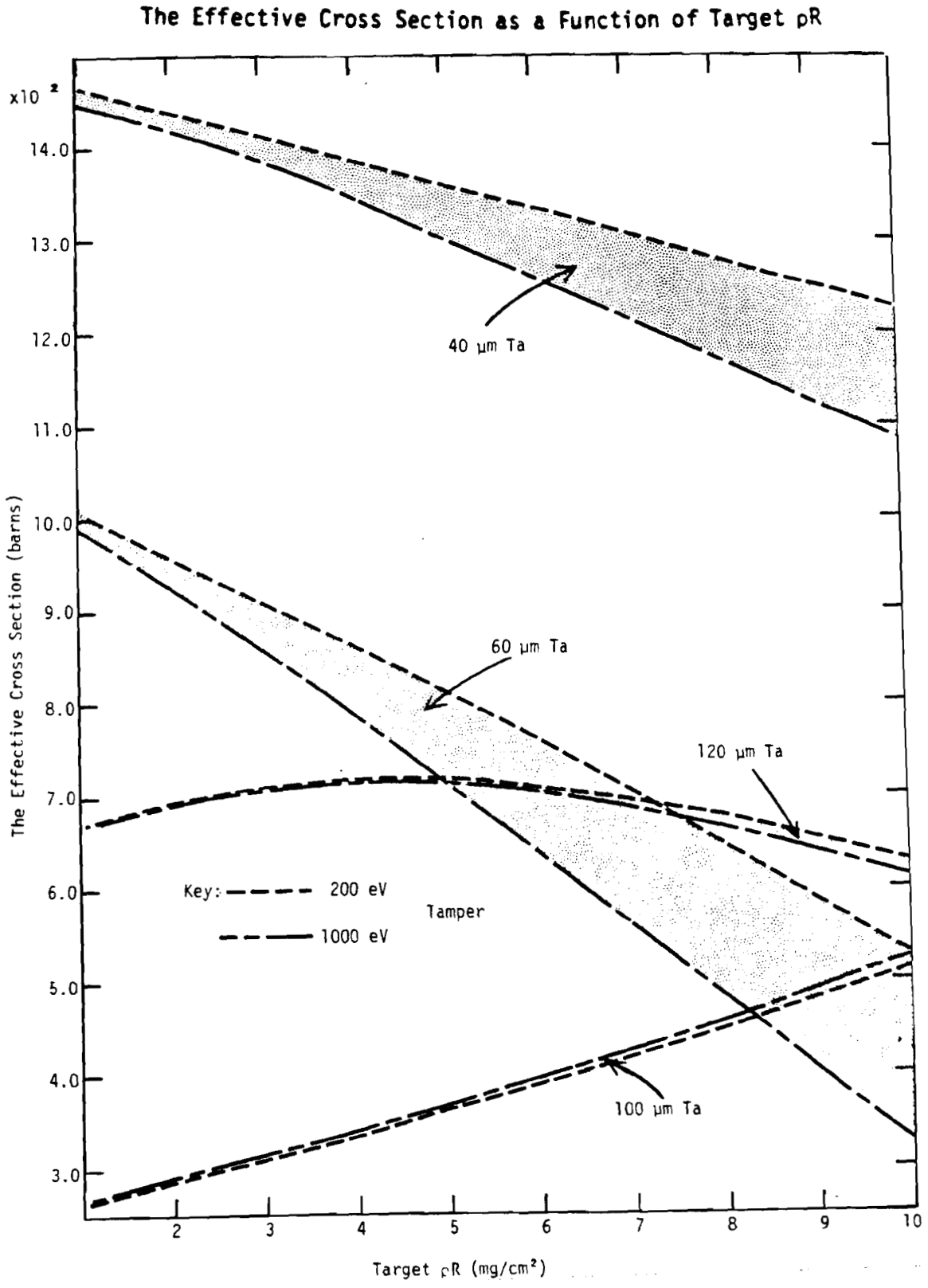
The Effective Cross Section as a Function of Target ρR
x10 ²
14.0
13.0
12.0
11.0
10.0
9.0
8.0
7.0
6.0
5.0
4.0
3.0
The Effective Cross Section (barns)
40 μm Ta
60 μm Ta
120 μm Ta
100 μm Ta
Key: 200 eV
1000 eV
Tamper
2
3
4
5
6
7
8
9
10
Target ρR (mg/cm²)

Figure 6.1

Spectral Distortion Due to Target ρR

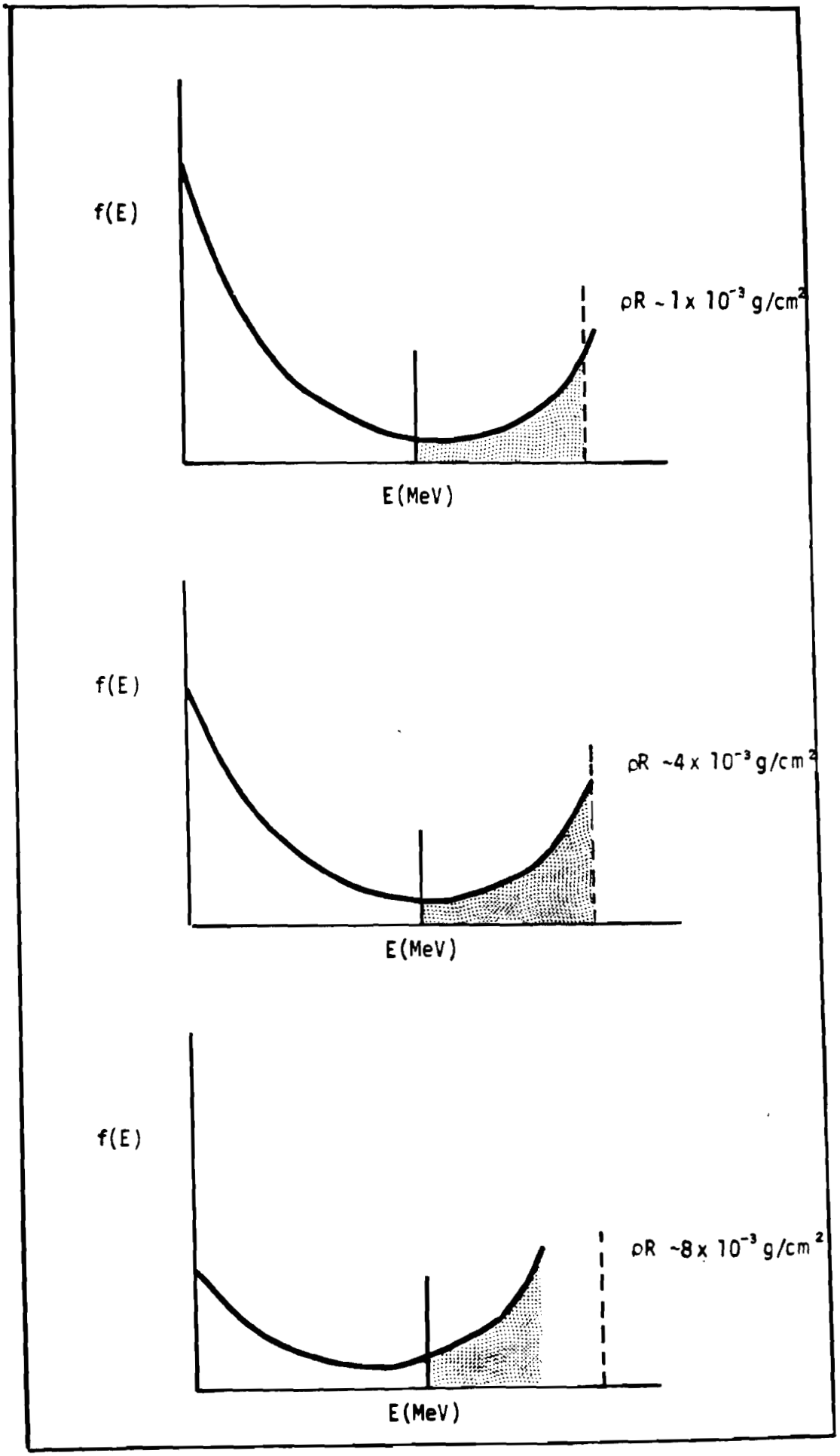

Figure 6.2

increase the knock-on effective cross section. A thinner foil cannot be used in this ρR regime because the DD-protons would penetrate the foil. The 40 μm foil has the advantage over the 120 μm foil system in that the effective cross section is twice as large. The price one pays is a higher fractional uncertainty of ± 16% if one assumes an effective cross section of .126 barns.

This uncertainty can be reduced by using one of two approaches. The first approach is to correlate the effective cross section with the DD-proton energy loss. It is fortunate that high energy forward scattered tritons have velocities similar to those of the DD-protons. It therefore is expected that any energy loss of the protons would be closely correlated with the triton energy loss. Figure 6.3 shows this correlation for two extreme temperature limits of 200 and 1000 eV for the case of a 40 and 60 μm foil system. As expected, the 60 μm system is less correlated with the DD-protons energy than the 40 μm system because of the greater velocity difference between the tritons and protons.

The energy loss of the DD-proton can be measured with the existing time-of-flight system at LLE. Since the transmission for the system is 10^{-4} a DD-proton yield of about 10^{6} is required to record a measurable signal. The energy resolution for the system is about ± 200 KeV. Therefore, the maximum uncertainty of the effective cross section will be approximately ± 5%. This approach works well up to a ρR of 10^{-2} g/cm^2 beyond which it may become difficult to separate background protons, arising from pump oil contamination on the microballoon surface, from the DD-protons.

USEFUL FRACTIONAL SIGNAL CORRELATED WITH THE DD-PROTON ENERGY

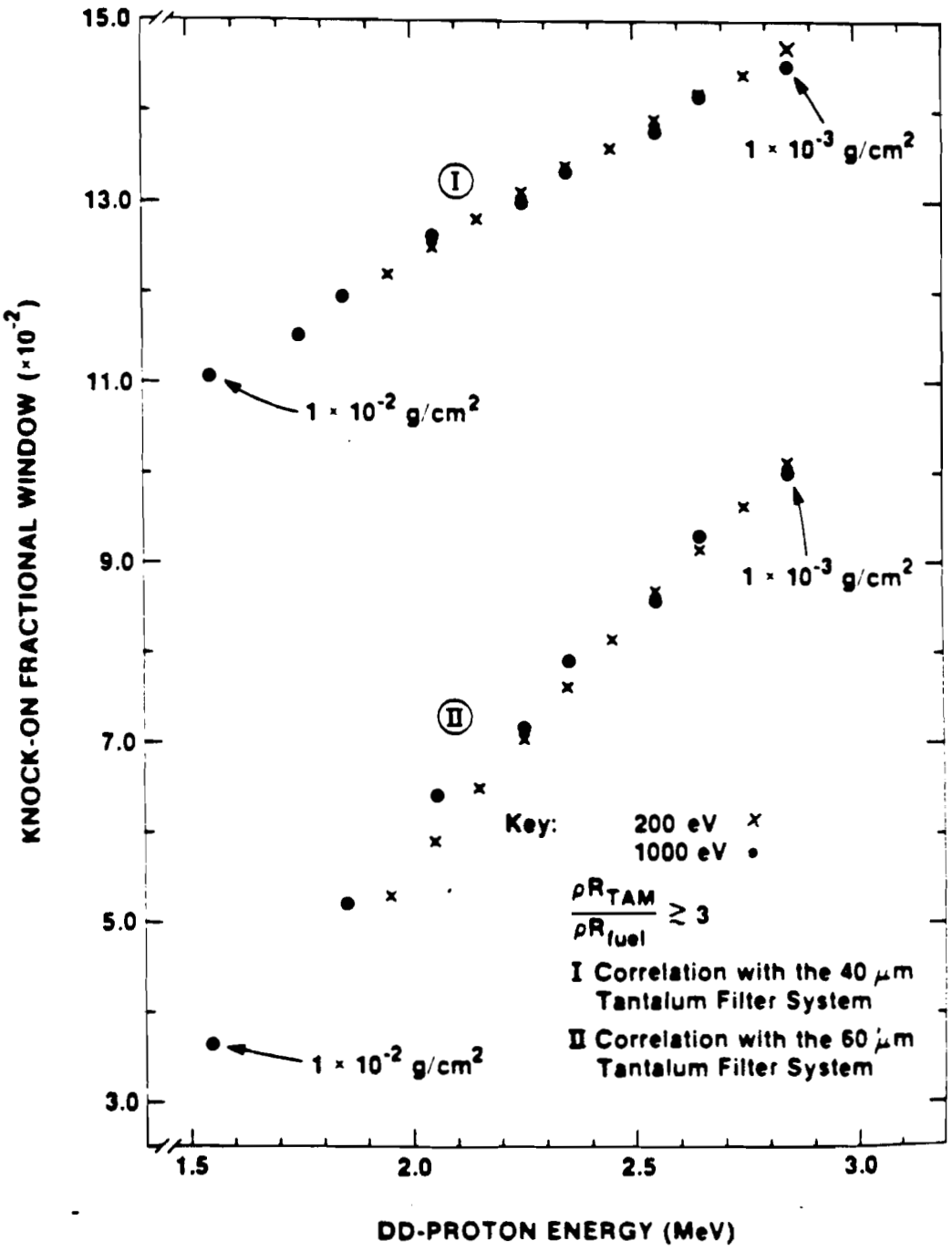

Figure 6.3

E1727

A second approach in estimating the effective cross section is to measure the ratio of two separate foil systems and then to correlate this ratio with the effective cross section. Figure 6.4 shows the underlying idea behind this approach. Two energy bins are selected relatively close to each other so that temperature affects the two bins approximately equally. The ratio of the number of particles found in each bin gives information of the positioning of the bins relative to the knock-on distribution. Calculations show that not much variation in this ratio occurs over much of the ρR parameter space if the tantalum foil difference is less than 20 μm. Therefore, a compromise was reached to insure reasonable ratio variation and the ability to remove the temperature uncertainty of the foil and tamper. The tantalum thickness difference was set at 20 μm and various foil combinations were examined.

When using the signal-ratio approach, one must decide which foil combination is optimal. As already discussed, a difference of about 20 μm in thickness between the two foils will produce a meaningful ratio. Another consideration is what the actual foil thicknesses should be. Computer calculations show that two foil systems have unique attributes which tend to minimize the uncertainty in the effective cross section. The first system consists of a 100 and 120 μm foil pair. As shown in Figure 6.5 the ratio is first fairly insensitive to the temperature and second, the window is relatively flat over the domain of signal ratio. The second system consists of a 40 and 60 μm pair of tantalum foils. Here the effective cross section is about twice as large as the first system. However, this 40/60 system

A GRAPHIC DESCRIPTION SHOWING THE UNDERLYING IDEA BEHIND THE RATIO TECHNIQUE

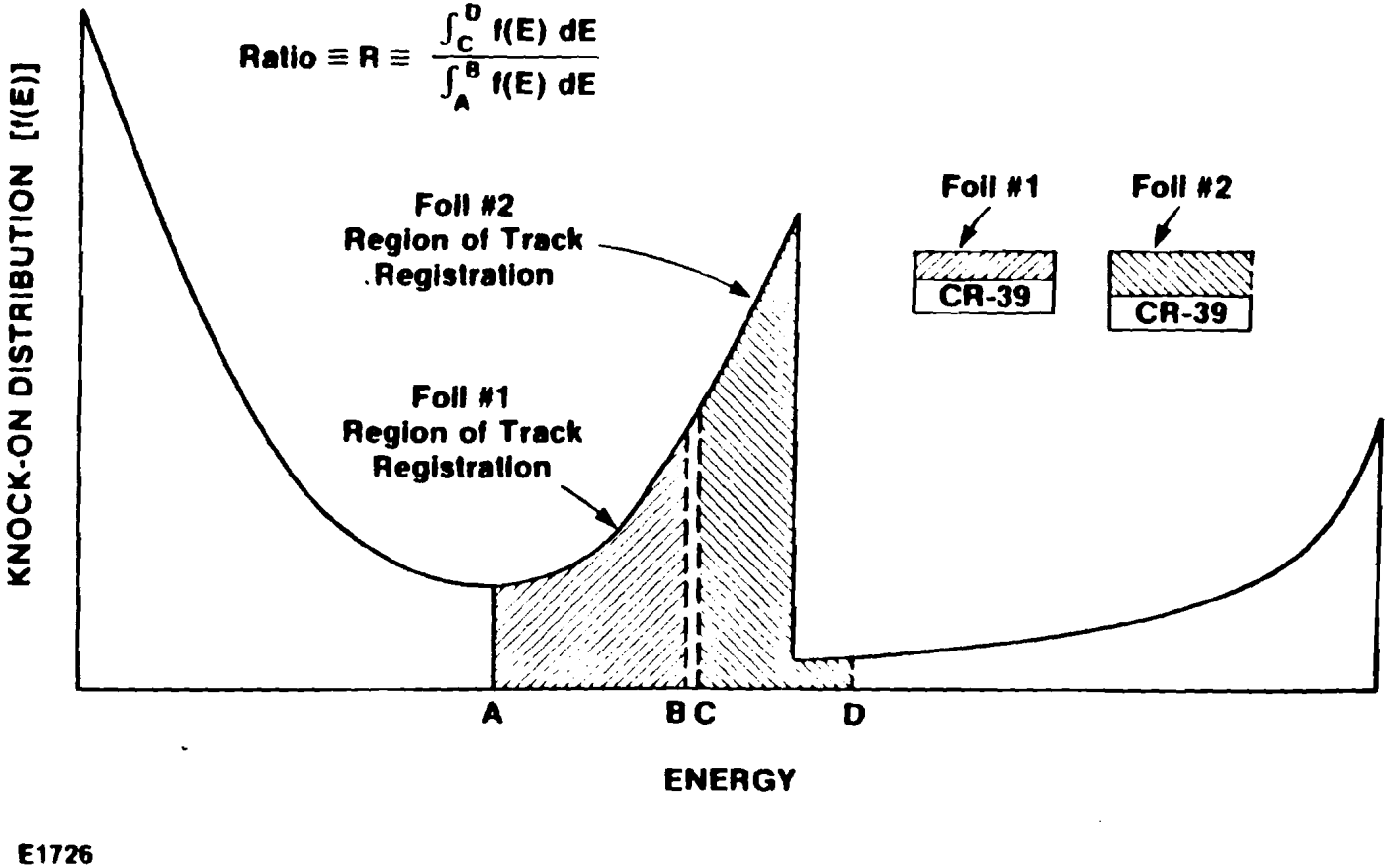

Figure 6.4

USEFUL FRACTIONAL SIGNAL VERSUS KNOCK-ON NUMBER RATIO

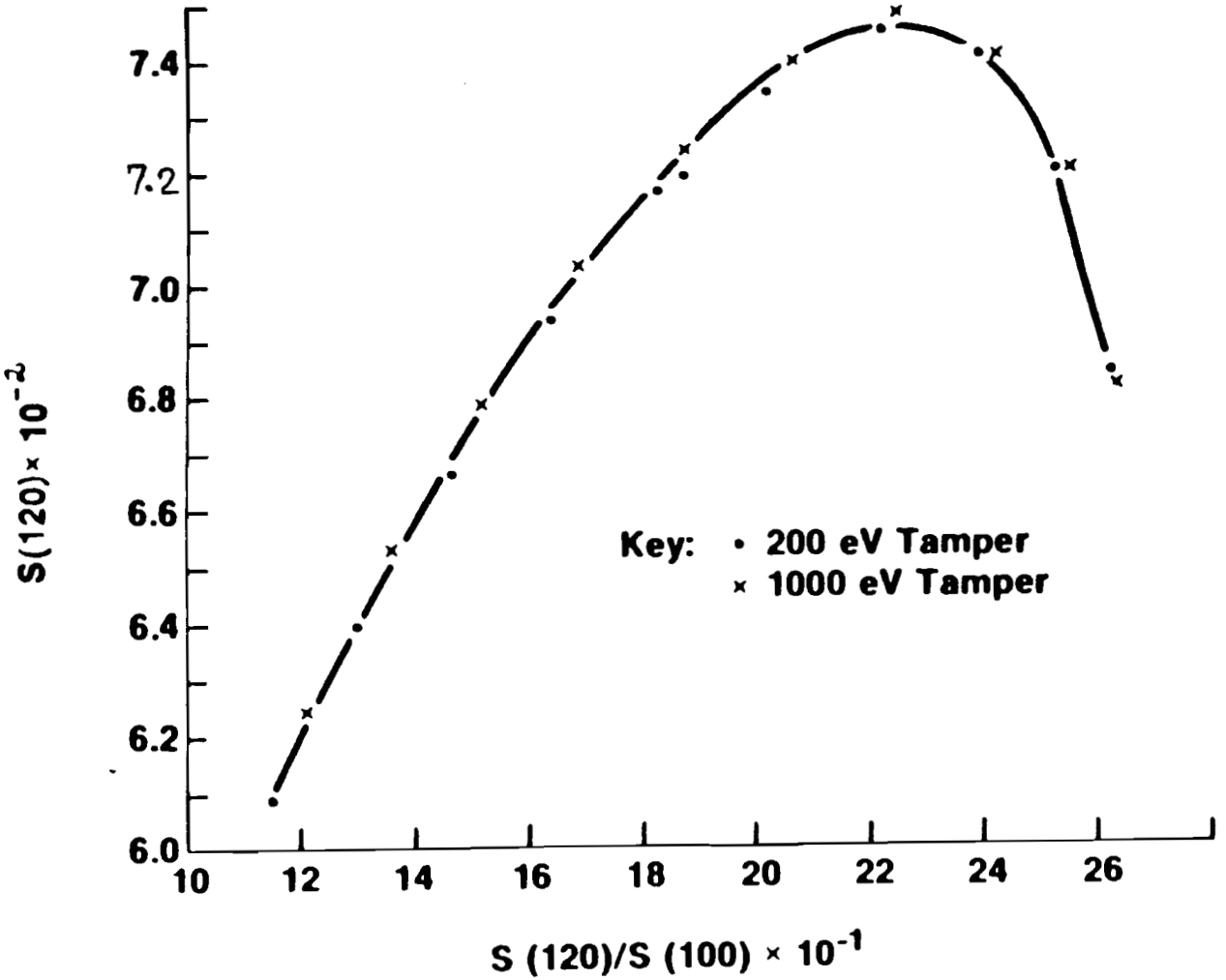

shows a greater temperature dependence and is not nearly so flat as the 100/120 system. Figure 6.6 shows the fractional window plotted against ratio for the 40/60 system. To decide which is the better of the two systems, one must fold in the effects of uncertainty of CR-39 thickness into the calculations.

In summary, this section has established that if one is interested in reducing the effective cross section uncertainty over the entire 10^{-3} to 10^{-2} ρR regime, two approaches are possible. The first method requires the use of a time-of-flight spectrometer to measure the DD-proton energy loss. This loss is closely correlated with the effective cross section. The disadvantages with this approach are that it requires an additional diagnostic and can be used only up to a ρR of about 10^{-2} g/cm^2. The second approach requires the use of two track detector systems each covered with different foil thicknesses. The ratio obtained is strongly correlated with the effective cross section. The disadvantages with this approach are that it requires twice the solid angle and is not quite as temperature independent as the energy loss approach.

Before deciding which of these methods is best, careful consideration will now be given to the role that detector thickness uncertainty plays in the calculation of the effective cross section. This will lead into a discussion as to which system performs best with the introduction of this new uncertainty.

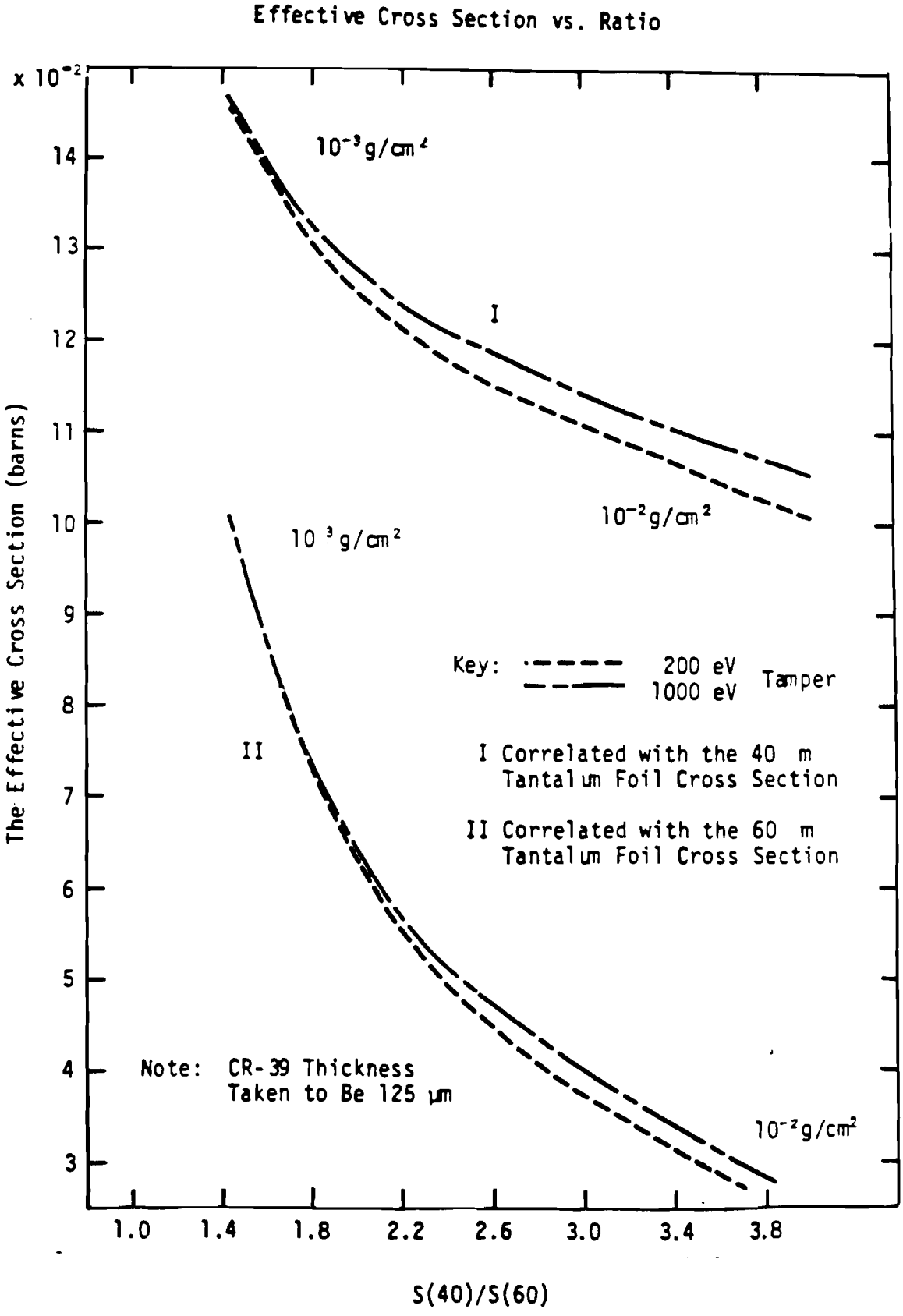
Effective Cross Section vs. Ratio
x 10⁻²
14
13
12
11
10
9
8
7
6
5
4
3
The Effective Cross Section (barns)
10⁻³g/cm²
I
10⁻²g/cm²
10⁻³g/cm²
II
Key: 200 eV
1000 eV
Tamper
I Correlated with the 40 m Tantalum Foil Cross Section
II Correlated with the 60 m Tantalum Foil Cross Section
Note: CR-39 Thickness Taken to Be 125 μm
10⁻²g/cm²
1.0
1.4
1.8
2.2
2.6
3.0
3.4
3.8
S(40)/S(60)

Figure 6.6

C. Thickness Variation in Track Detectors and Its Implications on Estimating the Effective Cross Section

Section B gave detailed analysis showing variation and uncertainty estimates in σ_{eff} as functions of target conditions. Here another factor, detector thickness, will be examined for ρR conditions up to 10 mg/cm^2.

Typically, track detectors used were punched out of square samples 2" x 2". Thickness variations across the sheet were measured to be as high as 50% (especially for very thin detectors $\sim$ 80 μm average thickness). These variations were not random but rather showed a constant thickness gradient. After one-inch discs were punched out of the sheet, thickness variations of no more than 20 μm were accepted on any given disc.

The analysis which follows is based on the worse case situation to establish maximum uncertainty in σ_{eff}. Two factors which contribute to its uncertainty is (1) the accuracy to which the thickness variation can be measured and (2) the degree of systematic uncertainty in the thickness measurement.

A model can be described which relates thickness variations across the disc to the uncertainty in σ_{eff}. In Figure 6-7 below, T1 and T2 denote the minimum and maximum points on the disc. The thickness gradient is directed in the positive y-direction.

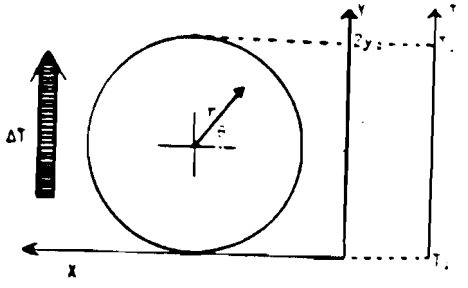

No thickness variation is assumed in the x-direction. Therefore, the thickness can be simply expressed as

$$T(x,y) = \frac{T_2 - T_1}{2y_o} \; y + T_1$$

Computer calculations showed that $\sigma_{e\delta\delta}$ is approximately linear over thicknesses between 115 and 135 μm, as shown in Figures 6.8 and 6.9. Therefore $\sigma_{e\delta\delta}$ can be determined for each point on the disc given by (using polar coordinates)

$$\sigma_{e\delta\delta}\,(r,\theta) = \frac{\sigma_2 - \sigma_1}{y_o}\, r\, \mathrm{Sin}\theta + \tilde{\sigma}$$

where

$$\tilde{\sigma} \equiv \frac{\sigma_1 + \sigma_2}{2}$$

and where σ_1 and σ_2 denote the value of the effective cross sections at thicknesses T_1 and T_2, respectively.

Since the thickness is not a constant across the detector, it is not possible to assign a unique $\sigma_{e\delta\delta}$ to the detector. However, it is possible to calculate an average effective cross section $\tilde{\sigma}_{e\delta\delta}$ given by

$$\tilde{\sigma}_{e\delta\delta} = \frac{1}{y_o^{\,2}} \int_0^{2\pi} \int_0^{y_o} \sigma_{e\delta\delta}\,(r,\theta)\; r\; dr d\theta$$

$$= \tilde{\sigma}$$

The Effective Cross Section Registered by Various Thickness Pieces
of CR-39 Under Two ρR Conditions.
Tantalum Foil Thickness of 40 and 60 μm Are Shown Below.

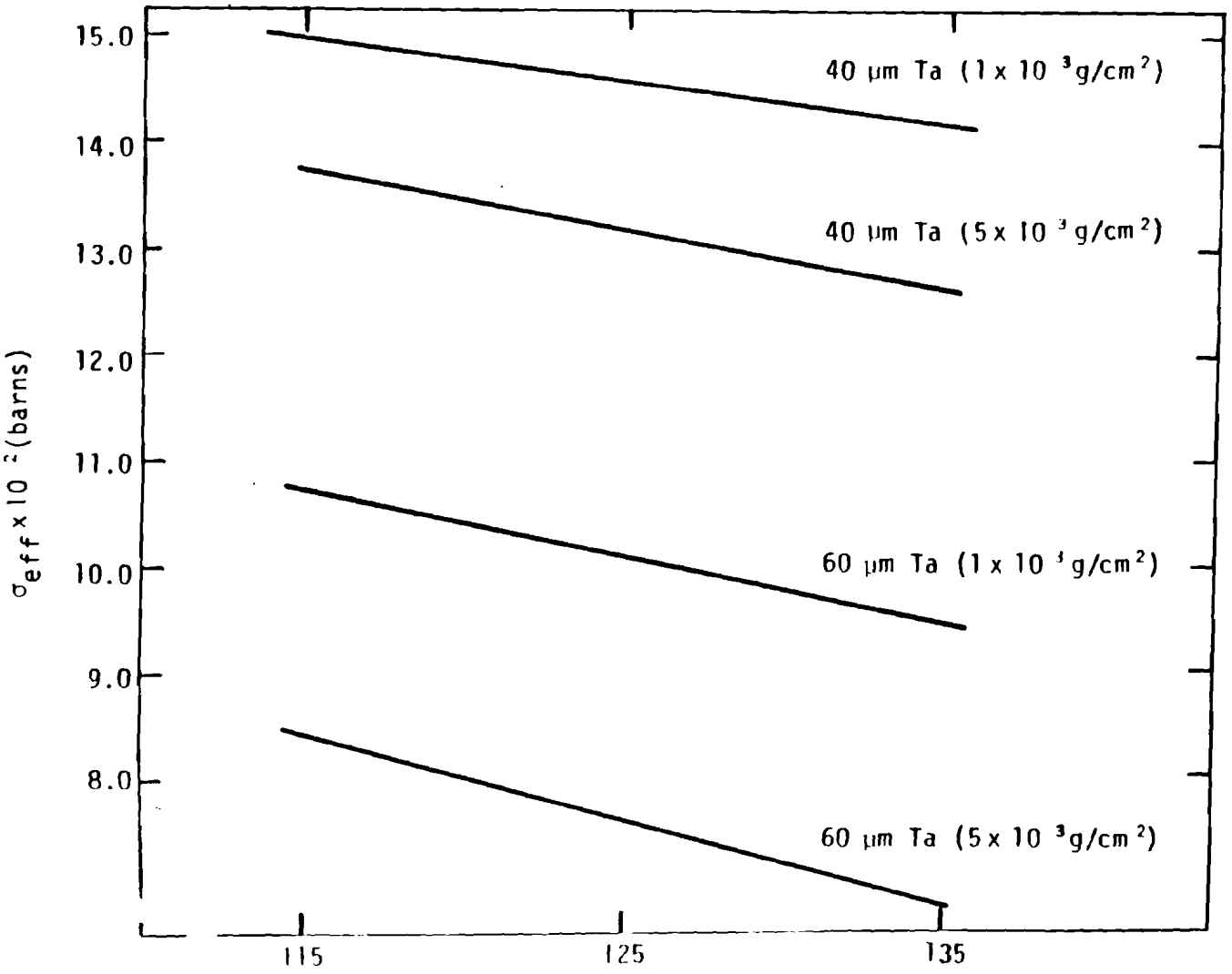

Figure 6.8

The Effective Cross Section Registered
by Various Thicknesses of CR-39 Under Two ρR Conditions.
Tantalum Foil Thicknesses Are 100 and 120 μm

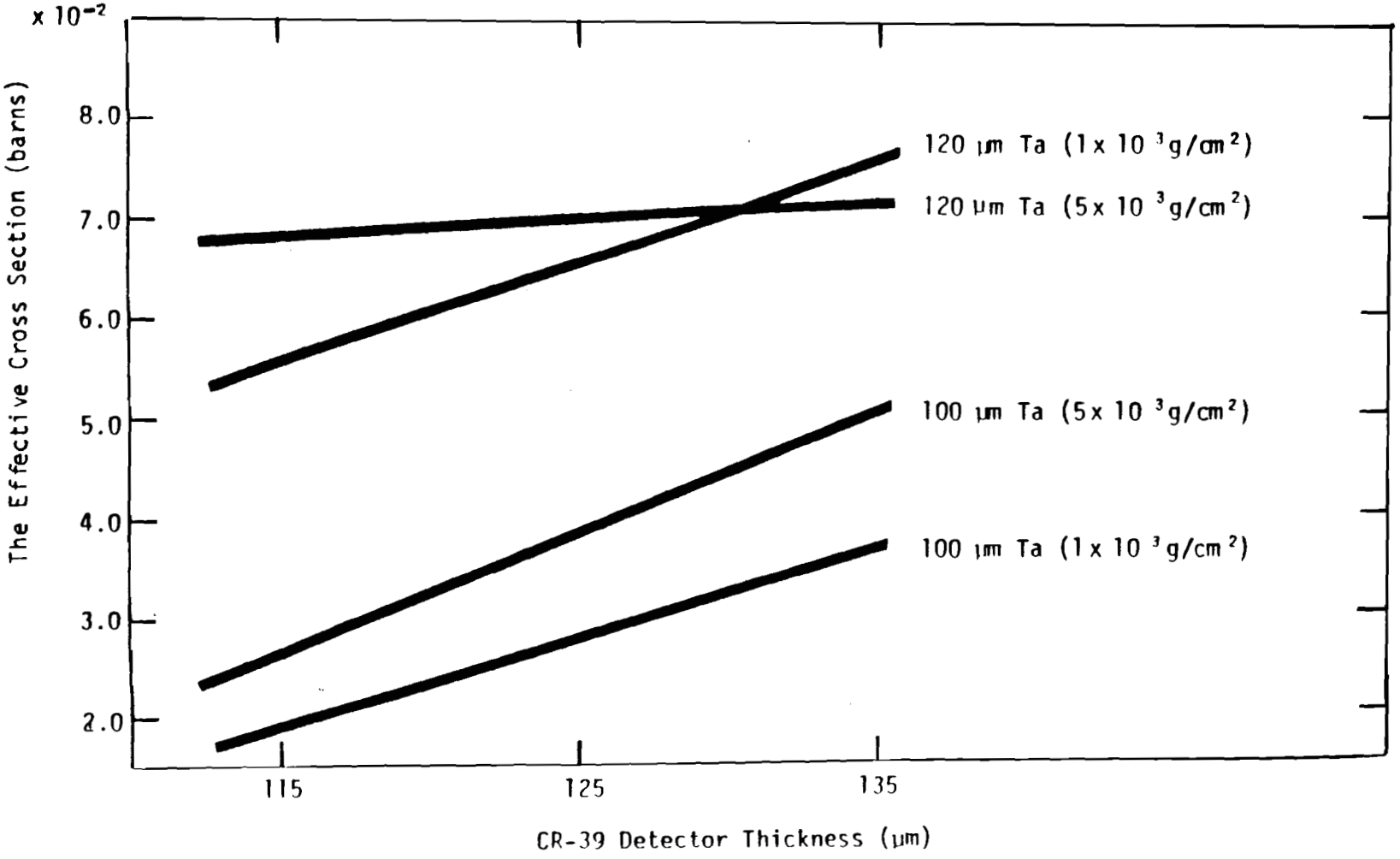

Figure 6.9

Because of the measuring resolution of the micrometer, ε_r, estimates for T_1 and T_2 will result in uncertainty in $\tilde{\sigma}_{eff}$ given by

$$\delta \tilde{\sigma}_{eff} = \varepsilon_r \left. \frac{\partial \sigma_{eff}}{\partial T} \right|_{T=T_1,\ T_2}$$

By inspection of the slopes in Figures 6.8 and 6.9 detectors covered with 40 μm of tantalum give the smallest uncertainty in $\tilde{\sigma}_{eff}$ for low 10^{-3} g/cm^2 regime. By the mid 10^{-3} g/cm^2 regime, however, the 120 μm tantalum filter system shows the least uncertainty in $\tilde{\sigma}_{eff}$. It is therefore necessary to examine the trade-off in uncertainty in $\tilde{\sigma}_{eff}$ under various ρR conditions when applying either the ratio or the DD-proton energy loss method.

Tables 6.1 and 6.2 summarize the data required for this analysis. The cross section σ_1 and σ_2 are evaluated for detector thicknesses of 115 and 135 μm, respectively. Tamper electron temperature is taken to be 600 eV. These tables can be used to generate the maximum and minimum ratios so as to estimate the uncertainty in $\tilde{\sigma}_{eff}$. Figures 6.10 and 6.11 show that the 40/60 filter system never exceeds about ± 10% in its estimate of $\tilde{\sigma}_{eff}$. However, as much as 20% uncertainty is present if a 100/120 filter system is used.

The effect of thickness uncertainty in the DD-proton energy loss method also produces uncertainty in $\tilde{\sigma}_{eff}$. Figure 6.12 shows the spread in $\tilde{\sigma}_{eff}$. Again the tamper electron temperature is taken

Table 6.1

40 μm tantalum filter

$\rho R(mg/cm^2$	$\sigma_1 \times 10^2$	$\sigma_2 \times 10^2$	$\tilde{\sigma}_{eff} \times 10^2$	$\pm \delta \tilde{\sigma}_{eff}$
1	14.9	14.1	14.50	.20
2	14.6	13.7	14.15	.23
3	14.3	13.3	13.80	.25
4	14.0	13.0	13.50	.25
5	13.7	12.6	13.15	.28
6	13.4	12.2	12.80	.30
7	13.0	11.8	12.40	.30
8	12.7	11.4	12.05	.30
9	12.3	11.0	11.65	.33
10	11.9	10.5	11.20	.35

60 μm tantalum filter

1	10.8	9.58	10.19	.30
2	10.2	8.94	9.57	.32
3	9.70	8.28	8.99	.35
4	9.13	7.60	8.37	.38
5	8.54	6.89	7.72	.42
6	7.91	6.16	7.04	.43
7	7.25	5.40	6.33	.47
8	6.57	4.64	5.61	.48
9	5.85	3.91	4.88	.48
10	5.11	3.25	4.18	.47

Table 6.2

100 μm tantalum filter

$\rho R(mg/cm^2)$	$\sigma_1 \times 10^2$	$\sigma_2 \times 10^2$	$\tilde{\sigma}_{eff} \times 10^2$	$\pm \delta \tilde{\sigma}_{eff}$
1	2.09	3.70	2.90	.45
2	2.27	4.25	3.26	.50
3	2.47	4.61	3.54	.53
4	2.67	4.98	3.84	.58
5	2.89	5.37	4.13	.62
6	3.12	5.75	4.44	.65
7	3.36	6.13	4.75	.70
8	3.62	6.50	5.06	.72
9	3.89	6.82	5.36	.73

120 μm tantalum filter

1	5.51	7.53	6.52	.50
2	5.91	7.51	6.71	.40
3	6.26	7.42	6.84	.28
4	6.54	7.27	6.91	.18
5	6.73	7.07	6.90	.08
6	6.84	6.83	6.84	.05
7.	6.86	6.57	6.72	.07
8	6.79	6.28	6.54	.13
9	6.65	5.97	6.31	.17
10	6.44	5.64	6.04	.20

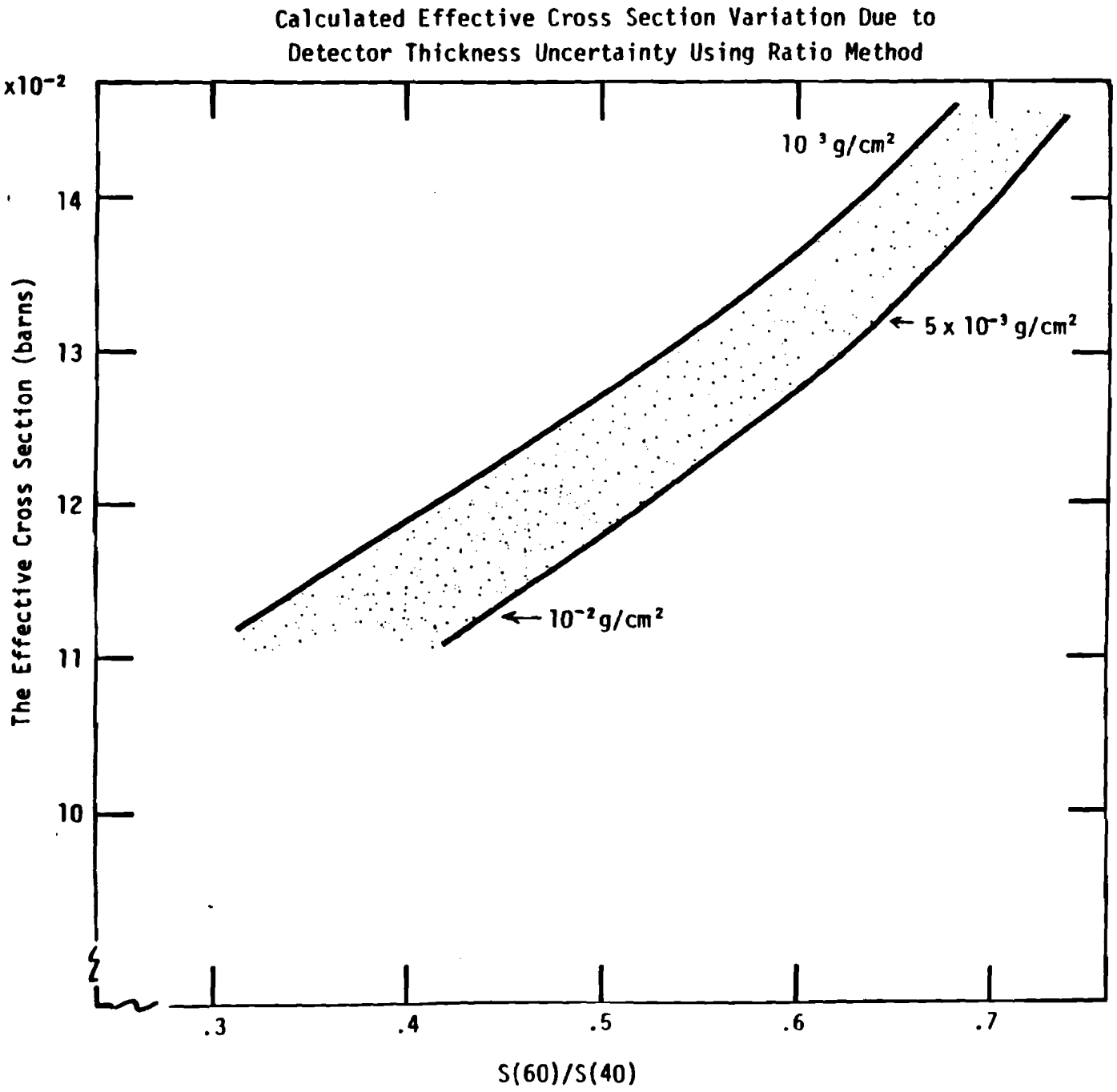
Calculated Effective Cross Section Variation Due to
Detector Thickness Uncertainty Using Ratio Method
x10⁻²
14
13
12
11
10
The Effective Cross Section (barns)
10⁻³ g/cm²
5 x 10⁻³ g/cm²
10⁻² g/cm²
.3
.4
.5
.6
.7
S(60)/S(40)

Figure 6.10

CALCULATE EFFECTIVE CROSS SECTION VARIATION DUE TO DETECTOR THICKNESS UNCERTAINTY USING RATIO METHOD

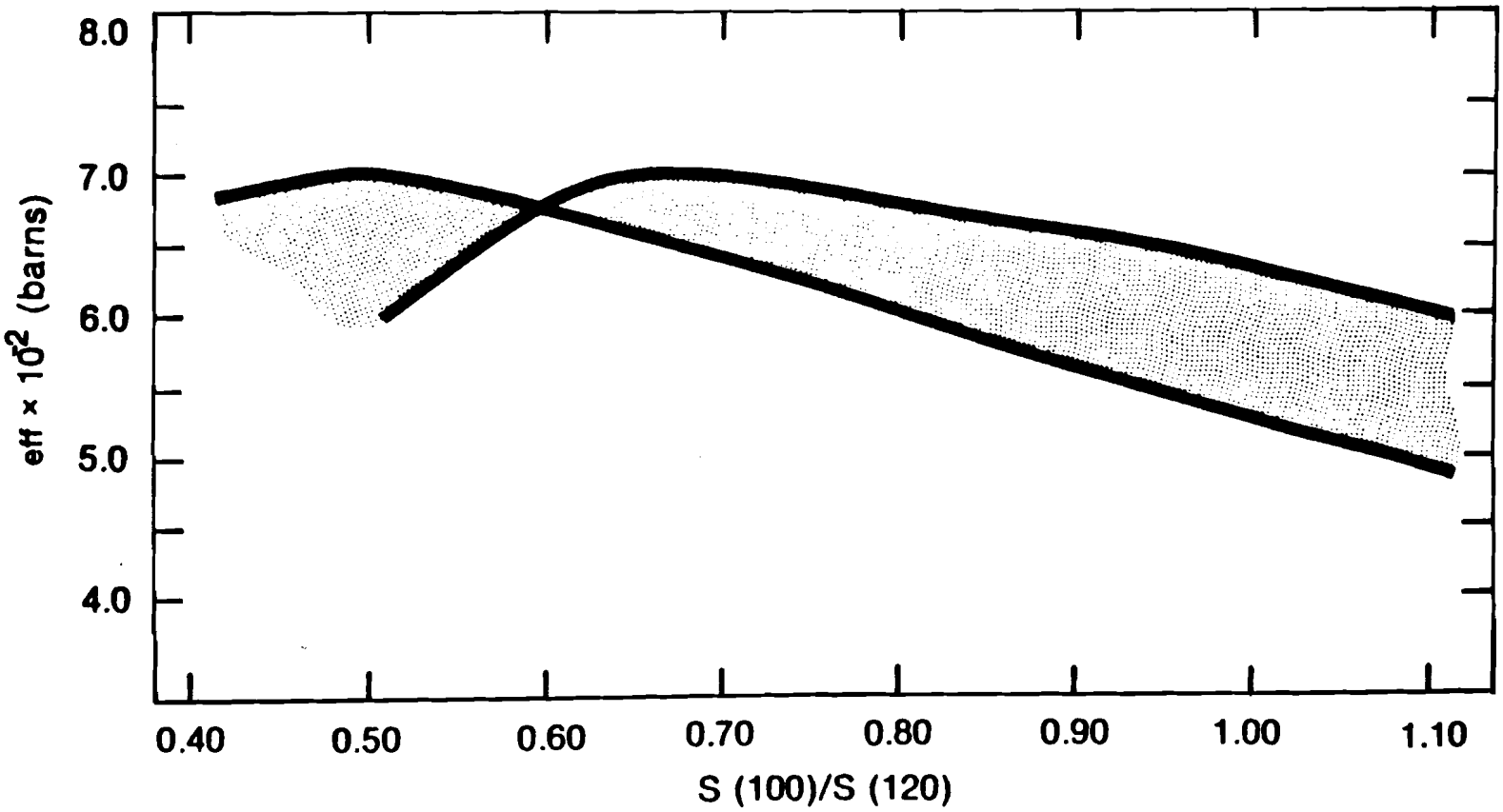

Figure 6.11

MODIFIED EFFECTIVE CROSS SECTION AS A FUNCTION OF DD-PROTON ENERGY LOSS — 40 μm TANTALUM FOIL SYSTEM

UR LLE

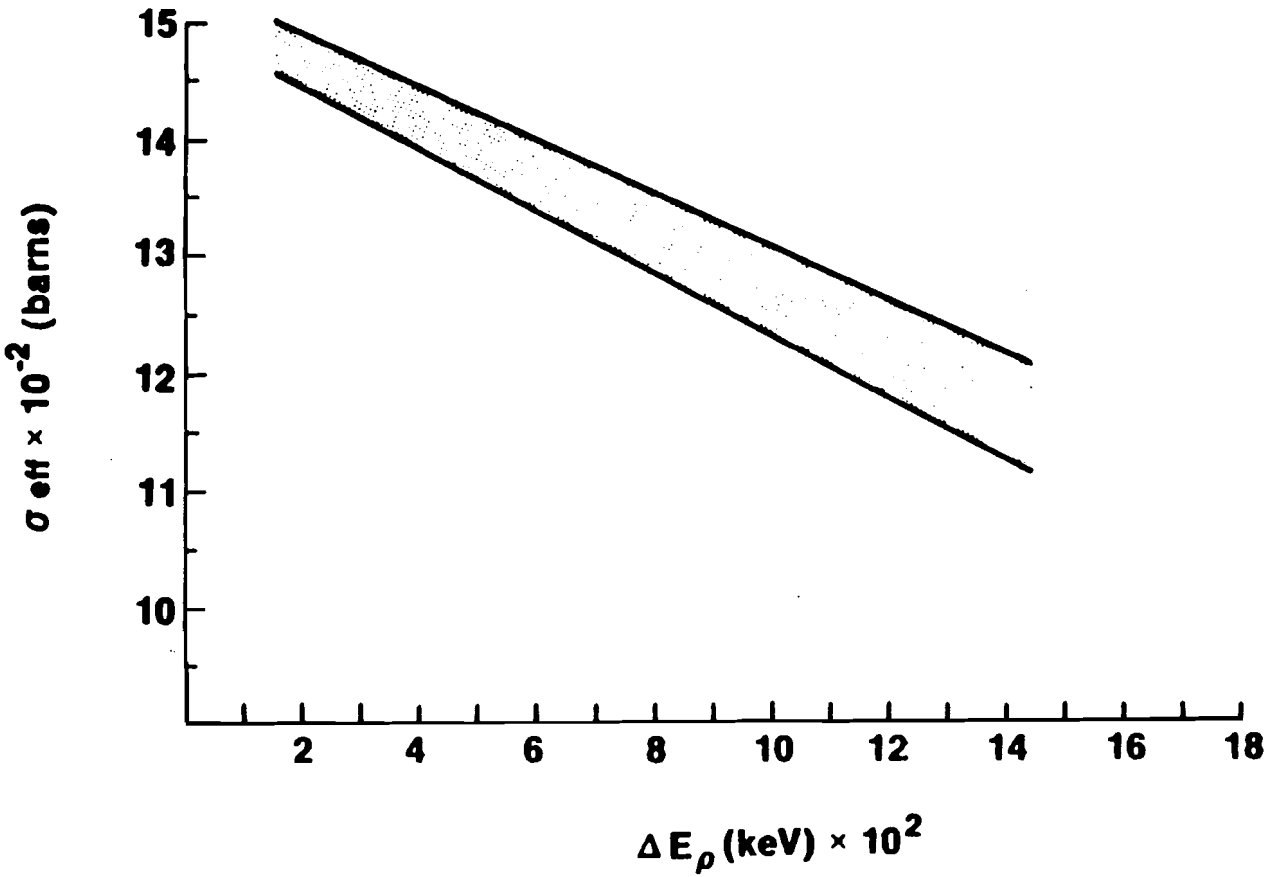

to be equal to 600 eV. If one folds in the spectrometer resolution of ± 200 KeV, it then results in a ± 6% uncertainty in $\tilde{\sigma}_{eff}$ for the 40 μm filter system. The uncertainty is somewhat worse for the 120 μm filter system being ± 10%.

Another type of thickness uncertainty that needs to be considered results from systematic error in the calibration of the micrometer. If the micrometer is off by an amount ε_δ than the thickness measurement will be in error as shown in Figure 6.13 below.

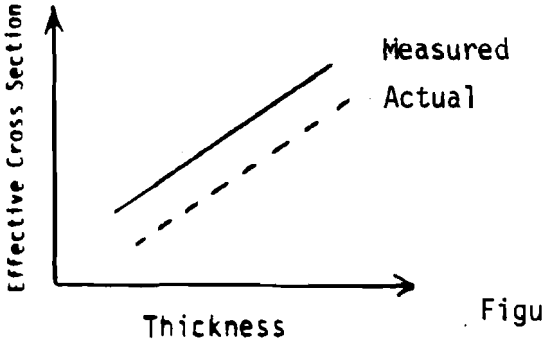

Figure 6.13

This analysis assumes that over the range of thickness variation, ε_δ is constant. As shown, the systematic error does not affect the measured thickness gradient and therefore $\delta\,\tilde{\sigma}_{eff}$ should be approximately the same as calculated earlier. However, the actual value of $\tilde{\sigma}_{eff}$ will be shifted. Excluding for now, the presence of ε_r, and looking only at the uncertainty associated with ε_δ one finds that even for measurement errors as large as 10 μm, uncertainty in $\tilde{\sigma}_{eff}$ is only ± 4%. This uncertainty can be significantly reduced by using a standard calibrated gauge.

In summary, it has been shown that detector thickness variations can be dealt with by defining an average effective cross section. The

uncertainty in this cross section (± 6%) is least when using the DD-proton energy loss method. However, the uncertainty is not much larger if applying the ratio method for the 40/60 (± 10%). Again, it should be stressed that these estimates are based on the worse case situation where thickness variations were taken to be 20 μm.

D. Extension of the Ratio Method to ρR Conditions in Excess of 10 mg/cm^2

The DD-proton energy loss method breaks down if the target ρR conditions exceed about 10 mg/cm^2. The only charged particle reaction products besides the knock-on particles to escape the target are DH_e^3- protons (14.7 MeV). Unfortunately, their velocities are about two times larger than the fastest deuteron. Therefore, correlation of energy loss of these protons with the effective cross section is poor.

It is therefore necessary to rely totally on the ratio method for target ρR greater than 10 mg/cm^2. Figure 6.14 shows the signal ratio correlated to the effective cross section for the 40 μm filter system. Also indicated on the figure is the approximate locations of the tamper ρR.

As seen, the ratio no longer gives a unique value for the effective cross section. Additional information supplied in the energy loss of the DHe^3- protons is necessary to establish the branch of this function. Beyond target ρR values of about 80 mg/cm^2, knock-on particles are slowed to the point where they no longer have sufficient energy to produce track coincidence.

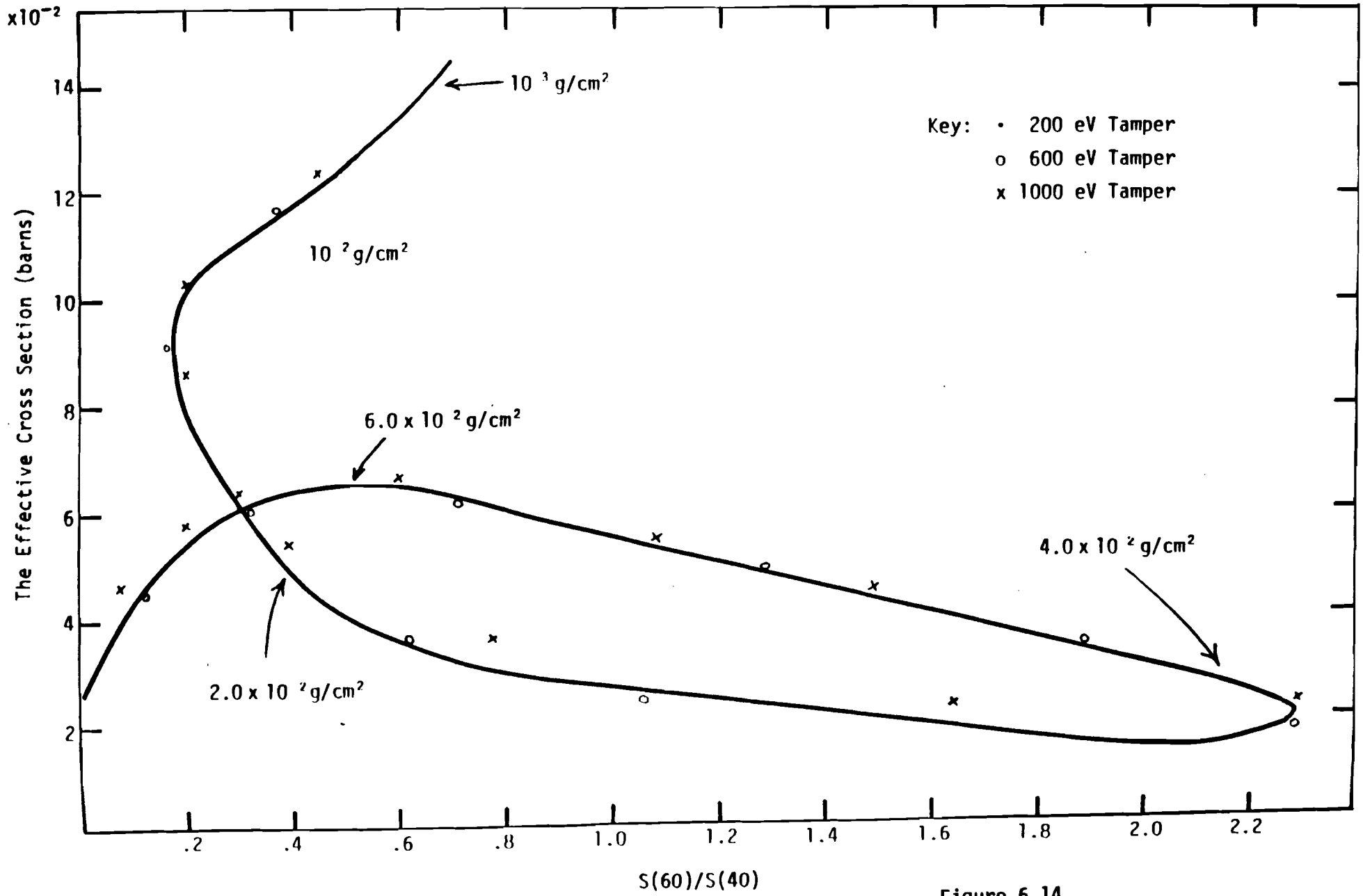
x10⁻²
14
12
10
8
6
4
2
The Effective Cross Section (barns)
10 ³ g/cm²
10 ² g/cm²
6.0 x 10 ² g/cm²
4.0 x 10 ² g/cm²
2.0 x 10 ² g/cm²
Key: • 200 eV Tamper
o 600 eV Tamper
x 1000 eV Tamper
.2
.4
.6
.8
1.0
1.2
1.4
1.6
1.8
2.0
2.2
S(60)/S(40)

Figure 6.14

Threshold conditions also change rapidly in this region. Figure 6.15 shows the minimum $\rho R \cdot Y_n$ product necessary to achieve 10 and 25% counting statistics on the 40 μm filtered detector. As seen, the present low ρR conditions have resulted in threshold conditions as much as nine times smaller than for future target conditions. Only future scaling experiments will establish whether adjustments in the collecting solid angle is necessary.

In conclusion, the knock-on diagnostic has been shown to accurately estimate fuel ρR conditions at the time of neutron production. Its success relies on its ability to discriminate against various backgrounds and its low threshold requirements. Future utilization of this diagnostic appears promising because the major anticipated problem of spectral distortion can be corrected for using either DD-proton energy loss correlation measurement or using multi-detector packages viewing different portions of the spectrum. Its implementation in future scaling experiments should prove a useful yardstick in determining one's proximity to thermonuclear breakeven.

ρRY THRESHOLD VALUES AS A FUNCTION OF TARGET ρR (Based on a Fraction Solid Angle of 0.01)

UR LLE

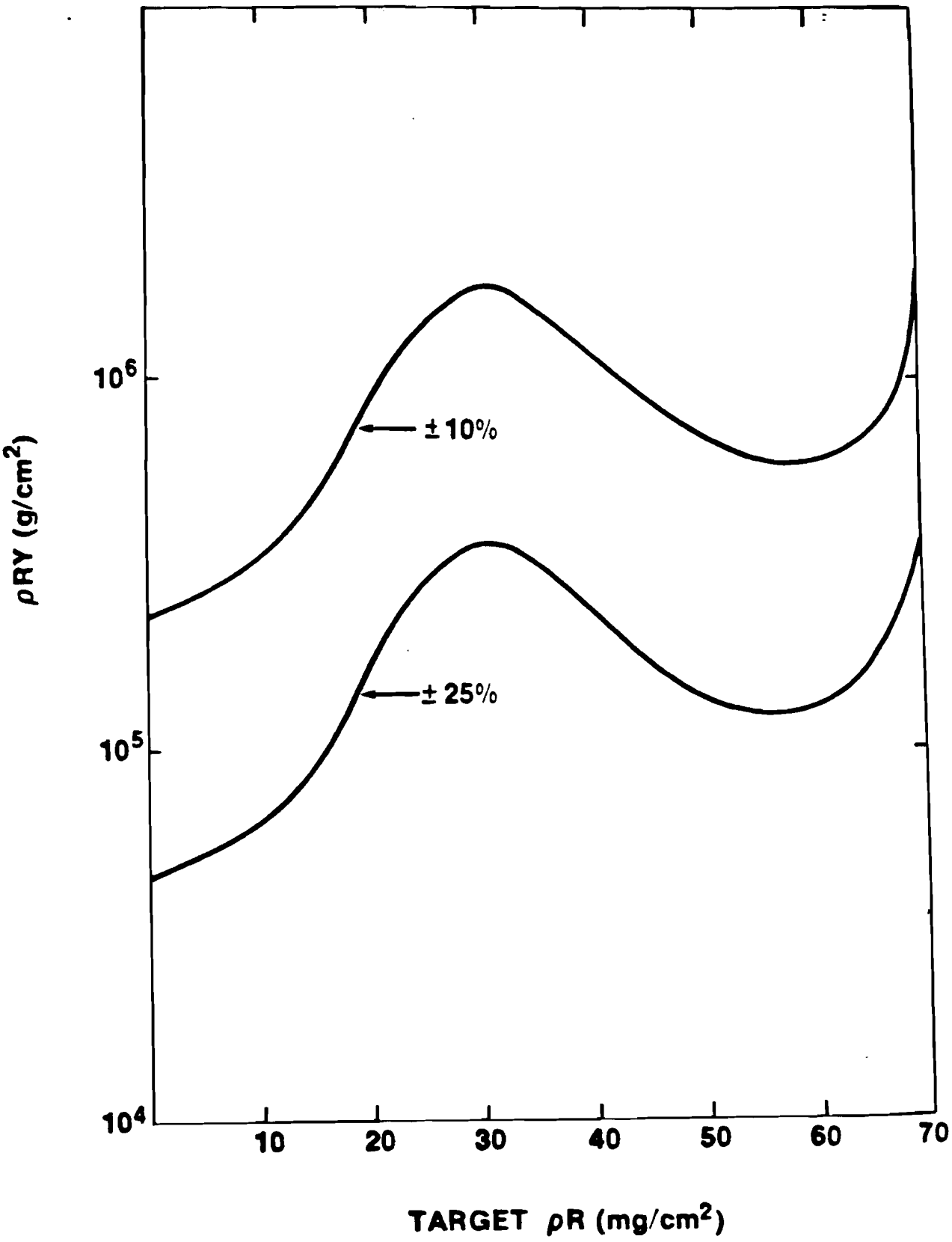

E1828

Figure 6.15

VII. THE APPROXIMATE LINE-OF-SIGHT FUEL ρR MEASUREMENT

A. Chapter Overview

Presented in this final chapter is a discussion of an important future application for the knock-on diagnostic. Since much interest in laser fusion is now directed towards understanding the degree of compression uniformity of the laser fusion target, the knock-on diagnostic can give valuable information of the approximate line-of-sight fuel ρR from predetermined direction.

This chapter will examine the relative contribution of knock-on particles from various locations of the fuel recorded by track detectors. The model presented will assume an isotropic neutron point source located at the center of the fuel. As will be discussed, the choice of the stopping foil thickness will determine the locations in the fuel where knock-on particles can scatter into the solid angle of the detector. The spatial contribution of these particles in the fuel will be shown to lie in the general line-of-sight direction.

Three stopping foil cases will be examined. The first case will show a 50 μm tantalum stopping foil approximately maximizes the total knock-on signal. This situation is identical with present experimental conditions. The second and third cases will measure the forward-scattered deuterons. Here it will be shown that line-of-sight ρR measurements are more nearly realized especially as one limits the count to the most energetic of knock-on deuterons.

B. Theory

Calculations presented in this chapter are based on the assumption that the neutron production is localized to a small central region of the fuel. This assumption is well-justified from both theoretical simulation studies as well as from x-ray pinhole camera measurements of the fuel temperature.

These calculations will be modeled by assuming an isotropic neutron point source. Also assumed is that the neutron mean-free path is much larger than the dimensions of the fuel so that multiple scattering can be neglected. Such an assumption is justified in present experiments where ρR conditions are much less than 1 g/cm^2.

Let the z axis represent the line-of-sight direction from the point source to the center of the detector as shown in Figure 1. The detector is circular in shape, as in the actual experiment, and its central axis is collinear with the z axis. Let θ be the polar angle with respect to the z axis as shown in the Figure 7.1.

Assuming a uniform fuel ρR, the azimuthal angle need not be explicitly carried through the calculations. For a given angle θ, the number of neutron dn, in a solid angle $d\Omega$ is propritonal to $2\pi \, \mathrm{Sin}\theta \, d\theta$. Defining $\hat{z}'$ as the initial direction the neutrons travel as indicated in Figure 7.1 the number of knock-on particles produced by these neutrons in $d\Omega$ is

$$\iint \sigma(\beta) \, \mathrm{Sin}\, \beta \, dn \, d\beta \, d\phi \qquad (7\text{-}1)$$

INTEGRATION GEOMETRY

UR
LLE

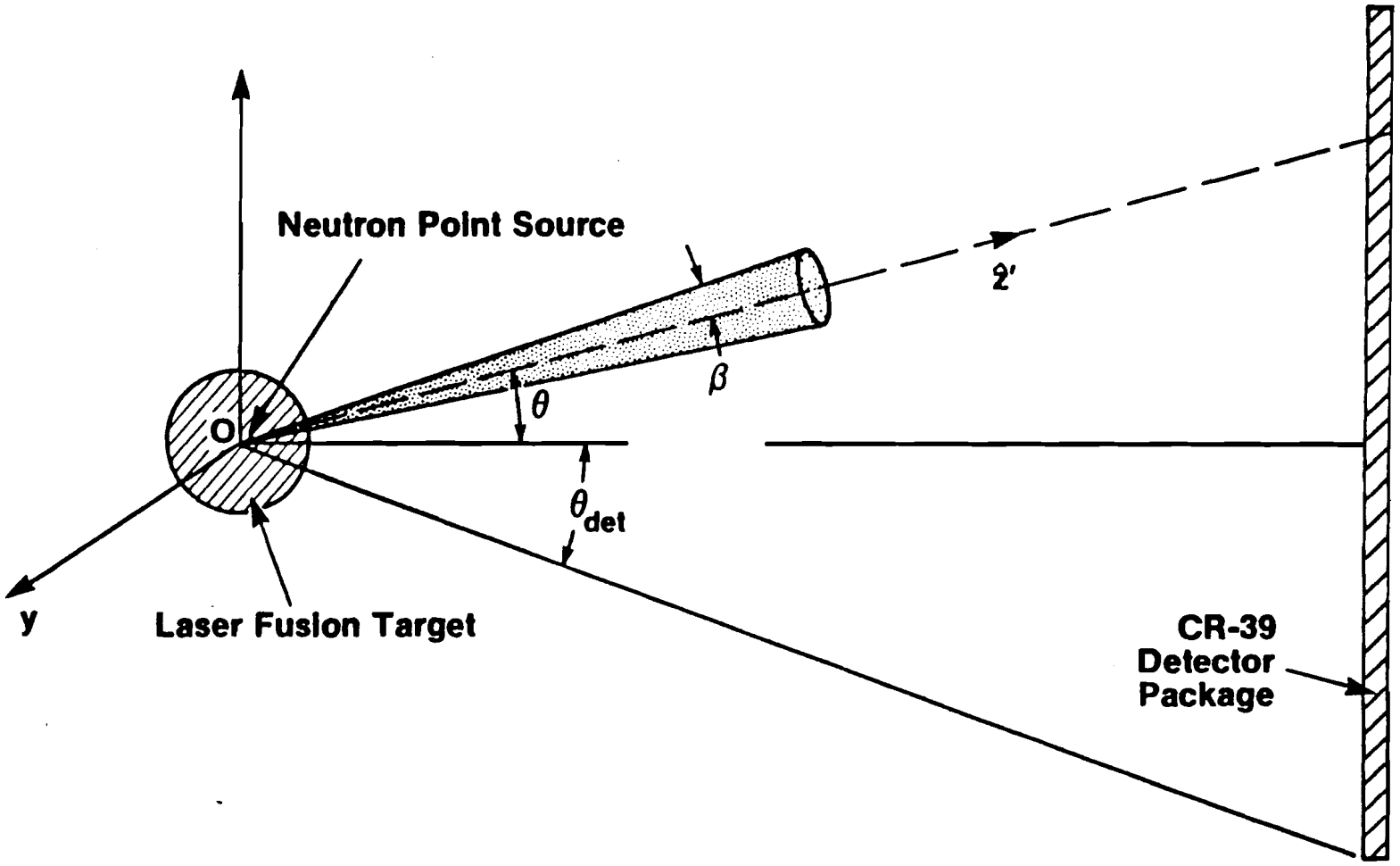

E1829

Figure 7.1

where β and ϕ are the scatter polar and azimuthal angles with respect to $\hat{z}'$ axis. The differential cross section $\sigma(\beta)$ is defined with respect to the $\hat{z}'$ axis. Therefore, the number of knock-on particles per unit angle $\frac{dN}{d\theta}$ scales as

$$\frac{dN}{d\theta} \sim \sum_{i=1}^{2} \iint_{\text{detector}} \sigma_i(\beta) \ \text{Sin}\theta \ \text{Sin}\beta \ d\beta \ d\phi \qquad (7\text{-}2)$$

where the sum is over the two types of knock-on species.

The energy differential cross section as previously shown in this dissertation can be related to the angular differential cross section by

$$\sigma(\beta) = \sigma(E) \left(\frac{dE}{d\beta}\right) \qquad (7\text{-}3)$$

The relationship between scattering angle β and energy in the laboratory frame is given by

$$E = E_n \frac{4 M_n M_i}{(M_n + M_i)^2} \text{Cos}^2\beta \qquad (7\text{-}4)$$

where E_n and M_n are the neutron energy and mass, and M_i is the knock-on particle mass. Therefore equation (3) scales as

$$\sigma(\beta) \sim \text{Cos}\beta \ \text{Sin}\beta \ \sigma(E) \qquad (7\text{-}5)$$

Substituting this expression into equation (2) yields

$$\frac{dN}{d\theta} \sim \sum_{i=1}^{2} \int_{0}^{\phi_{Max}^{(i)}} \int_{\beta_{Min}^{(i)}}^{\beta_{Max}^{(i)}} \sigma^{(i)}(E)\, \mathrm{Sin}\theta\, \mathrm{Cos}\beta\, \mathrm{Sin}^2\beta\, d\beta\, d\phi \qquad (7\text{-}6)$$

The limits of integrations are determined by the detector's angular dimensions subtended at the target and by both the stopping foil and detector thickness. In particular, the integration limit β_{Max} is set by the minimum energy knock-on particle which still has adequate energy to produce a spatial coincident track after exiting the stopping foil. The lower limit β_{Min} is set by the ability to discriminate the proton tracks from the knock-on coincident tracks. In other words, angles smaller than β_{Min} would produce knock-on tracks whose diameters are less than D* which are excluded in the actual measurement.

The ϕ integration limit ϕ_{Max} is dependent on θ, β, and the angle subtended by the track detector. Four cases determine the value of this parameter, as depicted in Figure 7.2.

C. Applications

Three cases will be examined: one which maximizes the total knock-on signal, and the other two which measure only the forward-scattered deuteron component. Table 7.1 lists all the relevant data for each case used in the evaluation of equation (6).

ϕ INTEGRATION CONDITIONS

UR LLE

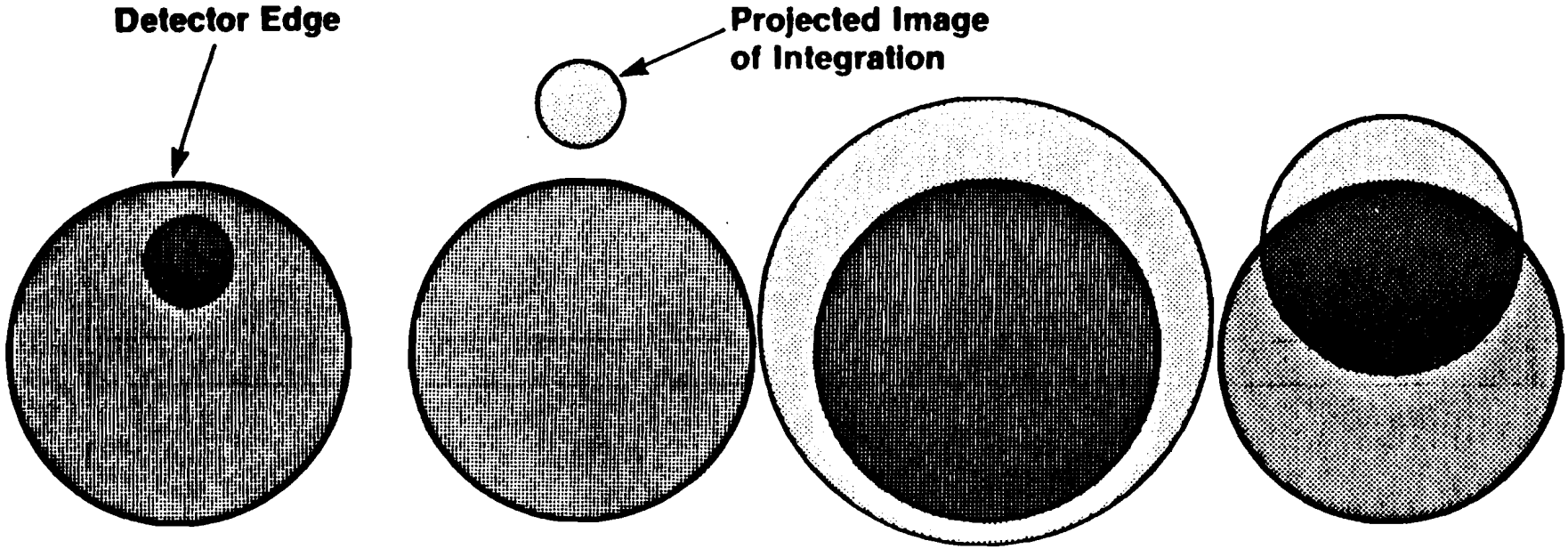

$\phi_{max} = \pi$

$\theta + \beta < \theta_{det}$

$\phi_{max} = 0$

$\theta_{det} + \beta < \theta$

$\phi_{max} = 0$

$\theta + \theta_{det} < \beta$

$$\phi_{max} = 2\cos^{-1}\sqrt{\frac{8\,(8 - \tan\theta_{det})}{\frac{\tan\beta}{\cos\theta}\,\tan\theta}}$$

where

$$q = \tfrac{1}{2}\left(\tan\theta + \frac{\tan\beta}{\cos\theta} + \tan\theta_{det}\right)$$

E1830

Figure 7.2

Table 1

Data Required for the Evaluation of Equation (6)

Stopping Foil Thickness (μm)	$\sigma^{(D)}(E)$	$\sigma^{(T)}(E)$	$\beta^{(D)}_{Min}$	$\beta^{(D)}_{Max}$	$\beta^{(T)}_{Min}$	$\beta^{(T)}_{Max}$
50	$.8911-\cos^2\beta$	$\cos^{\nu}\beta$	30.0^{o}	38.4^{o}	0.0^{o}	24.8^{o}
120	$\cos^{\nu}\beta$	0	0.0^{o}	22.1^{o}	N.A.	N.A.
140	$\cos^{\nu}\beta$	0	0.0^{o}	12.0^{o}	N.A.	N.A.

It should be noted from the table that:

1) All angles are converted into radians when performing the integration.
2) The CR-39 thickness after etching is taken to be 130 μm.
3) All tritons are stopped in the 120 μm tantalum foil.
4) $\sigma(E)$ is expressed in terms of β using equation (4). The accuracy of these empirical expressions are within ± 6%.
5) The proportionality constant has been dropped from the $\sigma(E)$ expression. Therefore, each component should be first normalized and then multiplied by its corresponding effective cross section.
6) For the 50 μm stopping foil case ν is equal to 15.26 while for the 120 and 140 μm cases ν is equal to 25.24.

The integration can be performed numerically. The first step is to decide for a given θ and β which of the four ϕ cases is appropriate. After evaluating ϕ the integrand is evaluated between β and $\beta + \Delta\beta$. Each β integration is added to the previous integrations until $\beta = \beta_{Max}$ is reached.

Figures 7.3 and 7.4 shows the dependence of $\frac{dN}{d\theta}$ as a function of θ for each of the two cases described above. Proper normalization in Figure 7.3 for each component is achieved by first normalizing each component separately and then multiplying each component spectrum by its effective cross section which for this case is .032 and .120 barns for the deuteron and triton components, respectively.

Notice that under present experimental conditions, a rather broad region of the target contributes to the knock-on signal. The reason for this is that the deuterons must be scattered by a large angle to have low enough energy to be separated from the proton background. By using a thicker foil as shown in Figure 7.1, the tritons are stopped in the tantalum foil and only deuterons reach the detector and produce spatial coincident tracks. In addition, since the energy lost by the deuterons is larger for the thicker stopping foil case, these particles need not be scattered as greatly to be separated from the proton background. This, in turn, minimizes the region over which the knock-on particles contributing to the measured signal can be produced in the fuel.

Two curves are shown in Figure 7.4. The 120 μm tantalum stopping foil accepts deuterons between about 11 and 12.5 MeV. By increasing

SPATIAL KNOCK-ON PRODUCTION DEPENDENCE IN FUEL

UR LLE

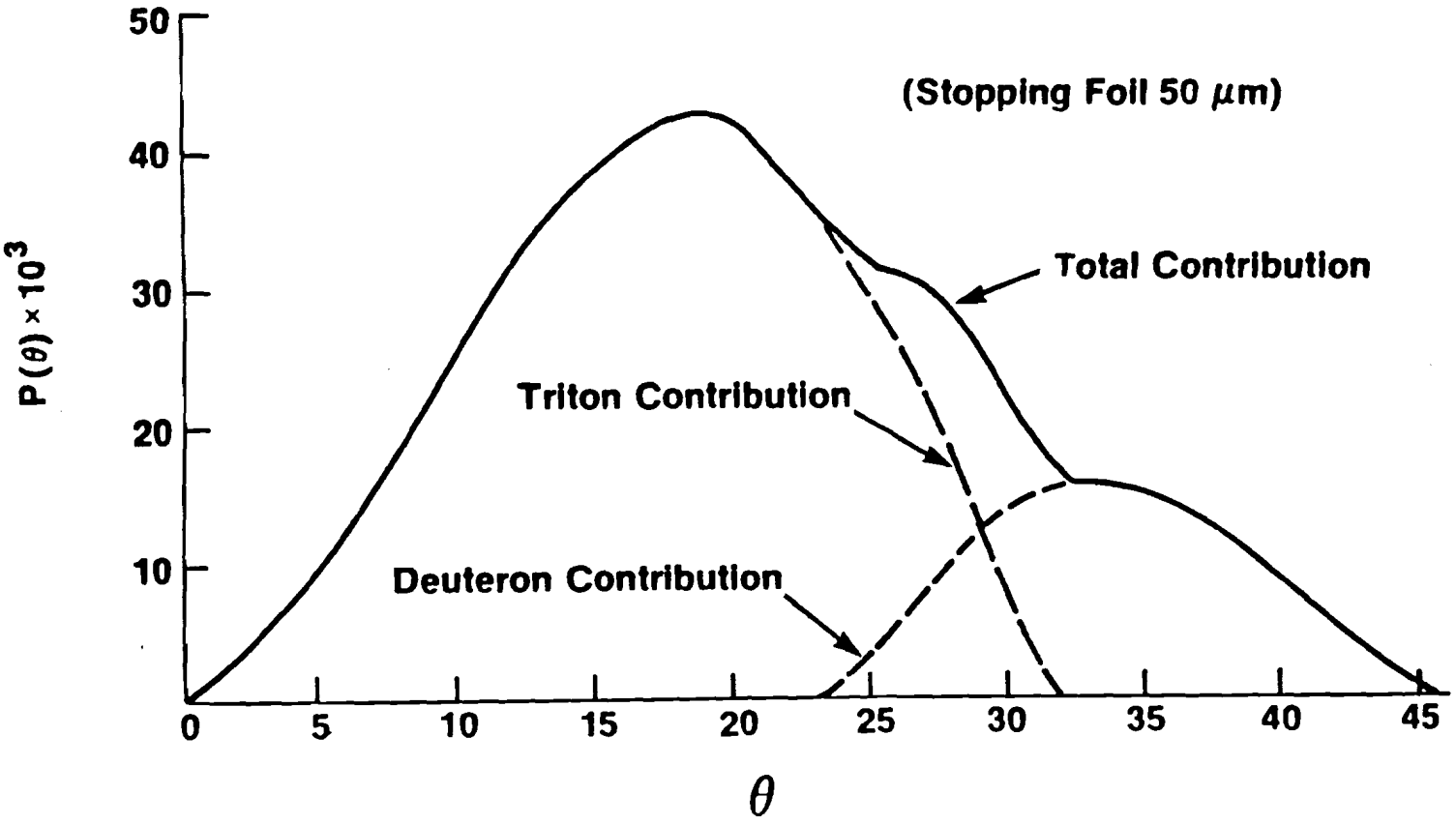

E1827

Figure 7.3

Knock-on Deuteron Production as a Function of Θ for Two Tantalum Stopping Foil Thicknesses

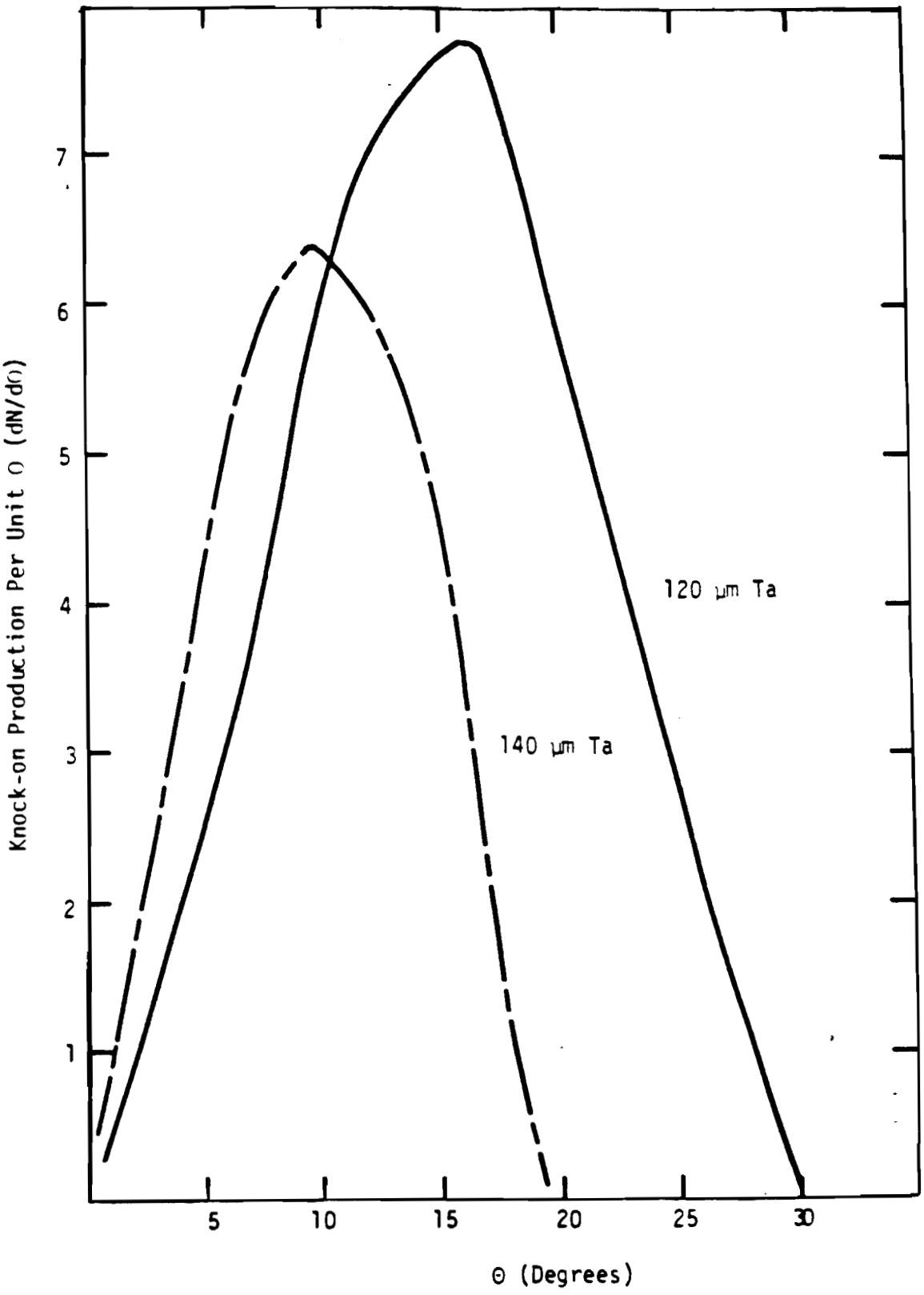

Figure 7.4

the thickness of the foil to 140 μm, the detector accepts knock-on deuterons between 12.0 and 12.5 MeV. This, in turn, reduces the maximum scattering angle from about 22^{o} to 12^{o}. The reduction in scattering angle is seen by the shift in the peak of $\frac{dN}{d\theta}$ to the left. Therefore, the line-of-sight measurement is improved by limiting the forward-scattered region recorded by the track detector. The trade-off in restricting the energy interval accepted by the detector to minimize contribution of off-axis knock-on deuterons is a reduction in the knock-on signal.

In summary, future measurements of fuel compression uniformity can be obtained with the use of the knock-on diagnostic. For best results, the stopping foil should stop all knock-on tritons and pass only the forward-scattered deuterons. Off-axis contributions of the signal can be minimized by raising the lower energy limit passed by increasing the foil thickness. This, however, leads to a reduction in the detectable deuteron signal.

VIII. SUMMARY AND CONCLUSIONS

In this concluding chapter, a summary of the important results discussed in the preceding chapters will be given. It will serve to piece together the many issues previously addressed. In doing so, it is hoped that the reader will finish this work with a more coherent understanding of the inter-connections of the various aspects discussed in this dissertation.

It has been shown that knock-on particles can be successfully used to measure the fuel ρR during the time of neutron production. From a simplistic perspective, this required the counting of knock-on particles produced during the thermonuclear burn as well as the measuring of the neutron yield. This number was shown to be proportional to the $\rho R \cdot Y_n$ product.

In reality, the measurement was complicated by the fact that solid state track detectors served as the only viable option available to record efficiently the knock-on particles. This can lead to a number of experimental difficulties.

Foremost, the major difficulty was discriminating proton tracks from knock-on tracks even though the signal-to-background calculations showed a 5:1 ratio. Skepticism among various colleagues motivated development of a technique capable of proton discrimination. This method discussed relied on measurement of both (1) the track diameter which gave velocity and charge information and

(2) the particle's minimum range through the indentification of spatial track coincidences which gave isotope mass information.

Another experimental difficulty was that the detectors had to be housed in an air environment so as to not be desensitized by extended periods in vacuum. A tantalum window allowed the knock-on particles to enter the chamber and strike the detector. Without such precautions, thin track detectors did not record hydrogen isotopes at all.

Complicating the experimental procedure, it was necessary to expose a small section of each detector to fission fragments generated from a Cf^{252} source. The fission fragment track diameter gave direct information of the etched depth and thus the effective detector thickness. This procedure was taken to alleviate any uncertainty arising from detector swelling after being etched for 16 hours at $70^{o}C$ in 6.25 N NaOH.

Knowledge of the effective thickness was required to calculate the acceptance window of the detector. This thickness placed restrictions on the minimum velocity required to produce spatial coincident tracks. Only knock-on particles having a finite range of velocities were able to produce spatial coincident tracks. Knock-on particles with velocities larger than the velocity required to produce proton-spatial-coincident could not be distinguished from proton tracks. This necessitated the introduction of the effective cross section. This cross section was the integrated differential cross section over the energy window where proton discrimination was possible.

Much of the theoretical uncertainty arose in calculating the value of the effective cross section. In present experiments the sources of this uncertainty resulted from measurement uncertainties in the stopping foil and detector thicknesses. However, the uncertainty in this cross section resulting from these measurement uncertainties was shown to be less than ± 5%.

As target ρR conditions increase above 4 mg/cm ^{2}, additional uncertainty in the cross section was examined. This was the result of spectral distortion due to charged particle energy loss as the knock-on particles traversed the target. As discussed, two methods can be implemented to correct for changes in the effective cross section.

One method relied not only on measuring the number of knock-on particles but also on measuring the energy shift of DD-protons. Here the acceptance window was centered across the triton forward-scattered peak. Since the protons had comparable velocities with that of the tritons, corrections due to the local differential cross section could be made. This method as shown broke down at about 10 mg/cm^2 where the DD-protons were stopped inside the target.

Above 10 mg/cm^2 a second method was developed to correct for spectral distortion. This involved counting knock-on particles from two adjacent energy intervals. The ratio of counts gave information of the local distortion. One important compromise in choosing the proper foil thickness combination was that if the two thicknesses were too close to one another, the count ratio did not deviate very much from 1. If the thicknesses were too different, the ratio did not correlate well with the effective cross section.

Two cases, namely the 40/60 and the 100/120 foil systems, were found to give adequate ratio variation and showed good correlation with the effective cross section.

In present experiments the major source of non-statistical uncertainty was shown to arise from estimates in the neutron yield (± 15%) and detector solid angle (± 10%). Other factors such as multiple scattering through the stopping foil, range straggling in the CR-39, and the various parameters characterizing the detector, did produce additional uncertainty in the cross section but were small compared with the uncertainties arising from Y_n and $\Omega/4\pi$.

The statistical uncertainty was influenced by (1) the collection solid angle, (2) the $\rho R \cdot Y_n$ product, and (3) the effective cross section. For an optimal stopping foil thickness of 40 μm (i.e., .0667 g/cm^2) and a 1% of 4π detection solid angle, the required $\rho R \cdot Y_n$ product to produce a ± 25% statistical uncertainty was shown to be equal to $\sim 6 \times 10^4$ g/cm^2.

Application of this methodology was used to measure the fuel ρR of DT-filled glass microballoons for high-intensity short-pulse and low-intensity long-pulse laser conditions. These measurements showed that under conditions of short pulse (~ 75 psec) and high intensity ($\sim 10^{16}$ w/cm^2), the fuel ρR was in the low 10^{-4} g/cm^2 regime. A 10-fold increase in the ρR was observed when laser conditions were changed to long-pulse (~ 1 nsec) low-intensity ($\sim 10^{14}$ W/cm^2) conditions. This general scaling was consistent with the interpretation that a smaller number of hot electrons preheated the fuel under low intensity conditions thereby enhancing the ultimate fuel compression.

Supportive data was also gathered demonstrating the ability of the methodology to experimentally separate proton tracks from knock-on tracks. As discussed, this involved the use of several different thicknesses of stopping foils to sample various portions of the knock-on particle spectrum. In addition, a stopping foil used to stop all knock-on particles was placed in front of one detector to demonstrate that no tracks recorded were confused as knock-on tracks.

In the last chapter it was discussed that the knock-on diagnostic had an important future application. By placing detectors around the target, non-uniformities in the compression during the time of neutron production could be measured. This was achieved by restriting the measurement to forward-scattered deuterons. Stopping foil thicknesses must be 120 μm thick or greater to approximate line-of-sight ρR measurement capability.

Future utilization of this diagnostic appears quite promising in light of other available options. To date, only radio chemistry has been shown to measure tamper ρR. Through computer modeling the fuel ρR can be inferred. Except for the knock-on approach, no method has measured the fuel ρR directly. In addition, unlike the other proposed schemes mentioned earlier, the knock-on method does not require specially prepared targets.

Therefore, the use of knock-on particles to directly measure fuel ρR is the best viable option in future laser fusion experiments. Its usefulness in studying non-uniformities of fuel compression is the next logical step in the utilization of the technology developed in this dissertation.

REFERENCES

1. S. Skupsky and S. Kacenjar, J. Appl. Phys. 52(4), 1981.
2. Total and differential cross sections for the interaction of 14 MeV neutrons were obtained from ENDF/D - IV library, National Neutron Cross Section Center, Brookhaven National Laboratory.
3. B. Cartwright, et. al., Nuclear Instruments and Methods 153, 1978.
4. R.L. Fleischer, et. al., "Nuclear Tracks in Solids," University of California Press, 1978.
5. Ibid.
6. Total and differential cross sections for the interaction of 14 MeV neutrons were obtained from ENDF/D - IV library, National Neutron Cross Section Center, Brookhaven National Laboratory.
7. E.M. Campbell, et. al., Appl. lett. 36(12), 1980.
8. H.R. Griem, "Spectral Line Broadening by Plasmas," Academic, New York, 1974.
9. T.E. Blue and D.B. Harris, FSL-14 (internal publication), Fusion Study Laboratory, University of Illinois.
10. V.L. Pan and J.T. Larsen, UCRL-79772, 1977.
11. S. Skupsky, "The Energy Loss of Ions Moving Through High-Density Matter," LLE 57, Internal Report, 1977.
12. S.T. Butler and M.J. Buckingham, Phys. Rev., Vol. 12 No. 1, 1962.

13. O.N. Kroklin and V.B. Rozanov, Soviet Journal of Quantum Electronics, Vol. 2, No. 4, 1973.

14. M. Goldberg, et. al., Neutron Cross Sections II C, BNL 325, 2nd Ed., Supl. No. 2, Brookhaven National Laboratory, 1966.

15. D.C. Santy and R.D. Werner, Nuclear Intrusments and Methods 188, 1981.

16. Total and differential cross sections for the interactions of 14-MeV neutrons were obtained from the ENDF/D-IV library, National Neutron Cross Section Center, Brookhaven National Laboratory.

17. C.F. Williamson, J.P. Boujot, J. picard, "Tables of Range and Stopping Power of Chemical Elements for Charged Particles of Energies 0.5 to 500 MeV," CEA-R 3042, 1966.

18. S. Kacenjar, L. Goldman, A. Entenberg, Rev. Sci. Instrum., 52(6), 1981.

19. D.C. Slater, KMSF-U-914, 1980 (unpublished).

20. C.L. Longmire, "Elementary Plasma Physics," Interscience, New York, 1963.

21. R. Fleischer, P. Price, R. Walker, "Nuclear Tracks in Solids," University of California Press, 1975.

22. H. A. Bethe, Ann. I. Physik 5, 325 (1930).

23. E.V. Benton and W.D. Nix, Nuclear Instruments and Methods, 67,1969.

24. L. Tommasino, Nuclear Instruments and Methods, 173, 1980.

25. P.C. Souers, R. T. Tsugawa, and R.R. Stone, LLL, UCRL-51609, 1974.

26. L.C. Northcliffe and R.F. Schilling, "Nuclear Data Tables," 1970.

27. W.H. Barkas and B.J. Berger, "Studies in Penetration of Charged Particles in Matter," NAS-NRC Publication 1133, Nuclear Science Series, Report No. 39, 1964.

28. J.F. Janni, Air Force Weapons Laboratory Technical Report No. AFWL-TR-65-150, 1966.

29. E. Segre, "Nuclei and Particles," W.A. Benjamin, Inc., 1965.

APPENDIX A

Solid State Track Detectors

A. Theory

Solid state track detectors (SSTD) are devices which record material damage information, in the form of latent tracks, produced when charged particles strike certain materials. These devices have high detection efficiencies and are relatively insensitive to x-rays. The SSTD's can be divided into two categories: the organic and the inorganic detectors. Of the two, only organic detectors have the required sensitivity to record hydrogen and helium isotopes. Five of the most sensitive organic track detectors are listed in table A.1 in order of most to least sensitive.[21]

Table A.1

Organic SSTD Composition and Energy Thresholds

Detector	Atomic Composition	Least Ionizing Ion Recorded
Allyl Diglycol Carbonate (CR-39)	$C_{12} H_{18} O_7$	$\sim$ 18 MeV ^1H
Cellulose Nitrate (CN)	$C_6 H_3 O_9 N_2$	$\sim$ .55 MeV ^1H
Cellulose Triacetate	$C_3 H_4 O_2$	$\sim$ 4.0 MeV ^4H
Polymethylmethacralate (Plexiglass)	$C_5 H_8 O_2$	$\sim$ 3.0 MeV ^4H
Lexan	$C_{16} H_{14} O_3$	$\sim$ 0.3 MeV ^4H_e

A fundamental property of all SSTD's is their ability to record charge particle passage through them in the form of tracks. Today there is general agreement that the cause of tracks is due to an energy transfer from the passing impinging charged particle to the surrounding bulk material.

In order for a theory to account for such formations, it must also explain two additional observed properties present in the track formation process. First, it must explain the fact that the smallest tracks observed are measured (without chemical etching) to be $\leq$ 50 Å in radius. Second, the theory must also account for threshold conditions needed in track registration.

The extremely small track diameters can be best explained from local energy deposition considerations.

Two mechanisms contribute to significant energy loss of the charged particle at high energies; namely (1) excitation and (2) ionization. In the case of polymers, process (1) can lead to bond breaking and thus radical formation when de-excited. Process (2) leads to the formation of delta rays which themselves, if energetic enough, can lead to secondary excitation and ionization. Figure 1 illustrates this process of bond breaking which is typical in polymers.

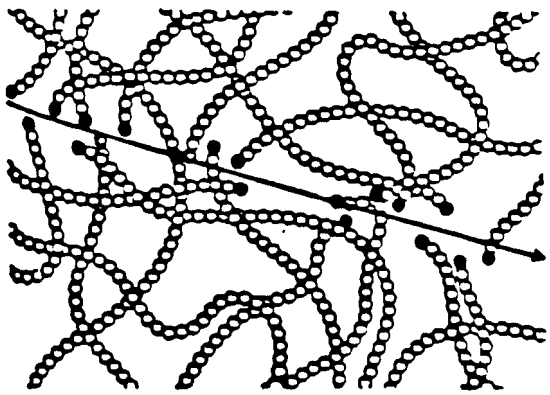

Figure A.1

It can be shown that, if one considers process (2) and calculates the net energy given to electrons in a shell centered around the particle trajectory, one finds that the number of high energy delta rays produced (small impact parameter) is greatly surpassed by the number of low energy delta rays (which have large impact parameters). Thus the majority of electrons move a short distance from the incident particle trajectory compared with high energy delta rays. Thus, heavy damage is expected to be locally confined to the immediate volume surrounding the particle trajectory.

After a sufficient distance within the detector, the charge particle slows down to where it can capture electrons and thus reduce its charge. This effective charge, based on experimental measurements by Heckman[21] takes the empirical form

$$Z^* = Z\,[1-\exp\,(-125\,\beta/Z^{2/3})] \qquad (1)$$

when $\beta \equiv v/c$ and works well in many solids although originally obtained from nuclear emulsion data.

In this domain of energies, the predominant mechanism for energy loss is through atomic collisions. This process also causes damage within the material; but in this case, it does not appear to be a predominant mechanism in the formation of tracks. The reason for this is that this mechanism does play a role in metals yet no tracks are observed.

Various models have been presented to explain the threshold conditions. Of these, three models are actively used at various laboratories throughout the world. These models are (1) Total Energy Loss, (2) Primary Energy Loss and. (3) Restricted Energy Loss.

The first model suggested by Fleicher[21] states that the track formation is governed by the total stopping power ($^{dE}/_{dx}$). Their early experiments tended to support the idea that a critical $^{dE}/_{dx}$ value existed, above which tracks would form. Typical data took the form as in Figure 2 below.

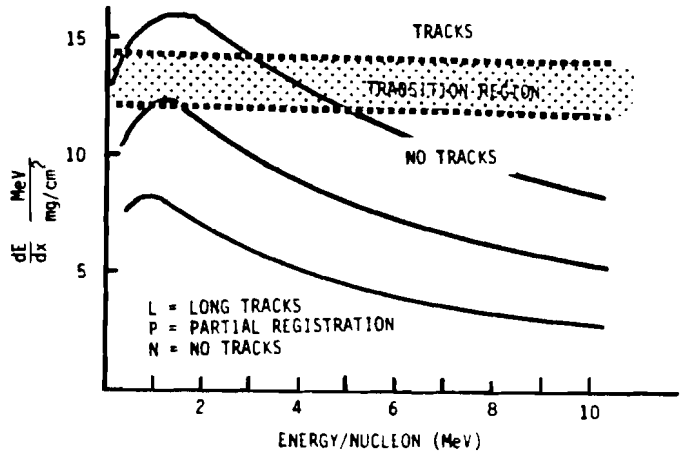

Figure A.2

The detector for this set of curves was muscovite mica. However, as more research was done, apparent violations to this simple model came to light. The theory, for example, had predicted tracks in CN for relativistic Fe nuclei. These tracks were never observed! The reason for this lack of registration is not difficult to understand. As the energy of the incident particle is increased, an increasing fraction of the energy goes into the formation of high energy delta rays which leave the immediate vicinity of the particle's path. This results in a lowering of damage density near the particle's path. This model was called the "Primary Ionization Model." It used the

fact that primary ionization and excitation occurs close to the ion's path, whereas secondary ionization and excitation are distributed over larger radial distances. It, therefore, assumes that track formation is a result of primary ionization of the bombarding particle. It states that tracks would result if the rate of primary ionization exceeds some critical value characteristic of the material. This model is based on Bethe's derivation[22] for stopping power. Two adjustable parameters are not predicted by the model; namely, the ionization potential of the outer shell electrons as well as the critical rate of primary ionization. Investigations indicate that the ionization potential parameter must be set equal to 2 eV to agree with experimental data. This is far below the value of ionization energy of the outer shell electrons in CN, as was pointed out by Benton[23]. It has been proposed that this value has resulted by a lower energy requirement in bond breaking since ionization in plastics is usually between 9 and 15 eV. The major criticism for this model is that it ignores energy loss by delta rays within the track region.

The difficulties of the last model led to the formation of yet another model. Benton[23], in his formulation of the model, has called it the "Restricted Energy Loss Model." A quantity called REL is defined in this model as the rate of energy loss of the impinging ion to distant electrons via coulombic interaction in the stopping medium. By "distant collision" is meant, those collisions which eject electrons of energy ω less than some adjustable parameter ω_o. The model postulates that track formation will commence only if the REL value is above some critical value characteristic of the stopping

material. This model makes no attempt to calculate either REL or ω_o. The major criticism of this model is that it assumes that damage is important at large distances from the particle's path, which is contrary to experimental findings. In fact, like the Total Energy Loss Model, it has predicted track registration for high energy particles which have not been observed experimentally. However, the Restrictive Energy Loss Model shows a smaller degree of error in prediction than does the Total Energy Loss Model.

It is therefore clear that experimental calibration must be carried out in order to obtain the response function for these detectors. Methods used to calibrate these detectors are discussed in Chapter 3.

Since the track diameters are extremely small and can only be observed under an electron microscope a chemical etch procedure is used to enlarge the tracks so that they can be easily seen under an optical microscope. This enlargement results from a differential etch rate between the bulk material and the area surrounding the track. In organic detectors, this difference in etch rates can be explained by the fact that as the charged particle propagates through the material, it ionizes and excites localized molecules which, in turn, break chemical bonds. The chain ends which result are more chemically reactive than the surrounding unbroken chains (See Figure 1 above) As a result, the track material etches at a velocity V_T while the remaining bulk etches at a rate V_g. As will be presently shown, optical tracks can only be formed if $V_T > V_g$. This is a necessary,

but not a sufficient, condition for optical track formation. Figure 3 below illustrates the etching process for normally incident charged particles. The optical track registration conditions

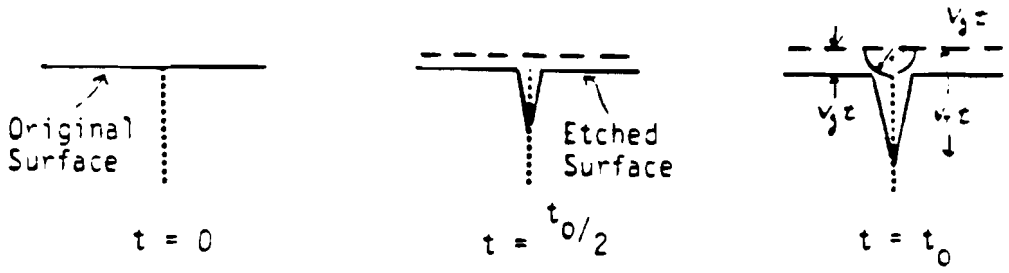

Figure A.3

can be readily derived from simple geometric considerations (See Figure 4).

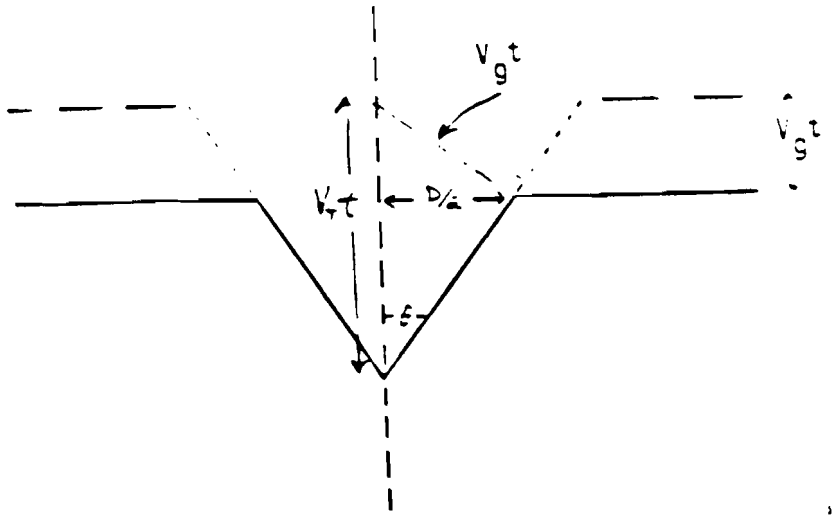

Figure A.4

$$\text{Noting that } V_T \, t \, \text{Sin}\, \theta = Vg \, t \tag{2}$$

$$\text{and } \ell \, \text{Sin}\, \theta = D/2 \tag{3}$$

$$\text{where } \ell \equiv D^2/4 + (V_T - V_g)^2 t^2 \tag{4}$$

then one can solve for the track diameter giving

$$D(t) = 2 V_g t \sqrt{\frac{V-1}{V+1}} \tag{5}$$

V is the track-to-bulk etch ratio (V_T/V_g). From equation (5) one observes that if V is large (as when for example the tracks are produced by fission fragments), the track diameter is a direct measure of the bulk etch rate. This fact is later used to estimate the amount of material etched away during the etching process.

It should also be noticed from this expression that if $V < 1$, D (t) is imaginary; no track diameter enlargement will occur. For the special case when $V = 1$, the etch rates are equal and no etch differential exist. This re-sults in a track diameter growth rate of zero and occurs because the track diameter growth due to the track etch rate is exactly compensated by the track diameter reduction rate due to the surrounding bulk surface being etched away. Therefore, optical track formation can only occur if the track etch rate is larger than the bulk etch rate.

The condition that track formation will result if $V = 1$ is only rigorously correct for normally incident charged particles. This is not a sufficient condition if the particle strikes the detector at an angle θ (See Figure 5 below).

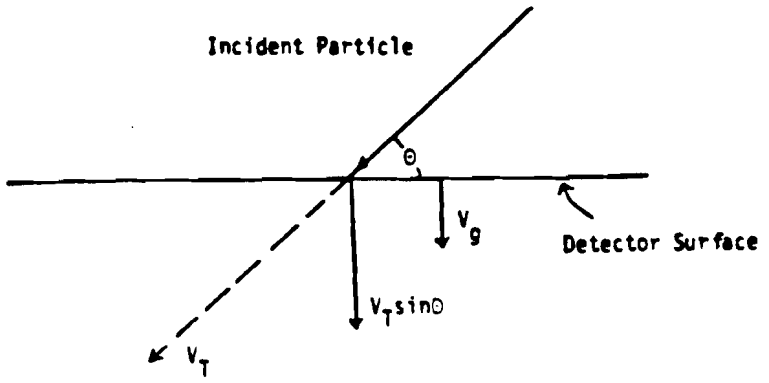

Figure A.5

For the case of inclined tracks, the necessary and sufficient condition for track registration is

$$V_T \text{ Sin } \theta > V_g \tag{6}$$

This results from the requirement that the vertical track etching velocity component be larger than the vertical bulk etching velocity.

Because of this situation, it is useful to distinguish between the etch and registration efficiency. Formally, the registration efficiency, η_R is defined as:

$$\eta_R \equiv \frac{\text{number of latent tracks intersecting surface}}{\text{number of incident particles}} \tag{7}$$

Upon etching however, not all latent tracks are revealed. The etch efficiency, η_E is defined as;

$$\eta_E \equiv \frac{\text{number of tracks revealed during etch}}{\text{number of latent tracks intersecting surface}} \tag{8}$$

For many types of track detectors the registration efficiency is close to 100%. However, these efficiencies are often not realized because of low etch efficiencies. The reduction in etch efficiency is attributed to the direction the particle enters the track detector. If the angle of incidence is less than a critical angle

(θcrit), track formation will not occur (at least for short etch durations). From equation (6) this angle is readily determinable, namely

$$\theta crit = Sin^{-1} \left({}^{V_g}/_{V_T} \right) \qquad (9)$$

The etch efficiency may change for prolong etchings. For example, energetic protons (on the order of an MeV or higher enter the track detector with an angle less than the critical angle. For short etching times the latent track would not produce visible tracks. However, as the protons begins to slow down inside the detector, the track-to-bulk etch ratio increases resulting in a decrease in the critical angle. At this point, the latent track may have an angle greater than the critical angle and therefore produces a visible track.

B. Experimental Considerations

To complement the above technical discussion of tract formation and registration criteria, a brief discussion should be given on the experimental aspects of chemical track etching. The process can range from a very crude to highly sophisticated approaches. In the crudest approach, one simply places a track detector into some appropriate etchant for a prescribed length of time. This approach lacks the required temperature control to insure reproducibility of results, especially if the parameter of interest is track diameter. Figure 6 below shows typical data of alpha track diameter as a function of temperature. It is clear that great care in temperature regulation is required to achieve reproducible results.

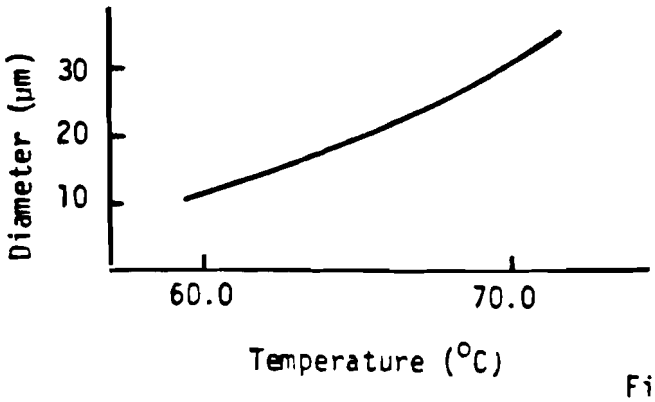

Figure A.6

The system used by this author employs a water bath with a thermo-probe to regulate the water temperature to within less than $\pm .1^{o}C$. During the etching process, a time history of temperature fluctuations was recorded by means of an auxiliary temperature monitoring system (747 Omega thermistor thermometer). A forced water circulation system in the bath insured that temperature gradients were less than $\pm 1^{o}C$ across the bath. To also insure that no temperature variations existed in the etchant, a magnetic stirred turbine device was used to stir the liquid. Figure 7 shows the experimental set up of the etching system.

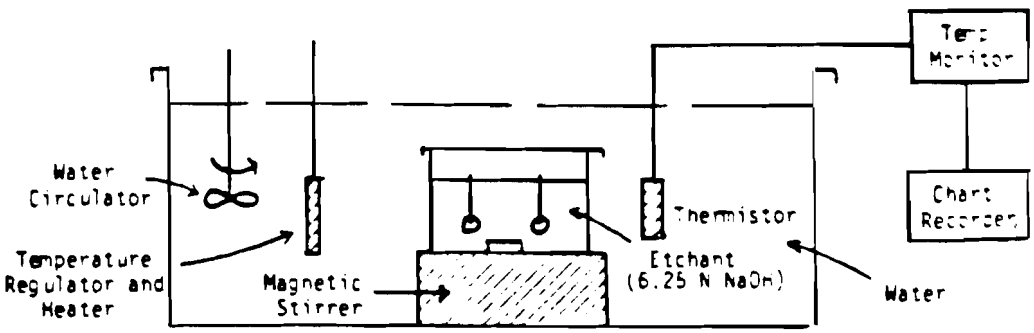

Figure A.7

Unlike the most sophisticated system, this did not employ thermal regulation of the etchant solution. Such systems have claimed temperature stabilities of ± .03°C.

Although chemical etching is by far the most used technique for track revelation, no discussion is complete without briefly mentioning electro-chemical etching. In its basic form a high ac voltage (several KV) is applied across a track detector during the chemical etch process. As demonstrated first by Tommasino,[24] track enhancement can be achieved to the point where individual tracks can be seen even without the use of an optical microscope.
The basic layout of the electrochemical cell is shown in Figure 8.

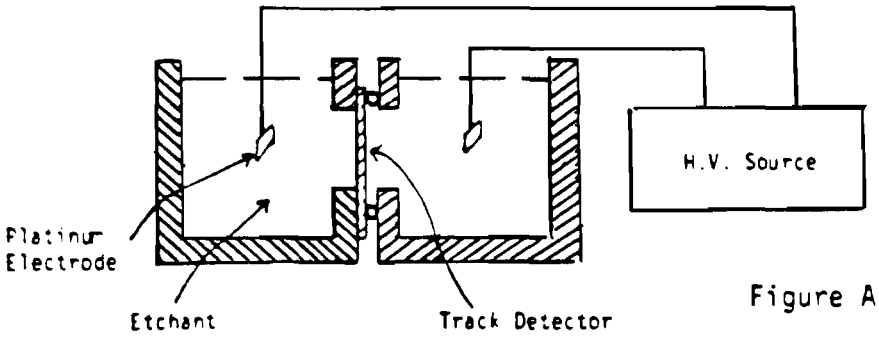

Figure A.8

This etching process can be divided into two steps. Initially, the etchant produces small pits in the detector with characteristic sharp points at the base of each track. Since the tracks are characterized by a relatively high electrical conductivity compared with the detector bulk material, at the points of these tracks the local electric field is much larger than the applied field and results in localized electrical breakdown. The result is the "tree discharge phenomenon" as depicted in Figure 9. In general, as

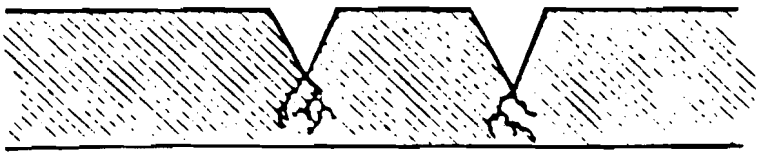

Figure A.9

the applied field and frequency is increased the track diameter also increase.

At present this technique has been employed in personnel neutron dosimetry. The applicability of this techniques in determining particle energies is still however, in its infancy.

Regardless of which etch technique is used, certain considerations should be given as to the handling of these detectors before and after the etch. Prior to etching, one should be extremely careful not to touch the detector with bare hands for it leaves permanent marks (contaminants) on the detector. In addition, the oils left on the track detector may alter the local etching characteristics of the detector. This, in turn, results in an alteration in the local track characteristics such as diameter and depth.

It is not advisable to try and clean plastic detectors with water for there is experimental evidence which indicates that these detectors absorb water. This water takes a considerable length of time before it evaporates out of the detector. The presence of water tends to change the track etching characteristics.

Also, it is not good practice to try and rub track detectors clean for this process generates fine scratches on the surface of the detector. These scratches after etching look like massive valleys when viewed under a microscope and partially obscure the field of view of tracks.

After etching the detectors should be rinsed thoroughly with distilled water making sure no etchant remains on the track detector surface. In addition, the detectors should not again be handled so as not to place finger prints on the detectors' surface. For thin detectors it is advisable to mount them on a smooth surface (such as a microscope slide) for easy handling and for reducing the risk of breakage.

APPENDIX B

The following is a derivation of the burn-up equation. The fractional burn up, defined as

$$f_r \equiv \frac{n_a + n_n}{n_a + n_n + n_d + n_T}$$

$$\equiv \frac{n_p}{n}$$

can be expressed in terms of the fuel ion density (i.e., $n_i = n_d + n_T$) as

$$f_r = \frac{n_p}{n} = \frac{n - n_i}{n} = \frac{n_i}{n} \qquad (A)$$

Noting that n is a constant (i.e., $n = n_i + n_p$), then

$$\dot{n}_i = -\dot{n}_p = -n\dot{f}_r \qquad (B)$$

For the case where $n_{D_o} = n_{T_o}$ the reaction rate per unit volume is given by

$$R_i = n_D n_T \langle\sigma v\rangle = \frac{1}{4} n_i^2 \langle\sigma v\rangle$$

$$R_i = -\dot{n}_D = -\dot{n}_T = -\frac{1}{2} n_i$$

$$\dot{n}_i = -\frac{1}{2} n_i^2 \langle\sigma v\rangle$$

Substituting this equation into equation B one obtains

$$\dot{nf}_r = \frac{n^2}{2} (1-f)^2 \langle\sigma v\rangle \qquad (C)$$

From equation A, n_i can be expressed in terms of f; therefore equation C becomes

$$\dot{f}_r = \frac{n}{2} (1-f)^2 \langle\sigma v\rangle \qquad (D)$$

defining the reaction time as

$$\tau_r \equiv \frac{1}{n \langle\sigma v\rangle}$$

then expression D takes the final form, as given in the text,

$$\dot{f}_r = \left(\frac{1}{2\tau_r}\right) (1 - f_r)^2$$

APPENDIX C - S/N ESTIMATE CALCULATIONS

The following analysis calculates the number of (n,p) reactions arising from both the fuel and tamper. A signal-to-background ratio is estimated.

Two reactions contribute to the signal.

1. $n(d,n')\ D'$ $\quad\quad \sigma = 620$ mb
2. $n(t,n')\ T'$ $\quad\quad \sigma = 920$ mb

In addition, four background reactions arise from the fuel.

1. $D(d,p)\ T$ $\quad\quad$ Proton energy $\simeq 3$ MeV
2. $D(n,2n)\ H$ $\quad\quad \sigma = 280$ mb
3. $He^3(d,p)\ He^4$ $\quad\quad$ *$R_1 \simeq 5\times10^{-3}$ for $\rho R_\delta = 10^{-2}$ g/cm^2
4. $He^3(t,d)\ He^4$ $\quad\quad$ **$R_2 \simeq 8\times10^{-4}$ for $\rho R_\delta = 10^{-2}$ g/cm^2

* $$R_1 \equiv \frac{\text{Number } He^3\ (d,p)\ He^4}{\text{Number } D\ (d,n)\ He^3} \qquad T_\delta \gtrsim 1 \text{ KeV}$$

** $$R_2 \equiv \frac{\text{Number } T\ (He^3,d)\ He^4}{\text{Number } D\ (d,n)\ He^3} \qquad T_\delta \gtrsim 1 \text{ KeV}$$

Additional (n,p) reactions arising from neutron activation of the tamper (glass) must be considered. A detailed breakdown of the chemical composition of the glass is given below in table C.1.

Table C.1. Molar Chemical Composition of the Glass Tamper

Chemical Component	M.W.	Molar Concentration (F)
SiO_2	60.08	79.3
CaO	56.08	10.7
Na_2O	61.98	4.4
B_2O_3	69.62	3.6
*Other	———	2.0

* A number of other trace oxide components.

Below is a table of all possible (n,p), (n,t) and (n,np) reactions which can occur in the tamper

Table C.2. Tamper Neutron Induced Reactions and Corresponding Cross Sections

Reaction	Cross Section in mb (for 14 MeV Neutrons)
Si^{28} (n,p) $A\ell^{28}$	160 ± 16 mb Ep>2.9 MeV
Si^{28} (n,np) $A\ell^{27}$	26 ± 22 mb
O^{16} (n,p) N^{16}	45 ± (10) mb
Ca^{40} (n,p) K^{40}	298 ± 38 mb
Ca^{40} (n,t) K^{38}	< .02 mb
Na^{23} (n,p) Ne^{23}	35 ± (15) mb
B^{11} (n,p) Be^{11}	3.3 ± .6 mb
B^{11} (n,t) Be^{9}	15 ± 5 mb

The effective number density for each of the chemical components is given by

$$n_{eff} = N_A \frac{F}{100} \frac{\rho^o}{M.W.}$$

where ρ^o is the natural density of a particular chemical component. Table C.3 below gives n^{eff} for the various components.

Table C.3 Relevant Information for the Calculation of n^{eff}

Chemical Component	Natural Density Lg/cm^3)	M.W.	n_{eff} (cm^{-3})
SiO_2	2.19	60.08	1.74×10^{22}
CaO	3.31	56.08	3.80×10^{21}
Na_2O	2.27	61.98	9.52×10^{20}
B_2O_3	1.81	69.62	5.64×10^{20}

The relevant information, however, is the atomic number density and are listed below along with its fractional number density, $\hat{n}$.

Table C.4. The Atomic Number Densities Found in a Typical Glass Tamper

Element	Atomic Number Density (n)	A
O	4.12×10^{22}	.63
Si	1.74×10^{22}	.27
Ca	3.80×10^{21}	.06
Na	1.90×10^{21}	.03
B	1.13×10^{21}	.02

The goal is to express the background in terms of tamper ρR. To do this, one must calculate the average atomic mass. Then one can relate the total atomic number density to the tamper density. Table C.5 below gives the relevant data used to calculate the average atomic mass <M>.

Table C.5. The Calculation of <M>

Element	M (AMu)	Mn
O	15.994	6.59×10^{23}
Si	28.086	4.89×10^{23}
Ca	40.08	1.52×10^{23}
Na	22.999	4.37×10^{22}
B	10.811	1.22×10^{22}

$$\Sigma\ n = 6.54 \times 10^{22}$$

$$\Sigma\ Mn = 1.36 \times 10^{24}$$

thus, $$\langle M \rangle = \frac{\Sigma Mn}{\Sigma n}$$

$$= 20.73 \text{ Amu}$$

$$= 3.46 \times 10^{-23} g$$

It is now possible to estimate the tamper background Q_b, in terms of the tamper, $\rho\Delta R$, and the thermonuclear yield, v by:

$$Q_b = (n_o\sigma_o + n_{Si}\sigma_{Si} + n_{Ca}\sigma_{Ca} + n_{Na}\sigma_{Na} + n_B\sigma_B)\ \Delta R\ Y_n$$

$$= n_{total}\ (\hat{n}_o\sigma_o + \hat{n}_{Si}\sigma_{Si} + \hat{n}_{Ca}\sigma_{Ca} + \hat{n}_{Na}\sigma_{Na} + \hat{n}_B\sigma_B)\ \Delta R\ Y_n$$

$$= \frac{\rho\Delta R}{\langle M \rangle}\ (\hat{n}_o\sigma_o + \hat{n}_{Si}\sigma_{Si} + \hat{n}_{Ca}\sigma_{Ca} + \hat{n}_{Na}\sigma_{Na} + \hat{n}_B\sigma_B)\ Y_n$$

Substituting in the numbers give:

$$Q_b = \frac{(\rho\Delta R)\ Y_n}{34.6\times10^{-24}}\ (.63)(.045\times10^{-24}) + (.27)(.272\times10^{-24}) +$$

$$(.06)(.298\times10^{-24}) + (.02)(.035\times10^{-24}) + (.02)(.018\times10^{-24})$$

$$= 3.41 \times 10^{-3}\ (\rho\Delta R)\ Y_n \qquad (1A)$$

The signal Q_{sig} can also be estimated from the fuel. Since we are comparing total elastic cross sections, we set $\Gamma_D = \Gamma_T = 1$ in eq. (1.3) of the main text.

$$Q_{Sig} = (\rho R)_f \frac{1}{5M_p} (\sigma_p + \sigma_n) Y_n$$

$$= \frac{1}{5x1.67} (.62 + .92) (\rho R)_f Y_n$$

$$= 1.84x10^{-1} (\rho R)_f Y_n \qquad (2A)$$

There is also a background component Q_b^f originating from the fuel which can be also expressed in terms of $(\rho R)_f$ and Y_n. This reaction is the n(d,2n)p which has a cross section of 18 mb.

$$\text{thus, } Q_b^f = \rho R_f \frac{1}{5M_p} \sigma (n,2n) Y_n$$

$$= \frac{1}{5x1.67} (.18) (\rho R)_f Y_n$$

$$= 2.16 \times 10^{-2} (\rho R)_f Y_n$$

Since the DD reaction is down by a factor of $\sim$ 100, then the He^3 (d,p) He^4 and He^3 (t,d)He^4 are down by orders of 10^{-5} for $(\rho R)_f$ conditions as high as $10^{-2} g/cm^2$. This is a negligible background that will not contribute significantly to the total background.

Therefore the signal-to-noise ratio is estimated to be

$$S/N = \frac{1.84 \times 10^{-1} (\rho R)_d}{3.41 \times 10^{-3} (\rho \Delta R) + 2.16 \times 10^{-2} (\rho R)_d} \qquad (3A)$$

For a specific example consider the following fuel and tamper ρR conditions at the time of peak burn:

$$\rho R_d \sim 5 \times 10^{-3} \text{ g/cm}^2$$

$$\rho R_t \sim 1.5 \times 10^{-2} \text{ g/cm}^2$$

thus,

$$S/N \simeq 5.8$$

This background can be greatly improved after additional track criteria are used to separate the proton tracks from the deuteron and triton tracks. These criteria are discussed in detail in Chapter III of the text.

APPENDIX D

Hydrogen Isotope Range and D* Calculations In CR-39

To adequately determine the effective cross section, knowledge of the knock-on ranges in CR-39 must be known. Since only emperical data exist on the energy-range dependence in element, the estimate used in this dissertation have been obtained by using the Bragg additivity rule. Its applicability does not strictly hold for the stopping of protons in hydrocarbons yet for lack of any better model, it is used in the below calculation. These deviations have however, little effect on the range calculation for energetic protons.
energetic protons.

The energy loss consist of two components: (1) the electronic energy loss (i.e., where the energy loss is due to excitation and ionization of the bulk material) and (2) nuclear stopping losses (i.e., where the energy loss is due to elastic scattering off screened target nuclei). For protons, the latter is of minor importance for energies above 10 KeV amount to only $\sim$ 2% of the total energy loss. Its significance decreases with increasing energy. Therefore, calculations assume that the electronic energy loss totally determines the particle range.

Data used in the following calculations were taken from Nuclear Data Tables of Northcliffe and Schilling.[26] No estimations are given